Design and Analysis of Fiber Bragg Grating for Quasi-Distributed Sensing Applications

A Thesis Submitted in Partial Fulfillment of the Requirements for the

Award of the Degree

of

DOCTOR OF PHILOSOPHY

By

KRISHNA MOHAN DWIVEDI

DEPARTMENT OF EEE

INDIAN INSTITUTE OF TECHNOLOGY GUWAHATI

GUWAHATI-781039, INDIA

August 2021

Declaration

I hereby declare that the thesis entitled "**Design and Analysis of Fiber Bragg Grating for Quasi-Distributed Sensing Applications**", submitted in the department of Electronics and Electrical Engineering, Indian Institute of Technology Guwahati, Assam, India, for the award of the degree of **Doctor of Philosophy**, has been carried out by me under the supervision and guidance of **Prof. Sunil K Khijwania and Dr. Gaurav Trivedi**. The results embodied in this thesis are original and have not been submitted to any other University or Institute for the award of any degree or diploma.

Dated: 28/08/2021

Place: Varanasi

Krishna Mohan Dwivedi (126102017)
Research Scholar, EEE
Indian Institute of Technology, Guwahati
Guwahati – 781 039, Assam, India

Certificate

This is to certify that the thesis entitled "**Design and Analysis of Fiber Bragg Grating for Quasi-Distributed Sensing Applications**", submitted by **Krishna Mohan Dwivedi (126102017),** a research scholar in the department of Electronics and Electrical Engineering, Indian Institute of Technology Guwahati, for the award of the degree of **Doctor of Philosophy**, is a record of an original research work carried out by him under my supervision and guidance. The thesis has fulfilled all requirements as per the regulations of the institute and in my opinion has reached the standard needed for submission. The results embodied in this thesis have not been submitted to any other University or Institute for the award of any degree or diploma.

Dated:

Place: Guwahati

Prof. Sunil K Khijwanai
Department of Physics, IIT Guwahati
Guwahati-781039, Assam, India

Dr. Gaurav Trivedi
Department of Electronics & Electrical Engineering, IIT Guwahati
Guwahati-781039, Assam, India

Dedicated

To

My parent and family specially my daughters Kavya Dwivedi and Ansh Dwivedi

&

To

Those who help me in my hard time

&

To

Almighty God

Abstract

The present thesis work is focused on the design and analysis of novel fiber Bragg grating (FBG) structures for its efficient application in quasi-distributed sensing network (QDSN). Novel grating structures are designed to achieve widest possible dynamic range and to enhance the sensing capabilities manifold. A comprehensive theoretical study is carried out to achieve the objective of the research work. In order to devise an efficient WDM/QDSN for the given source-bandwidth, critically important characteristics, e.g., reflectivity/transmissivity, FWHM, side-lobe suppression ratio (SLSR), maximum side lobe (MSL) and delay need to be optimized w.r.t. the grating design parameters, such as, length (L), index-change (δn), apodization profile and loss (α). In the first part of the research, a novel apodization profile to device FBG that can efficiently resolve strain and temperature in QDSN is proposed. Optical characteristics of the grating employing novel apodization are optimized w.r.t. L and δn. For the optimum grating based five-stage QDSN, dynamic range for the temperature measurement as high as 131.6°C and for the strain measurement as high as 1450με are obtained. Further, an isolation of 10.07 dB and the total isolation of 33.818 dB, highest among the other apodization profiles recently reported in the literature, are observed for the proposed FBG. In order to further enhance the sensing efficiency, slow-light π-FBG based QDSN is proposed. A novel π-FBG is designed by optimizing optical and sensing characteristics with respect to the parameters L, δn, α and employing the novel apodization profile proposed earlier in the research. Strain sensitivity as high as 8.380 $(\mu\varepsilon)^{-1}$ and temperature sensitivity as high as 91.064°C^{-1}, manifold higher than the maximum sensitivity reported in the literature, are achieved for the proposed slow-light π-FBG. Optimized slow-light π-

FBG is employed in a five-stage QDSN. Dynamic range for the strain measurement as high as 1469με and for the temperature measurement as high as 133°C are obtained. Finally, π-FBG based fiber Mach-Zehnder interferometer is proposed to develop ultrasonic acoustic sensor. With the optimized characteristics of π-FBG achieved at L = 5 mm, $\delta n = 1.2\times10^{-3}$ and employing the proposed novel apodization profile, strain sensitivity as high as 1.21321×10^{8}/ε and resolution as high as 4.1 fε/√Hz are achieved from the proposed sensing system. Observed strain sensitivity and resolution are much better than the best reported in the literature.

Table of Contents

List of Figures

List of Table

List of Acronyms

AE	Acoustic Emission
AFBG	Apodized Fiber Bragg Grating
AOM	Acoustic Optical Modulator
BLS	Broadband Light Source
BOTDR	Brillouin Optical Time Domain Reflectivity
CCD	Coupled Charged Detector
CFRP	Corban Fiber Reinforce Polymer
CMDE	Coupled Mode Differential Equation
CMT	Coupled Mode Theory
CPO	Coherent Population Oscillation
CRC	Canadian Communications Research Centre
DFB	Distributed Feedback
DWDM	Dense Wavelength Division Multiplexing
EDFAS	Erbium-doped Fiber Laser Source
EIT	Electromagnetically Induced Transparency
EMI	Electromagnetic Interference
FBG	Fiber Bragg Grating
FDM	Frequency Division Multiplexing
F-MZI	Fiber Mach-Zehnder Interferometer

FP	Fabry-Perot
FPI	Fabry-Perot Interferometer
FSI	Frequency Shifted Interferometer
FWHM	Full Width at Half Maximum
LDV	Laser Doppler Vibrometers
LLS	Laser Light Source
LPG	Long Period Grating
MLS	Modulated Laser Source
MMF	Multimode Fiber
MSL	Maximum Side-Lobe
NDT	Non-Destructing Testing
OCDM	Optical Code Division Multiplexing
OFDR	Optical Frequency Domain Refractometry
OFS	Optical Fiber Sensor
OPD	Optical Path Difference
OTDR	Optical Time Domain Refractometry
PCW	Photonic Crystal Waveguide
PID	Proportional Integral Derivative
PSFBG	Phase-Shifted Fiber Bragg Grating
PZT	Lead-Zirconate-Titanate
RH	Relative Humidity

RI	Refractive Index
SBS	Stimulated Brillouin Scattering
SDM	Space Division Multiplexing
SHM	Structural Health Monitoring
SLSR	Side-Lobe Suppression Ratio
SMF	Single Mode Fiber
SNR	Signal to Noise Ratio
SRI	Surrounding Refractive Index
SRS	Stimulated Raman Scattering
TDM	Time Division Multiplexing
TMM	Transfer Matrix Method
TOF	Time of Flight
US	Ultrasonic
UV	Ultraviolet
WDM	Wavelength Division Multiplexing
WSFL	Wavelength Swept Fiber Laser

Chapter 1 : Introduction and Literature Review

This chapter presents an introduction and literature review on optical fiber sensor (OFS) based structural health monitoring (SHM), its background and basic concepts. Sections 1.1 and 1.2 present an introduction of the thesis and evolution of optical fiber sensor (OFS), respectively. Section 1.3 discusses about various topologies used in the design of OFS. A short literature review on wavelength-division multiplexed fiber Bragg grating (WDM-FBG) sensing networks and the motivation to use it in the structural health monitoring is presented in section 1.4. Finally, section 1.5 elaborates organization of the thesis.

1.1 Introduction

Advancements in science and technology in the last couple of decades have made our lives comfortable beyond imagination. Infrastructures provided for electronics and communication engineering, civil engineering, computation, healthcare, energy etc. computing have substantially improved to aid daily personal as well as professional chores. Advent of artificial intelligence and machine learning has further improvised systems to transform them from traditional to the smart ones. In this transformation, sensors and data analysis associated with a system play an important role. Efficiency of sensors impacts performance of the systems, which we design and develop.

For a robust and reliable system, it is imperative to design a system in such a way that it can sustain for a prolonged duration. As we know, all types of engineering infrastructures, such as, railways, roads, bridges, tunnels, dams, wind, hydro or nuclear turbines, oil and gas wells, high power transportation lines to deliver electricity, aerospace, high-rise buildings, etc., deteriorate with time. This

deterioration occurs due to several reasons, for example overloading, error in design, environmental effects, and some unexpected events like earthquakes, Tsunami, etc. These factors change structures' health conditions in terms of several impairment parameters (measurands) such as, stress, strain, crack, tilt, deformation, displacement, corrosion, oxidation, etc. Therefore, for the safe and efficient exploitation of the structures, an inspection and maintenance are needed on a regular basis. The cost of personnel required to complete these processes in traditional manner is quite expensive. Alternatively, a smart and autonomous monitoring of structures' health condition is of prime importance in order to reduce inspection costs and to make the process more efficient. Thus, a robust, reliable, efficient, and intelligent system is the need of the hour. In this thesis, we propose to develop a solution for continuous structural health monitoring (SHM) for engineering infrastructures so that proper actions could be taken within a stipulated time frame, if the crisis arises.

A structural health monitoring (SHM) system can be described as a combination of devices that gives information, which helps in the implementation of a damage detection and its curing strategy for engineering infrastructures. Sensor is an integral part of a SHM system. A sensor is a device that converts changes in the magnitude of one physical parameter into another parameter, which not only can be measured more conveniently but also more accurately [1].

Various kinds of conventional sensors like anemometers, temperature sensors, servo type accelerometers, dynamic weigh-in-motion sensors, level sensing stations, displacement transducers, weldable strain gauges, piezoelectric sensor have been utilized for SHM of engineering infrastructures [2, 3]. Conventional sensors, however, have many limitations, such as, acceptable performance only under certain conditions and highly susceptible to (a) electromagnetic interferences (EMI), (b) radio frequency

interferences (RFI), and (c) turbulences provided by the nature. Moreover, these sensors hardly offer multiplexing and remote sensing capabilities. One of the possible ways to overcome these limitations is to device the system that exploits lightwave frequencies of the electromagnetic spectrum. As an example, a laser Doppler vibrometers (LDV) was demonstrated for an accurate displacement measurement of the bridges [4]. Although this sensor overcomes the limitations imposed by EM/RF interferences as the measurement is performed using light, but it does not offer multiplexing capabilities. Furthermore, the cost of sensing system is also very high, and the laser intensity may become dangerously strong in some situations [5]. Further, another key limitation of conventional as well as laser based traditional (holographic as an example) optical sensors is the fact that these sensors cannot be deployed in hazardous environment. A sensor having capabilities to operate in a hazardous environment, immunity to EMI and RFI, long-term performance, durability, and ability for multiplexing and remote-sensing is of great importance for many practical applications. In the next sections, a brief discussion on optical fiber sensors and their topologies are presented.

1.2 Optical Fiber Sensors (OFSs)

The adoption and exploitation of optical fiber has drastically impacted sensing technology since the major breakthrough invention of fiber optics for telecommunication in the early seventies [6]. An optical fiber is a cylindrical dielectric waveguide having a high refractive-index core and low refractive-index cladding. Depending on the core diameter, core and cladding refractive indices as well as the operating wavelength, optical fiber can be classified as (a) single-mode fiber (SMF) that supports only the fundamental mode and (b) multi-mode fiber (MMF) that supports more than one (fundamental) modes. Apart from nonlinearity effects, two

fundamental characteristics that severely affect the transmission efficiency of optical fiber and restrict the information-carrying-capacity are loss and dispersion (intermodal as well as intramodal dispersion). Loss is minimized by operating optical fiber communication system at 1550 nm. Intermodal dispersion is a characteristic feature of MMF and is obviously zero for SMF. On the other hand, intramodal dispersion for standard SMF is observed to be zero at 1310 nm and in the range of 15-19 ps/(km-nm) at around 1550 nm. It is for these reasons, SMF is used to design and develop optical fiber telecommunication systems and to design a sensing network that is capable of remote sensing applications.

At the early stage when the fiber optics was still evolving, transmission efficiency of optical fiber was observed to be profoundly affected by various external parameters, such as, pressure, macrobends, microbends, etc. Enormous efforts were made to nullify the sensitivity of optical fiber to these external parameters. However, soon it was realized that the sensitivity of optical fiber to various external parameters could be utilized for sensing applications, which motivated scientific community to use optical fiber as a sensor.

Any optical fiber sensor (OFS) system contains three main integrated parts – a sensor, a transmission medium, and an optoelectronics unit. The earliest "***Fotonics***" sensor was proposed to estimate location and spacing in the machine tool industry [7]. As OFS illustrated various advantages over traditional electronics and optical sensors, for example, reduced size and weight, immunity towards electromagnetic and radio interferences, ability to work in a harsh environment, reduced cost, versatility, reliability, compatibility to optical communication network, remote sensing, corrosion-free, and embedding capability [8, 9, 10].

The OFS can be broadly divided into two subcategories, extrinsic (hybrid) and intrinsic (all-fiber) sensors. In the extrinsic sensors, light emerges from an optical fiber to another medium, where it is modulated by measurand. The modulated light is again recollected by same or a different fiber, and is forwarded to a remote location for further processing. In the intrinsic sensors, external parameters modulate one or more physical properties of the propagating light e.g. phase, wavelength, polarization, and intensity within the fiber. As evident, an intrinsic fiber sensor can be further classified on the basis of the employed modulation scheme and can be termed, for example, as an intensity modulation based optical fiber sensor or a wavelength modulation based optical fiber sensor and so on. Most popular schemes among researchers in terms of ease of realization are intensity, phase and wavelength modulation. In general, extrinsic sensors are utilized for chemical and biomedical measurements [11, 12], while intrinsic sensors are primarily used for physical measurements and also utilized for SHM widely [13].

Sensors based on intensity modulation have more practical importance due to their simplicity in fabrication and compatibility with multi-mode optical fiber. The most popular scheme to achieve intensity modulation in optical fiber is to exploit the evanescent wave in the cladding. On the other hand, invention of in-fiber grating has significantly revolutionized the field of optical fiber sensors that exploits wavelength modulation scheme. Fiber gratings consist of periodic perturbation of refractive index, generally over a small length, with in the core of a single-mode fiber (will be explained later). They fall into two general categories based on the period of grating – short period grating or fiber Bragg grating (FBG) and long period grating (LPG). In addition to intensity and wavelength modulation, controlling the light in an optical

fiber has started a new area of sensing. Sensors exploiting this mechanism are known as slow-light fiber sensors [14].

1.3 OFS Topologies for Sensing Applications

OFSs that are deployed in various sensing applications, including structure health monitoring, can be developed in three different topologies [15, 16]:

- Single point sensor,
- Multipoint/quasi-distributed, and
- Fully distributed sensing networks

1.3.1 Single Point Sensor

1.3.1.1 Intensity/Wavelength modulation-based OFS

Since the first optical fiber sensor was reported in mid 1960s for vibration measurement, extensive research began in late 1970s to develop OFS that can monitor other important parameters, e.g., pressure, strain, relative humidity (RH), curvature, displacement, rotation etc. These sensors were targeted to monitor localized perturbation/parameters of interest. Primarily, technologies such as, intensity modulation/phase modulation/wavelength modulation were exploited to develop these OFSs. For example, intensity modulation through evanescent wave absorption was exploited to monitor RH in [17]. Similarly, as an example, wavelength modulation mechanism was exploited to monitor tilt by designing FBG based all-optical sensor in [18]. To be very specific, in-fiber Bragg gratings (FBGs) have become synonym to the optical sensing technology as for as real-field applications are concerned. The reason is, apart from inheriting the advantages of fiber optics, FBG sensors are characterized with additional advantages, such as, (1) inherently self-referencing, (2)

ease of designing spectral and phase response as per the requirement, (3) capability of multiplexing a large number of FBGs on a single fiber line, (4) ease of employing DWDM, spatial-division-multiplexing, time-division-multiplexing (TDM) and quasi-distributed sensing, (5) insensitive to the fluctuations in the irradiance of the illuminating source, (6) compatibility for the application in advance composite materials to name a few. A brief introduction on FBG is presented in next subsection.

1.3.1.1.1 An overview of FBG and its Sensing Applications

An FBG is a finite length permanent intra-core periodic perturbation of induced refractive index (RI) change along the fiber axis (Figure 1.1). This induced RI is due to the exposure of photosensitive fiber in an intense ultraviolet (UV) or excimer laser using phase mask or interferometric technique [19]. When a broadband light propagates through the grating, due to change in RI, multiple Fresnel reflection takes place along the grating length. The forward and backward propagating waves interfere constructively only when they satisfy phase matching (or the Bragg) condition.

The phase-matching condition states as [20]:

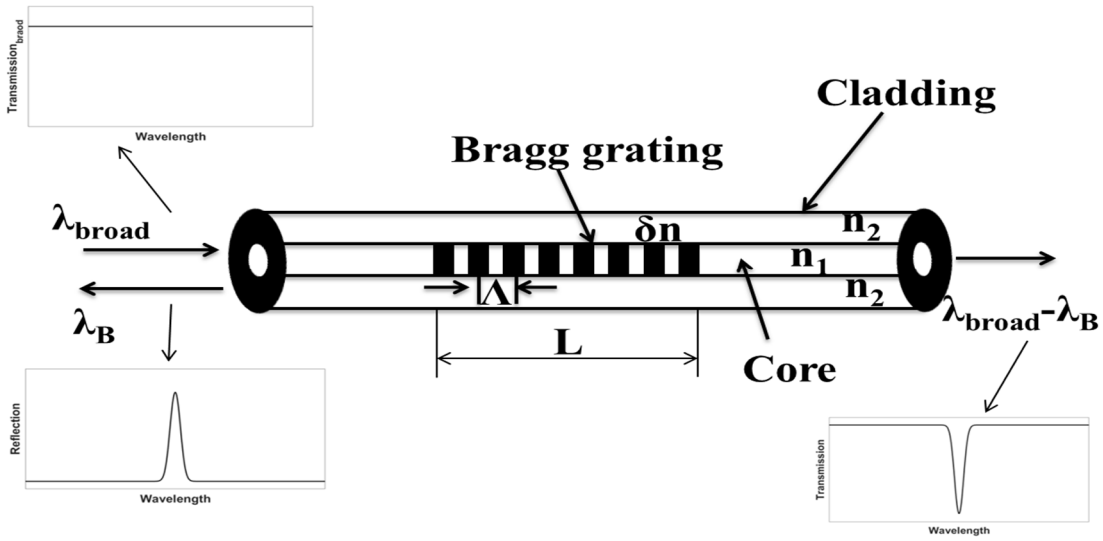

Figure 1.1: Schematic of FBG.

$$\beta_f - \beta_b = \frac{2\pi}{\Lambda} \tag{1.1}$$

where, β_f and β_b are the forward and backward propagation constant, respectively, and Λ is the grating period. For an FBG, β_b = - β_f, hence, the phase-matching condition becomes

$$2\left(\frac{2\pi n}{\lambda_B}\right) = \frac{2\pi}{\Lambda} \tag{1.2}$$

where, λ_B is Bragg wavelength, and n is the effective mode index in the fiber. Equation (1.2) may be simplified to the first-order Bragg condition as mentioned below.

$$\lambda_B = 2n\Lambda \tag{1.3}$$

The light that does not follow Bragg condition transmitted through FBG. Both n_{eff} and Λ depend on the strain and temperature, therefore, Bragg wavelength also becomes sensitive to strain and temperature. The change in Bragg wavelength due to longitudinal strain, ε, is given by,

$$\Delta\lambda_{B\varepsilon} = \lambda_B\left(1 - p_e\right)\varepsilon \tag{1.4}$$

where, p_e is the photo-elastic coefficient of the fiber and can be given as

$$p_e = \frac{n^2}{2}\left(p_{12} - \nu\left(p_{11} + p_{12}\right)\right) \tag{1.5}$$

where, p_{11} and p_{12} are the components of a strain-optic tensor, and υ is Poisson's ratio. A typical germanosilicate fiber exhibits wavelength–strain sensitivity of 1.2 pm/με at 1550 nm wavelength [21]. The change in Bragg wavelength due to temperature change is given as:

$$\Delta\lambda_{BT} = \lambda_B\left(\alpha + \zeta\right)\Delta T \tag{1.6}$$

where, $\alpha = (1/\Lambda)(\partial\Lambda/\partial T)$ is a thermal expansion coefficient ($\approx 0.55\times10^{-6}$ for silica), and $\zeta = (1/n)(\partial n/\partial T)$ is a thermo-optic coefficient ($\approx 8.6\times10^{-6}$ for a germanium-doped silica-core fiber). The wavelength-temperature sensitivity of 1550 nm FBG sensor is approximately 14 pm/°C [21]. The overall shift in Bragg wavelength due to strain and temperature is given as:

$$\Delta\lambda_B = \lambda_B(1-p_e)\Delta\varepsilon + \lambda_B(\alpha+\zeta)\Delta T \tag{1.7}$$

As can be observed from Eq. (1.7), FBG is inherently sensitive to strain and temperature perturbations both. This makes FBG an intrinsic optical fiber sensor for these two parameters. However, FBG sensors can be used to monitor any other physical parameter if a suitable methodology can be developed to map this other parameter into strain or temperature. Numerous FBG sensors are successfully developed to monitor various parameters of interests such as tilt [22], displacement [23], strain [24], temperature [25], humidity [26], pressure [27], magnetic field [28], refractive index [29], ultrasound waves [30], corrosion [31], vibration [32], weight [33], chemicals [34], biomedical [35, 36] etc. which are critically important in different engineering applications/industrial processes. In all the examples mentioned above, parameters of interest are strategically mapped in the strain domain.

One very important issue that arises and to be addressed for all such sensors is the cross-sensitivity of FBG towards temperature variations and resulted noise while deploying the FBG sensor in real-field applications. This issue is addressed by adopting a suitable temperature compensating mechanism [22]. Besides, there are various known techniques to modulate a grating to enhance sensing and optical characteristics of FBGs, such as tilting [37], phase-shifting [38], chirping [39], tapering [40], and apodization [41].

One very important point needs to be highlighted here. Demodulation of the information about the applied perturbations (e.g., strain, tilt, pressure, torsion etc.) is generally done by monitoring the wavelength shift by employing optical spectrum analyzer (OSA) or the FBG interrogator. However, demodulations of FBG sensors for ultrasonic waves are different from the static strain. It requires an instrument having sub-micron strain resolution [42] and over kilo-Hertz bandwidth [43, 44]. The tracking of the shift in the Bragg wavelength of FBG under an ultrasonic strain wave is usually not possible with an optical spectrum analyzer (OSA) due to its limitation in terms of sensitivity/resolution and demodulation speed. Demodulation techniques that needs to be employed in this case depends on the light source (broadband source/laser/Erbium-doped fiber laser/modulated laser) employed in a sensing system [45].

1.3.1.2 Interferometer based OFS

Optical fiber based interferometric sensors, such as, Fabry-Perot, Mach-Zehnder, Michelson, and Sagnec interferometers are also heavily exploited for monitoring physical parameters at a localized point. The working principle of interferometric sensors is based on the change in the phase of two light waves with the same frequency due to the external perturbations [46]. The first Sagnec interferometer was developed in 1980s as a fiber optic strain sensor for SHM [47, 48] and, since then, it has been utilized in various practical applications. A white-light fiber optic Michelson interferometer was proposed for two-dimensional strain measurement inside a concrete structure [49]. Michelson and Mach-Zehnder interferometer sensors employing photonic crystal fibers and long period grating (LPG) have been primarily preferred for velocity [50], refractive index [51], and temperature [52] measurements.

Further, photonic crystal fiber based Sagnac interferometer was deployed to monitor pressure in a localized region in [53].

Fiber-optic Fabry-Perot interferometer (FPI) sensors are one of the best candidates for SHM [54, 55]. The typical strain resolution of FPI sensors is 0.01% of full scale, and measurement range can extend up to ±5000 με [56]. A gold deposited extrinsic FPI sensor was developed for dynamic strain measurement [57]. Zhou *et al*. [58] proposed an extrinsic FPI strain sensor to investigate damage in the smart composite beam. An FPI fiber-optics sensor in [59] was used to monitor strain in concrete structures. A moderate multiplexed extrinsic FPI strain sensor was also proposed for the strain measurement of composite structures [60]. The major drawback of interferometric sensors is their weak multiplexing capability, which limits their application for large civil infrastructures as they can measure a relatively low number of points.

1.3.1.3 Slow light based OFS

Slow-light fiber sensors have evolved as a new class of OFS for various applications to monitor the localized parameter of interest. Initially slow-light in optical fibers was employed for various applications in optical communication systems, such as, tunable delay line for data synchronization, optical buffering, and optical signal processing [61]. Slow-light in a medium has a smaller group velocity of light than the velocity of light in a vacuum. Slow-light fiber sensors exhibit better sensitivity than conventional fiber sensors. Standard optical fibers show weak interaction between light and fiber material, and offer a very high group velocity of $\sim 2\times10^{8}$ m/s. The group velocity, however, in fiber can be reduced by either using a high refractive index material [62] or periodic/aperiodic variation of induced index along the finite length of a fiber [61] Therefore, based on the interaction of light,

slow-light in the fiber can be broadly divided into two classes: material dispersion slow-light and structural dispersion slow-light [63].

Slow-light based on material dispersion relies on the nonlinear gain and loss in stimulated Brillouin scattering (SBS) and stimulated Raman scattering (SRS) [64, 65], coherent population oscillation (CPO) in absorption and amplification media [66], and electromagnetically induced transparency (EIT) [67]. Generally, in an optical communication system, stimulated light scattering processes are harmful as they restrict upper power level or transmission distance of an optical signal. However, in a dedicated prototype, SBS and SRS can be harnessed to generate slow-light effect. The first slow-light based on SBS in a fiber was experimentally illustrated by Song *et al.* [68] and Okawachi *et al.* [69], whereas, Sharping *et al.* [70] demonstrated slow-light for SRS.

In structural slow-light, propagating light interacts with a large number of periodic resonant structures. The period of resonant structures is of the order of a propagating light wavelength. The well-known examples of in this category are photonic crystals [71], Fabry-Perot etalon [72], fiber ring resonators [73], and fiber Bragg gratings (FBGs) [74, 75].

Material dispersion based slow-light medium has the ability to produce very low group velocity. However, these systems need power supply to the fiber and long fiber lengths in the case of SBS [76], whereas, structural dispersion based slow-light medium is robust and passive, and can be used for developing functional applications. Therefore, slow-light based fiber optics can be used extensively in sensing applications.

A temperature sensor based on SBS slow-light in 2-m fiber was experimentally demonstrated in [77]. It shows a temperature dynamic range of 25°C and resolution better than 1.0°C. An enhanced sensitivity rotation sensor based on slow-light in gyro structure was experimentally presented by Y. Zhang *et al*. in [78]. The experimental result revealed that due to slow-light effect, sensitivity of the system is enhanced by 2.5-fold. A high sensitive and large dynamic range fiber MZI demodulation system utilizing tunable slow-light in polymer-infiltrated PCW in one arm is experimentally demonstrated for fiber Bragg grating (FBG) displacement sensor in [79]. The proposed sensing system exhibits a displacement sensitivity of 1.035 rad/mm for wide measurement range of 35 mm. Q. Wang *at el.* [80] theoretically as well as experimentally demonstrated a micro-displacement sensing system based on slow-light in fiber double-loop coupled resonator. The experimental results provide 10 με displacement resolutions over 0 – 350 μm displacement measurement range along with 32.0668 ns delay in the system. An angular velocity sensor based on optical gyroscope containing double-ring slow-light structure had shown two-fold higher sensitivity than the interference type sensors [81]. Recently, W. S. Pang *et al.* [82], experimentally demonstrated second order Brillouin slow-light in fiber for temperature sensing. The delay – temperature sensitivities of proposed first order and second order systems were obtained as 1.126 ns/°C and 1.917 ns/°C, respectively. The second order sensitivity is 1.7 times better as compared to the first order sensitivity.

Further, the presence of a periodic variation of refractive index in FBG creates a band of finite reflections in the frequency space, where light is not allowed to propagate. In other words, FBG reflects light in the vicinity of Bragg wavelength, while the light sufficiently detuned from the Bragg wavelength is transmitted. However, on the edges of photonic bandgap, frequencies are propagated at a reduced

group velocity. Thus, FBG supports structural slow-light and, shows an enhanced sensitivity and resolution as compared to the conventional FBG [83]. Therefore, several slow-light FBG sensors have been proposed for highly sensitive and high-resolution measurements.

1.3.2 Multi-Point/ Quasi-distributed OFS

In many practical situations, requirement of the accurate assessment of the parameter of interest is not localized, but distributed over the entire structure/region of observation. In such cases, sensors should be capable of covering hundreds or thousands of sensing points spanning a large area of the structure/region. This is done by multiplexing large number of point sensors, in series, along a single optical fiber, that ways, building a multipoint/quasi-distributed OFS network. Grating based sensors, especially fiber Bragg grating (FBG) sensors are mostly utilized for quasi-distributed sensing network applications [84].

The distinct properties of an FBG sensor, which make it best optical sensing component among other OFSs, are its wavelength encoded measurement and ease of multiplexing. It is to mention that the wavelength encoded measurement is less prone to signal amplitude fluctuations and several FBG point sensors can be multiplexed on a single fiber. Mainly, two types of multiplexing techniques proposed for real field application in large engineering structures are wavelength-division multiplexing (WDM) and time-division multiplexing (TDM) [85].

1.3.2.1 WDM-FBG Sensing Network

The WDM technique is the most straightforward interrogating method, in which each FBG sensor is assigned a unique slice of wavelength in an available spectral width of broadband source without getting operational region of individual FBGs

overlapped. Figure 1.2 illustrates a WDM-FBG sensing network with scanning F-P filter. High reflective FBG sensors, which are not identical, are multiplexed along a single optical fiber to yield WDM sensing network. Typical wavelength measurement accuracy demonstrated by WDM interrogation systems is 1 pm. This is equivalent to temperature and strain measurement accuracies of 0.1°C and 1με, respectively [86]. Furthermore, a WDM system can be utilized for long-distance quasi-distributed measurements [87]. The maximum number of FBG sensors along a single fiber in a WDM system depends on the optical bandwidth of a broadband light source, operation range and optical characteristics of each FBG sensor, and tuning range of a tunable filter. Typically 40 FBG sensors can be interrogated by a WDM system due to limitation imposed by optical bandwidth of a broadband light source [86]. However, the number of sensors can be increased by using hybrid multiplexing techniques, such as, WDM and TDM [88], WDM and spectral profile division multiplexing (SDM) [89], WDM and frequency-shifted interferometry (FSI) techniques [90]. It can also be augmented by optimizing inherent optical characteristics of FBG, such as, reflectivity, full-width at half maximum (FWHM), and side-lobes [91].

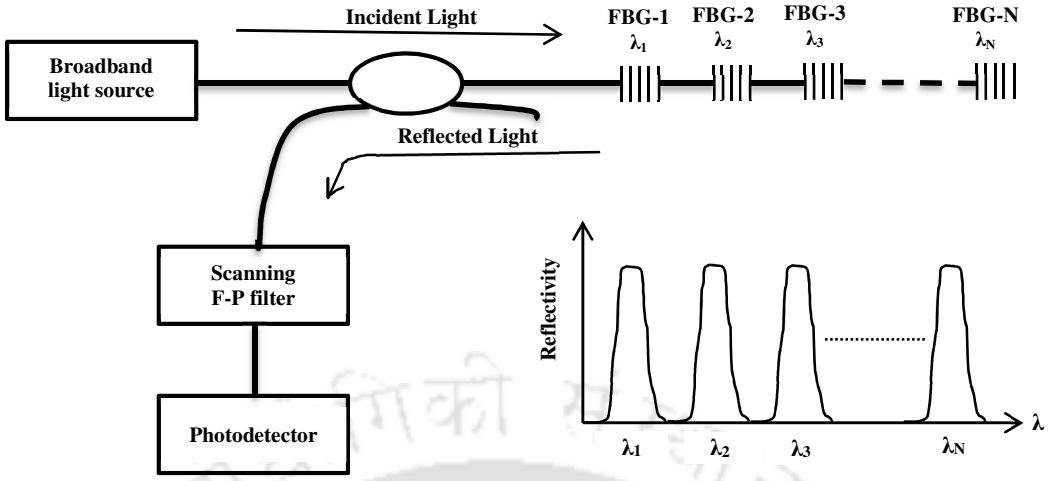

Figure 1.2: WDM-FBG sensing network interrogation system.

1.3.2.2 TDM-FBG Sensing Network

TDM systems increases total number of FBG sensors to be used in the single fiber. In this system, multiple FBGs that are virtually identical and each characterized with week reflectivity (typically 4% reflectivity) are multiplexed along the fiber. Narrow optical pulses are launched into the single optical fiber that carries these multiple FBG sensors. The separation between two adjacent sensors depends on the width of the pulse launched in a fiber, as shown in Figure 1.3. If the pulse width is T and the mode effective index in the fiber is n, then the separation between two adjacent FBG sensors (d) needs to be maintained at $d > cT/2n$, where c is the velocity of light in the free space. Individual FBG sensors are distinguished by the measurement of the time-of-flight (TOF) of the launched signal upon returning to the photodetector. In comparison to the WDM technology, TDM technology provides large measurement range and does not require a coherent source [86].

However, this technology has some disadvantages, such as requirement of pulse modulation, optical amplification, high speed switching circuits and the low data acquisition rate of the system. Since it interrogates every individual FBG sensor, therefore, measurement time increases linearly with the number of sensors [92]. The narrow temporal pulses in TDM systems have wide-bandwidth in the frequency

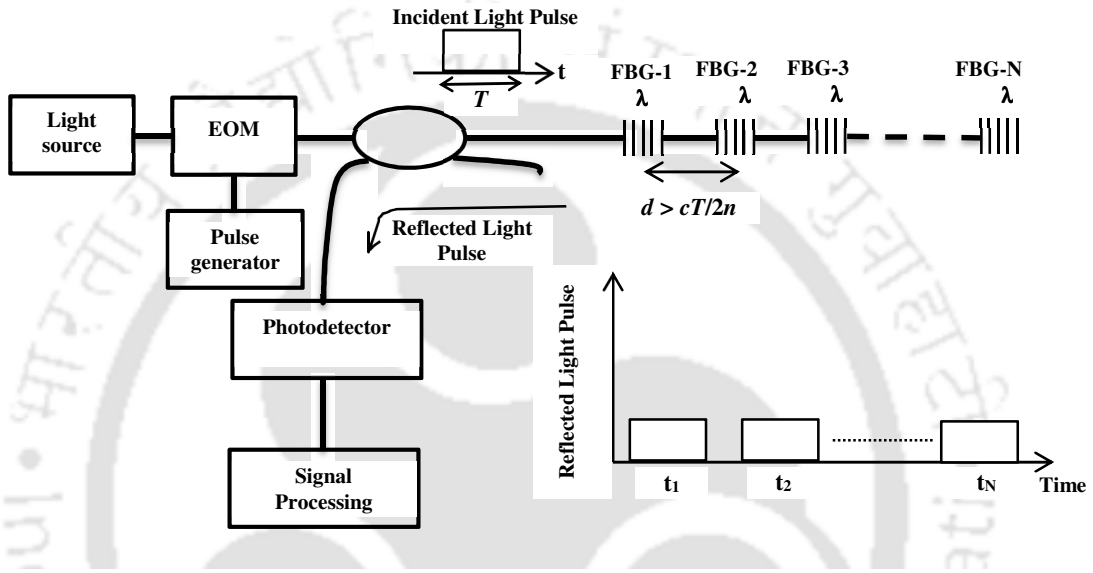

Figure 1.3: TDM interrogation based FBG sensing network. EOM = Electo-optical modulator.

domain, which results in low reflected power from weak FBG sensors and, thus, reduces signal-to-noise ratio (SNR). Further, TDM technology exhibits a cross-talk and shadowing effect due to near-identical FBGs [93].

The cross-talk can be minimized by utilizing ultra-weak fiber Bragg grating (uwFBG) sensors in the network. Recently, in-line identical uwFBGs with −37 dB to −50 dB reflectivity had been realized experimentally in [94]. These uwFBGs reduced the crosstalk between multiple gratings, and increased number of FBG sensors in a single fiber greatly. However, such large-scale grating cannot be interrogated by an ordinary TDM interrogator. To interrogate a large-scale uwFBG sensor array, various probing technologies, such as optical time-domain reflectometry (OTDR) [95], optical

frequency domain reflectometry (OFDR) [96], and frequency-shifted interferometry (FSI) [97] have been proposed in the literature.

1.3.2.3 Real-Field Application of WDM-FBG Sensing Networks

During the past few years, FBG sensing networks have been heavily employed for the structure health monitoring (SHM) of almost all the major engineering structures, such as bridges, tunnels, highway and railways transports, high-rise towers, aviation transports, etc. [98]. A consolidated study on WDM-FBG sensing networks being conducted for analyzing health of the structures in real time is presented below for completeness.

The performance evaluation of Mjosund bridge in Norway, which is 350 m long steel box road bridge with concrete decking, was carried out using a network of 32 FBG sensors over 18 months long period. FBG sensors were divided into eight parallel fiber channels, and each channel contained a group of four serially multiplexed FBG sensors spaced at 5 nm across 20 nm spectral width of the source spectrum. The return signals from the array of sensors were interrogated using scanning Fabry–Perot based wavelength division multiplexing (WDM) technique. This system could interrogate up to eight sensors in each channel. The grating used in this system was 10 mm long and, had reflectivity more than 90% along with 0.2 nm bandwidth [99].

The total 40 multiplexed FBG sensors divided into three arrays were installed in different locations (hanger cables, rocker bearing, and supporting structure) of Tsing Ma bridge (TMB), which is the longest (1377 m) bridge of the world carrying both road as well as railway traffic. A low cost and high-speed demultiplexing/interrogation system (DEMINSYS) was utilized for sensors array for

the structural health monitoring of Tsing Ma bridge. In this SHM system, all gratings were spaced 4 nm apart. For the temperature compensated measurement, addition strain-free FBG sensors were installed at different sensing points [86].

A two-channel WDM-FBG sensing network was utilized to measure loading capacity of an old railway bridge, which was being demolished in Örnsköldsvik, Sweden under European Union's "Sustainable Bridges" project. First channel had six serially multiplexed FBG sensors and second channel contained four FBG sensors. One sensor in the first channel was used for temperature compensation. Further, all sensors were embedded into Carbon Fiber Reinforced Polymer (CFRP) rods, which made FBG sensing system installation easier and performs efficiently during maintenance of an existing bridge as well. Signals returned from the sensors of each array were interrogated by scanning Fabry-Perot demultiplexing technique. At shear failure loading of the bridge, strain induced in the sensor was found to be 4000 με [100].

The structural health monitoring of 50 years old rail bridge situated in Frövi, Sweden in terms of strain, displacement, and crack opening size using the same sensing network was reported in [101] for a very moderate strain loading. During monitoring, the specimen was interrogated by eight parallel channels with eight sensors per channel. Further, FBG sensors were integrated into CFRP rods and tubes. The CRPF rods were installed in the lower part of the bottom slab using near surface mounted reinforcement (NSMR) technique, while tubes were placed in a hole in the upper part [101].

A long-term monitoring system based on WDM-TDM-FBG sensing network had been developed for concrete bridges for measuring physical parameters, such as strain, temperature, and vertical displacement. In this system, 30 strain sensors were

placed in three parallel fiber channels containing 10 serially multiplexed FBG sensors in each channel [102].

G. Kister *et al.* [103] developed a network of 16 FBG sensors to measure strain at different sections of 50 m foundation concrete pile. The multiplexed FBG sensors were 10 mm long and were separated by 5 nm. The reflected Bragg wavelength from the sensors were interrogated by an optical spectrum analyzer (OSA) with the resolution of ± 5 pm.

A wavelength multiplexed FBG sensor network was designed for the long-term measurement of operational load in a wind turbine blade. Bragg signals returned from five multiplexed FBG sensors were interrogated by a compact polychromator, which contained an imaging diffractive grating and 2048-pixel CCD photo-receiver line covering 720 nm – 890 nm wavelength ranges. The FBG sensors had grating length of 5 mm, reflectivity varying from 30% - 90% and a spectral width of 0.1-0.3 nm. The maximum strain measured by this system was 2000 με. It is to mention that a separate sensor was used for temperature compensation [104].

Dynamic strain and bending deflection of 70 m high wind turbine tower under feathering and blade starting conditions were measured using an array of ten WDM-FBG sensors. Eight FBG sensors deployed at four different positions of this tower for measurement of dynamic strain and two FBG sensors were utilized for temperature compensation. A high-speed FBG interrogator was especially designed for this wind turbine structure [105].

K.-S. Choi *et al.* used a two-channel fiber optic sensing system to measure tip deflection due to static strain of an 11 m long turbine blade. Each channel contained ten serially multiplexed FBG sensors, out of which, six FBG sensors were employed

for strain measurement, one for temperature measurement, and remaining three sensors for the temperature compensation. Signals returned from these sensors were detected using a commercialized FBG interrogator [106].

WDM-FBG sensor network employing two FBG sensor arrays with five sensors in each array was used for measuring local as well as global responses of a maglev guideway such as local stains, curvatures, vertical deflections, and frequencies. A wavelength-swept fiber laser (WSFL) interrogator was utilized to detect shift in the Bragg wavelength of sensors [107].

A two-array WDM-FBG sensing network was designed for impact location detection and energy in CRFP rods containing five FBG sensors in each array. In these sensors, one sensor was used for temperature compensation and remaining sensors were employed to calculate structural stain. The wavelength separation between two consecutive sensors was 10 nm [108].

A WDM-FBG based acoustic sensing network was designed for the structural health monitoring of a marine structure [109]. This system used BLS and optical filter demodulation schemes. The experimental results of acoustic measurements on glass and plate specimens exhibited that the performance of FBG sensor was similar to commercially available PZT sensors.

An adaptive wavelength demodulated four-channel WDM-FBG sensing network was designed to detect ultrasonic signals. The sensing system had four tunable distributed feedback (DFB) semiconductor lasers and, wavelength lock-in technology based on a self-scanning device and proportional-integral-derivative (PID) method. All FBG sensors were 5 mm long and their wavelengths were separated by 5 nm in the wavelength domain. The experimental results illustrated that the proposed system

could detect the maximum 1 MHz ultrasonic frequency. Further, the proposed system was able to detect acoustic emissions even in the presence of a quasi-static background having temperature and vibrations [110].

Most recently, W. Li *et al.* [111] experimentally demonstrated a novel water leakage detection method using a thermal sensing cable, which was formed by the coupling of heating cable and WDM-FBG quasi-distributed temperature sensing network. In this method, ten FBG sensors were serially multiplexed in a 2 m long fiber with an equal spacing of 0.18 m and had 3 nm differences in their central wavelengths.

1.3.3 Fully Distributed Sensing Network

A distributed OFS network fully utilizes optical fiber as a sensor by detecting changes in the optical properties of light scattered all along the fiber length due to deviations in physical parameters locally. When a light is launched in an optical fiber, it interacts with the constituent atoms and molecules. This interaction gives rise to a time dependent polarization through induced dipole moment. An oscillating dipole gives rise to the secondary electromagnetic radiation. This process is known as the scattering of light [112]. Depending on the mechanisms, scattering of light can be elastic (Rayleigh scattering) or inelastic (Brillouin and Raman scatterings). Majority of the distributed optical sensing mechanisms deploy one or more among Rayleigh, Brillouin and Raman scatterings.

Rayleigh scattering in the fiber is the scattering of light off random density fluctuations that exist in the dielectric material of the fiber. This scattering is a linear and elastic phenomenon. Therefore, wavelength of the scattered light is same as that of the incident light as illustrated in Figure 1.4 [64]. The Rayleigh scattered light

component is utilized for the measurement of attenuation profile of a long-haul optical fiber link using Optical Time Domain Reflectometry (OTDR). The measured attenuation profile using OTDR play a crucial role in localizing breaks, in the evaluation of splices and connectors, and in the assessment of overall quality of a fiber link [15].

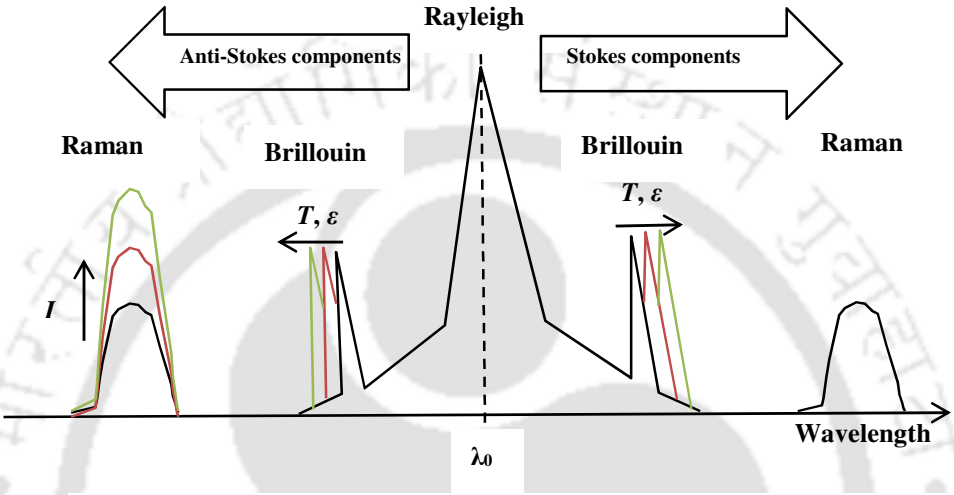

Figure 1.4: The Rayleigh, Raman, and Brillouin scattering effects in optical fibers **[64].**

Brillouin and Raman scatterings are inelastic physical phenomenon. Both of these scatterings generate two spectral components around an exciting (pump) wavelength by emitting low-energy photons (Stokes emissions) and high-energy photons (anti-Stokes emissions) as shown in Figure 1.4. Brillouin scattering observed in a fiber is due to the interaction of incident light wave with acoustic phonons. Acoustic phonons consist of collective vibrations of the atoms and molecules. On the other hand, Raman scattering results due the interaction of incident light wave with optical phonons. A phonon is a quantum of vibrational energy in a lattice. Further, it is important to mention that anti-stokes amplitude emission of Raman scattering is temperature (T) dependent, whereas stokes amplitude emission is temperature independent. It is to state further that Brillouin Stokes and anti-Stokes drifts are both strain (ε) and temperature (T) dependent [113]. Therefore, Brillouin scattering based distributed

fiber optics sensing networks are exploited for both strain and temperature measurements [64], while Raman scattering is utilized for distributed temperature sensing [114].

Brillouin and Rayleigh scatterings can be detected both in time and frequency domains using Optical Time Domain Reflectometry (OTDR) and Optical Frequency Domain Reflectometry (OFDR). It is found that Raman scattering can be interrogated using only OFDR [112].

In addition to sensing applications, stimulated Brillouin scattering (SBS) based slow-light has also been utilized for optical communication [115]. However, application of SBS based slow-light for distributed sensing is very limited. Slow-light based distributed strain and temperature sensing networks were demonstrated in [116] and [117], respectively. Strain resolutions of 13 με, spatial resolution of 15 m, and strain sensitivity of 0.3 ns/ με were achieved in [116] for strain in the range of 0-400 με in a 100-m fiber specimen [116]. The temperature sensitivity of 0.90 ns/°C and the resolution of 0.7°C were reported in [117] for temperature sensing networks.

Although distributed OFS networks have capability to monitor almost all engineering structures, they have limited spatial resolution, accuracy, and dynamic range. It is to mention that FBG based quasi-distributed OFS networks exhibit better resolution. Therefore, in SHM, quasi-distributed FBG optical sensing networks are primarily employed [118].

Based on our detailed study, it has been established that FBG sensing networks have wide applicability in the area of structure health monitoring (SHM). Thus, in the next section, motivations behind the proposed work along with objectives are presented.

1.4 Motivation

In all the research work, reviewed in the present chapter, uniform FBG sensors were employed in the sensing network for multi-point/quasi-distributed sensing applications to perform structural health monitoring. In SHM systems, multi-point sensing with accurate sensing data is very crucial and any deviation in the sensing data from any of these multi-point sensors leads to false diagnosis. However, as mentioned in the section 1.3.2.1, number of sensors in the WDM sensor system is limited by the bandwidth of the light source, dynamic range of each FBG sensor and the optical characteristics of each FBG sensor. Bragg grating with narrow full-width-at-half-maximum (FWHM) and greater degree of side-lobe suppression ratio (SLSR) are desirable and critically important in order to increase the number of FBGs and to devise efficient and optimized WDM/quasi-distributed sensing network for a given source-bandwidth. As an example, side-lobe suppression ratio (SLSR) is one of the key spectral indices for accuracy evaluation of demodulation results [119]. The SLSR can be enhanced by utilizing appropriate apodization scheme. Thus, advanced FBG sensors employing complex grating structures in order to realize desirable spectral characteristics are of tremendous importance for its applications not only in optical communication systems but also in all-optical WDM sensing systems. The main objective of the proposed research work is to device novel FBG structures for its efficient application in quasi-distributed sensing network and to enhance sensing capabilities. The following goals are set to achieve main objective of the proposed research work.

- A novel apodized FBG is proposed for strain/temperature measurement for WDM quasi-distributed sensing network. This requires optimization of optical

characteristics of FBG that are critically important for optical communication and sensor applications, e.g., reflectivity, FWHM, side-lobe suppression ratio (SLSR), maximum side lobe (MSL).

- Further, slow-light peaks in π-FBG are free from the side-lobes. Hence, slow-light π-FBG based quasi-distributed sensing network is proposed to enhance sensing capability.
- Finally, a combination of π-FBG sensor and fiber Mach-Zehnder interferometer (F-MZI) interrogation is proposed to develop a high sensitive ultrasonic acoustic sensing system.

It is to mention that rigorous theoretical study and analysis for the optimization of FBG sensor's characteristics and to simulate response-characteristics of quasi-distributed sensing network are performed employing couple-mode-theory and transfer-matrix-method. The thesis organization is presented in the next section summarizing overall proposed research work.

1.5 Thesis Organization

The thesis is organized as follows:

- **Chapter 1:** This chapter provides an extensive literature review in order to establish foundation of the research work presented in this thesis. It also lays down objectives of the proposed work and methodologies used to achieve these objectives.
- **Chapter 2:** In this chapter, important concepts, principles and techniques to analyze spectral characteristics of a fiber Bragg grating are presented. Coupled-mode theory (CMT) and transfer matrix method (TMM), the most powerful technique to understand the optical response characteristics

of uniform as well as nonuniform FBGs, are discussed. Some of the key parameters defining the optical characteristics of FBG that play crucial role in optical communication and WDM quasi-distributed sensing applications are highlighted at the end of the chapter.

- **Chapter 3:** In this chapter, a novel (symmetrical) apodization profile is proposed for tailoring and controlling key optical characteristics of FBG for its efficient application in a quasi-distributed sensing network. Objective of designing FBG for quasi-distributed sensing is to achieve better efficiency, measurement accuracy, high SNR, minimum channel-cross-talk and a large dynamic range. Optical characteristics, e.g., reflectivity, FWHM and the side-lobe suppression which are critically important for WDM sensing applications are optimized. While doing so, predominant focus is to achieve greater degree of side-lobe suppression without much compromise with reflectivity and FWHM. A rigorous and comparative analysis is carried out for the FBG employing proposed as well as the elite and the recently reported apodization profiles. Among all the apodization profiles included in the theoretical analysis, best side-lobe suppression characteristics, FWHM and reflectivity are observed for the proposed apodization profile at optimum grating parameters. These features establish that the proposed FBG is most suitable for quasi-distributed sensing applications. The proposed FBG with optimized characteristics is then employed in a five-stage quasi-distributed temperature and strain sensing network to analyze its application efficiency. During the study, it is found that the proposed apodization profile for quasi distributed sensing networks is better than the apodization

profile proposed in literature with respect to guard band and isolation between adjacent sensors.

- **Chapter 4:** In this chapter, optical (transmissivity and delay) and sensing characteristics of slow-light π-FBG are theoretically investigated. A π-FBG exhibits single and high delay peak in the delay spectra, which can be used for multipoint/quasi-distributed sensing networks. The motivation behind the research investigation is to develop an efficient all-optical quasi-distributed sensing network based on slow-light π-FBG and to analyze its response characteristics. To do so, optical and sensing characteristics of slow-light π-FBG are optimized with respect to the grating parameters (δn, L, α and the apodization profile). Apodization profile proposed in Chapter 3 is employed to design π-FBG. In comparison to the reported highest sensitivities reported in the literature, strain sensitivity enhancement of more than two-fold and temperature sensitivity enhancement of more than four-fold are achieved by the proposed grating structure. Finally, the slow-light π-FBG with optimized optical and sensing characteristics is employed in a five-stage quasi-distributed strain and temperature sensing network to analyze its application efficiency.
- **Chapter 5:** In this chapter, a combination of π-FBG and unbalanced fiber Mach-Zehnder interferometer (F-MZI) is theoretically analyzed and optimized for the highly sensitive ultrasonic acoustic sensing applications. Numerical investigations show that π-FBG ultrasonic sensor exhibits better sensitivity at high frequency as compared to the conventional FBGs ultrasonic sensors. This is because of the fact that light at the resonance frequencies of the strong ultra-narrow transmission peak within the stop

band of π-FBG undergoes strong localization resulting in a significantly higher group delay and hence, the sensitivity. Optical characteristics of π-FBG are optimized for ultrasonic acoustic sensing application w.r.t. L and δn. Further the sensor characteristics is optimized w.r.t. the optical path difference (OPD) of F-MZI. Proposed sensing system shows the theoretical highest strain sensitivity of $1.21321\times10^{8}/\varepsilon$ and a theoretical dynamic strain resolution of 4.1 fε/√Hz. The achieved strain resolution provides a theoretical wavelength shift resolution of 4.9×10^{-9} pm, which is much better than the reported values in the literature.

- **Chapter 6:** In this chapter, summary of the proposed research work is presented. Future scope of the proposed research work is also outlined and a roadmap is drawn to extend the work proposed in this thesis.

Chapter 2 : Theory of Fiber Bragg Gratings

In this chapter, a brief overview of the theory and simulation techniques for FBG is presented. Various theoretical techniques for developing mathematical model for understanding the physical mechanism of the interaction of guided modes inside the grating region of an optical fiber are briefly discussed in section 2.1. Coupled-Mode theory, the most popular and widely used theoretical technique among all is presented in section 2.2. Section 2.3 highlights key parameters defining the optical characteristics of FBG that play pivotal role in communication and sensing applications of FBG. Finally, summary of the chapter is presented in section 2.4.

2.1 Introduction

FBG is a periodic refractive-index perturbation within the core and along a specified length of the optical fiber. Realization of permanent grating structure within the core of an optical fiber was first demonstrated by Hill *et al.* in 1978 at the Canadian Communications Research Centre (CRC), Ottawa, Ont., Canada [120]. They launched intense Argon-ion laser radiation at 488 nm into a germanium-doped optical fiber. Due to this internal exposure, a permanent and narrowband grating structure was formed over the entire length of the fiber. As a result, almost all the light launched into the fiber was reflected and the grating structure acted as the filter. Meltz *et al.* [121] demonstrated a more efficient formation of grating structure while exposing the optical fiber externally from the cladding side to a radiation at one-half of this wavelength, *i.e*. 244 nm, that falls in the ultraviolet region of the spectrum. It was a major breakthrough in the grating writing technology as it has enabled the fabrication of FBG that will reflect any desired wavelength as per the need of the application. Several other methods are proposed for the fabrication of grating [20].

Out of these, phase mask technique is one of the most popular methods for the fabrication of FBG [122].

Wave propagation mechanism in an optical fiber can be analyzed by solving Maxwell's equations. Under the weekly-guiding approximation, solution of Maxwell's equations turns out to be a set of discrete, mutually orthogonal, transversely (linearly) polarized guided modes. Once excited, while propagating down the optical fiber, these distinct modes do not interact with each other and no coupling of power occurs between them if the fiber is in ideal condition (absence of any deviation from the cylindrical symmetry of the optical fiber structure, bending and any periodic phase/amplitude perturbation). However, in the presence of periodic perturbation such as Bragg grating structure within the fiber core, specific guided modes may get coupled. Various techniques have been developed for the analysis of field propagation and the coupling characteristics in the corrugated structure such as FBGs. These are coupled-mode theory, Rouard's method, Blotch theory, etc. [20]. All these techniques have diverse degree of complexity and advantages. The most widely used technique among these is Coupled-mode theory. Using this technique, a set of first-order differential equations is obtained describing the change in the amplitude of the electric-fields along the fiber, which have analytical solutions for uniform periodic perturbations such as the grating structure.

2.2 Coupled-Mode Theory (CMT)

In an optical fiber, if the dielectric constant varies periodically along the direction of wave-propagation (usually taken as the z-axis), total polarization is defined as:

$$\vec{P} = \varepsilon_0 \left[\varepsilon_r - 1 + \Delta\varepsilon(z) \right] \vec{E}_{lm}, \quad z \in (0, L) \tag{2.1}$$

where $\vec{E}_{lm}$ is the electric field associated with the guided mode of index *lm*, ε_r is the unperturbed relative permittivity (dielectric constant), $\Delta\varepsilon(z)$ is the perturbed permittivity along the fiber axis (z-axis) and L is the grating length. In the case when the modulating refractive index perturbation is small compared to the unperturbed refractive index (n) of the fiber core, applying constitutive relation between permittivity and the refractive index gives $\Delta\varepsilon(z) = 2n\delta n(z)$. Here, $\delta n(z)$ is periodic refractive index modulation along the fiber core and can be described as:

$$\delta n(z) = \overline{\delta n}\left(1 + f(z)\nu\cos\left[\frac{2\pi}{\Lambda}z + \phi(z)\right]\right), \quad z \in (0, L) \tag{2.2}$$

where $\overline{\delta n}$ is the refractive index change spatially averaged over a grating period, $f(z)$ is the apodization profile function, ν is the fringe visibility of the index change, Λ is the period of the grating, and $\phi(z)$ is the grating chirp.

While employing coupled-mode theory to analyze such structures, ideal-mode approximation is used. Under this approximation, the total transverse component of the electric field within the fiber carrying perturbation, $E_t(x, y, z, t)$, can be described as a superposition of *j* ideal modes (guided modes of an unperturbed, ideal optical fiber). Thus,

$$E_t(x, y, z, t) = \sum_j \begin{bmatrix} A_j(z)\exp\left(i\left(\beta_j + i\alpha\right)z\right) \\ +B_j(z)\exp\left(-i\left(\beta_j - i\alpha\right)z\right) \end{bmatrix} \xi_{jt}(x, y)\exp(-i\omega t) \tag{2.3}$$

where $A_j(z)$ and $B_j(z)$ are slowly varying amplitudes of the j^{th} guided mode of the unperturbed ideal optical fiber traveling in the $+z$ and $-z$ directions, respectively; $\xi_{jt}(x, y)$ is the transverse field distribution and β_j is the propagation constant of the j^{th} guided mode of the unperturbed ideal optical fiber, ω is the angular frequency, and

α is the attenuation coefficient which is a measure of total fiber loss. Attenuation coefficient can be neglected for the conventional gratings owing to the weak modulation index and the short grating length. However, it cannot be ignored for the slow-light gratings, which are generally strong gratings or long length gratings. Transverse field distribution $\xi_{jt}(x,y)$ obeys the following orthogonality condition:

$$\iint \xi_{jt}^{*}(x,y)\xi_{kt}(x,y)\,dxdy = \frac{2\omega\mu_0}{|\beta_j|}\delta_{jk} \tag{2.4}$$

where μ_0 is the magnetic permeability, and δ_{jk} is Kronecker's delta which is unity for $j = k$ and zero for $j \neq k$.

In order to study the effect of periodic perturbation such as Bragg reflection grating, scalar-wave-equation (which reduces to the scalar Helmholtz equation) is solved for the total transverse field within the fiber carrying the perturbation and defined in Eq. (2.3). For the case perturbation is small ($\delta n << n$), this process is simplified by applying the slowing varying amplitude (SVA) approximation that requires $\frac{d^2}{dz^2}A_j \ll \beta_j \frac{d}{dz}A_j$ [20]. Resulting coupled-mode differential equations (CMDEs) for the Bragg grating are obtained as:

$$\frac{dR}{dz} = i\bar{\sigma}R(z) + i\kappa S(z), \tag{2.5}$$

$$\frac{dS}{dz} = -i\bar{\sigma}S(z) - i\kappa^{*}R(z), \tag{2.6}$$

where $R(z) = A(z)\exp(i\delta z - \phi/2)$ and $S(z) = B(z)\exp(-i\delta z + \phi/2)$, κ is the AC coupling coefficient for the fundamental core mode, which is given as $\kappa = \pi\nu f(z)\overline{\delta n}/\lambda$ for a single-mode Bragg reflection grating and $\bar{\sigma}$ is the general

DC self-coupling coefficient. Using $\delta = \beta - \pi/\Lambda$ as detuning from the phase matching condition ($\beta = \pi/\Lambda$), $\bar{\sigma}$ is defined as

$$\begin{aligned}\bar{\sigma} &= \delta + \sigma - \frac{1}{2}\frac{d\phi}{dz} + i\frac{\alpha}{2} \\ &= 2\pi n_{eff}\left(\frac{1}{\lambda} - \frac{1}{\lambda_B}\right) + \frac{2\pi}{\lambda}\overline{\delta n} - \frac{1}{2}\frac{d\phi}{dz} + i\frac{\alpha}{2}\end{aligned} \tag{2.7}$$

where $\lambda_B = 2n_{eff}\Lambda$, which is the design peak-reflection-wavelength of a week grating having period Λ, and $\sigma = \frac{2\pi}{\lambda}\overline{\delta n}$. n_{eff} is the effective mode index in the fiber. $\frac{1}{2}\frac{d\phi}{dz}$ in Eq. (2.7) describes a chirp in the grating period. If the grating is uniform along the z-direction, then $f(z)$ as well as $\frac{d\phi}{dz}$ both are zero and κ, $\bar{\sigma}$, σ all are constant. This reduces CMDEs into coupled first-order ordinary differential equations with constant coefficients, whose solutions can be found analytically by applying appropriate boundary conditions. For a uniform grating of length L, boundary conditions are depicted in Figure 2.1. Here, amplitude of the forward-propagating wave incident from $z = -\infty$ at the input end of the fiber grating ($z = -L/2$) is considered as $R(-L/2) = 1$. As there cannot be any backward-propagating (reflected) wave for $z \geq L/2$ where no perturbation exists, amplitude of the backward-propagating wave at $z = L/2$ is considered as $S(L/2) = 0$. Applying these conditions, the amplitude reflection

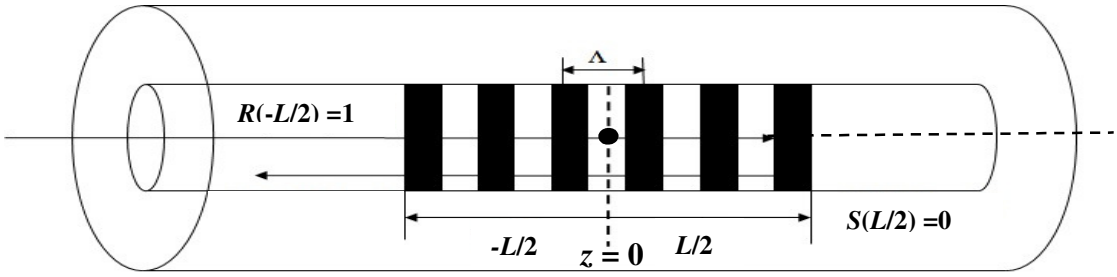

Figure 2.1: Boundary condition for determining amplitude and power reflection coefficients.

coefficient, defined as $\rho = S(-L/2)/R(-L/2)$, comes out to be [123]

$$\rho = \frac{-\kappa \sinh\left(\sqrt{\kappa^2 - \bar{\sigma}^2}\, L\right)}{\bar{\sigma} \sinh\left(\sqrt{\kappa^2 - \bar{\sigma}^2}\, L\right) + i\sqrt{\kappa^2 - \bar{\sigma}^2} \cosh\left(\sqrt{\kappa^2 - \bar{\sigma}^2}\, L\right)} \tag{2.8}$$

The power reflectivity *r*, calculated using $r = |\rho|^2$, comes out to be

$$r = \frac{\sinh^2\left(\sqrt{\kappa^2 - \bar{\sigma}^2}\, L\right)}{\cosh^2\left(\sqrt{\kappa^2 - \bar{\sigma}^2}\, L\right) - \frac{\bar{\sigma}^2}{\kappa^2}} \tag{2.9}$$

Several practical applications of FBG require an adjustment of the optical characteristics of gratings, which is possible only by tailoring the grating parameters along the fiber axis. Such gratings are termed as nonuniform gratings. Some of the examples of nonuniform gratings are apodized gratings, chirped gratings, phase-shifted gratings and superstructure gratings. It's worth mentioning that a simple analytical solution does not exist for the nonuniform gratings, which are characterized by a complicated coupling constant $\kappa(z)$ and chirp $\Lambda(z)$. Several methods have been reported to investigate the reflection and transmission characteristics of such nonuniform gratings. Simplest method among all is the direct numerical integration of CMDEs. However, it is not the fastest method. Another method, known as Rouard's method, works on the principle of treating each grating half-period as a layer in the thin-film stack. Standard thin-film techniques employing matrix for each subwavelength thin-film layer is used to calculate the reflection and the transmission spectra. This method has the capability of simulating the grating characteristics for any refractive index modulation; however, it quickly becomes laborious and

computationally intensive for the gratings having length of few centimeters and 10^5 or more periods.

Most powerful, simple to implement, accurate and generally the fastest method is Transfer matrix method (TMM), which is based on the "piecewise-uniform approach". In this approach, a complex grating of length L is divided into N number of uniform sections. Each section of short length Δz is characterized with constant σ, κ and $\frac{1}{2}\frac{d\phi}{dz}$. It's important to mention that the value of N is restricted by the couple-mode-theory approximations that requires $\Delta z >> \Lambda$, which gives

$$N \approx \frac{2n_{eff}L}{\lambda_B} \tag{2.10}$$

In order to simulate the optical characteristics of these sections, 2×2 matrices (transfer or T-matrices) are established using CMDEs for each uniform section of the grating (Figure 2.2 (a)). These T-matrices represent amplitude and phase response of the particular segmented grating sections. Output of the T-matrix for the first section is used as the input to the second section. This process is continued until a single 2×2 matrix is obtained that describes the optical characteristics of the whole grating. For a single grating section (say 1st) of length Δz, input and output fields are depicted in Figure 2.2 (b). Input fields correspond to the forward propagating wave and are defined as $R(-\Delta z/2)$ and $R(\Delta z/2)$ at the beginning and the end of the section, respectively. Output fields correspond to the backward propagating wave and are defined as $S(-\Delta z/2)$ and $S(\Delta z/2)$ at the beginning and the end of the section, respectively.

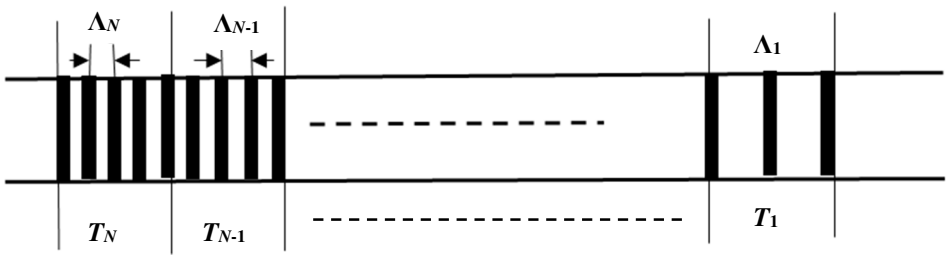

(a)

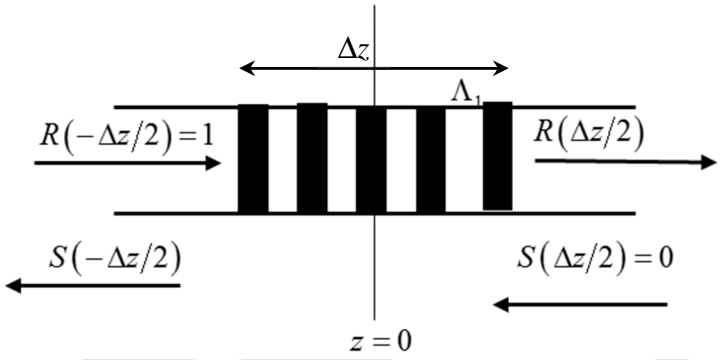

(b)

Figure 2.2: Concept of piece-wise uniform simulation. (a) Segmentation of a non-uniform FBG, (b) Input and output fields across a single grating section.

Employing an appropriate 2 × 2 T-matrix, T^1, fields at the output end (at $\Delta z/2$) of the first section of the grating are transformed into the fields at the input end (at $-\Delta z/2$) of the same section according to the following relation:

$$\begin{bmatrix} R(-\Delta z/2) \\ S(-\Delta z/2) \end{bmatrix} = \begin{bmatrix} T^1 \end{bmatrix} \begin{bmatrix} R(\Delta z/2) \\ S(\Delta z/2) \end{bmatrix} \tag{2.11}$$

For a single grating section of length Δz, boundary conditions are depicted in Figure 2.2 (b). Here, the input field amplitude $R(-\Delta z/2) = 1$ and reflected field amplitude at the output end of the grating $S(\Delta z/2) = 0$. Applying the boundary conditions and explicitly showing the matrix elements for T^1, Eq. (2.11) is rewritten as

$$\begin{bmatrix} 1 \\ S(-\Delta z/2) \end{bmatrix} = \begin{bmatrix} T_{11} & T_{12} \\ T_{21} & T_{22} \end{bmatrix} \begin{bmatrix} R(\Delta z/2) \\ 0 \end{bmatrix}, \tag{2.12}$$

From this matrix equation, the transmitted and reflected amplitudes of the single grating section can be obtained as

$$R(\Delta z/2) = \frac{1}{T_{11}} \ , \tag{2.13}$$

and

$$S(-\Delta z/2) = \frac{T_{21}}{T_{11}} \ , \tag{2.14}$$

Four elements of the transfer matrix T^1 can be calculated by solving the CMDEs. These are given as:

$$T_{11}^1 = T_{22}^{1*} = \cosh(\gamma \Delta z) - i\frac{\overline{\sigma}}{\gamma}\sinh(\gamma \Delta z) \ , \tag{2.15}$$

$$T_{12}^1 = T_{21}^{1*} = -i\frac{\kappa}{\gamma}\sinh(\gamma \Delta z) \tag{2.16}$$

where $\gamma = \sqrt{\kappa^2 - \overline{\sigma}^2}$.

Fields on the LHS of T^1 are the fields on the RHS of the transfer-matrix T^2 of the section "2" and so on. Continuing in this fashion for the entire grating of length L that is divided into N sections, fields at the output end of the grating at $L/2$ and fields at the input end of the grating at $-L/2$ are related as following:

$$\begin{bmatrix} R(-L/2) \\ S(-L/2) \end{bmatrix} = \left[T^N\right]\left[T^{N-1}\right]\cdots\cdots\left[T^2\right]\left[T^1\right]\begin{bmatrix} R(L/2) \\ S(L/2) \end{bmatrix} \tag{2.17}$$

Product of N 2×2 matrices result in a single equivalent 2×2 transfer matrix T for the whole grating:

$$\begin{bmatrix} R(-L/2) \\ S(-L/2) \end{bmatrix} = \prod_{j=1}^{N} \left[T^{j}\right] \begin{bmatrix} R(L/2) \\ S(L/2) \end{bmatrix} = [T] \begin{bmatrix} R(L/2) \\ S(L/2) \end{bmatrix} . \tag{2.18}$$

Applying the appropriate boundary conditions, the amplitude reflection coefficient (ρ) and the amplitude transmission coefficient (t) of the whole grating come out to be

$$\rho = \frac{S(-L/2)}{R(-L/2)} = \frac{T_{21}}{T_{11}} , \tag{2.19}$$

$$t = (1-\rho) = \frac{R(L/2)}{R(-L/2)} = \frac{1}{T_{11}} . \tag{2.20}$$

Phase shifted gratings are one of the important class of the gratings that comprise a phase-step within its length. This phase-step introduces a single narrow pass-band within the transmission spectrum of the grating. The position of this phase-step decides the position of the narrow pass-band. In order to analyze the optical characteristics of such gratings, TMM is again employed. Here, for a phase-step after the i^{th} section, a phase-shift matrix T^{ph} is inserted between the T-matrix for i^{th} and $(i + 1)^{th}$ section in Eq. (2.17). This phase-shift matrix T^{ph} is given as [123]

$$T^{ph} = \begin{bmatrix} e^{-i\phi/2} & 0 \\ 0 & e^{i\phi/2} \end{bmatrix} \tag{2.21}$$

Here, φ is the shift in the phase of the grating itself that results from a change in the n_{eff} or a discontinuity in the grating. This shift in the phase is given as [20]:

$$\frac{\phi}{2} = \frac{2\pi\left(n_{eff} + \delta n\right)}{\lambda} \Delta z_0 \tag{2.22}$$

where Δz_0 is the separation between two grating sections and δn is the local phase change over Δz_0.

2.3 Properties of Uniform Bragg Grating

Some of the important optical characteristics of FBG that play crucial role in optical communication and WDM quasi-distributed sensing applications are peak reflectivity, bandwidth, maximum side-lobe (MSL), side-lobe suppression ratio (SLSR), group delay and dispersion. Some of these characteristics are illustrated in Figure 2.3, which carries the simulated reflection spectrum and the delay of a uniform and weak fiber Bragg grating.

1. **Peak reflectivity**: As can be observed from Eq. (2.9), maximum reflectivity for a Bragg grating occurs at a wavelength at which $\bar{\sigma} = 0$ and is given by

$$r_{\max} = \max\left(|\rho|^2\right) = \tanh^2(\kappa L) = \max\left(\left|\frac{T_{21}}{T_{11}}\right|^2\right) \tag{2.23}$$

Eq. (2.19) is used to evaluate $r_{\max}$ in Eq. (2.23). Peak reflectivity is depicted in Figure 2.3 (a). For a uniform and short grating, $d\phi/dz = 0$ and α can be neglected. Using Eq. (2.7) and the condition $\bar{\sigma} = 0$, it can be shown that this maximum reflectivity (peak of the Bragg reflection) occurs at a wavelength $\lambda_{\max}$, which is given by

$$\lambda_{\max} = \lambda_B\left(1 + \frac{\overline{\delta n}}{n_{eff}}\right) \tag{2.24}$$

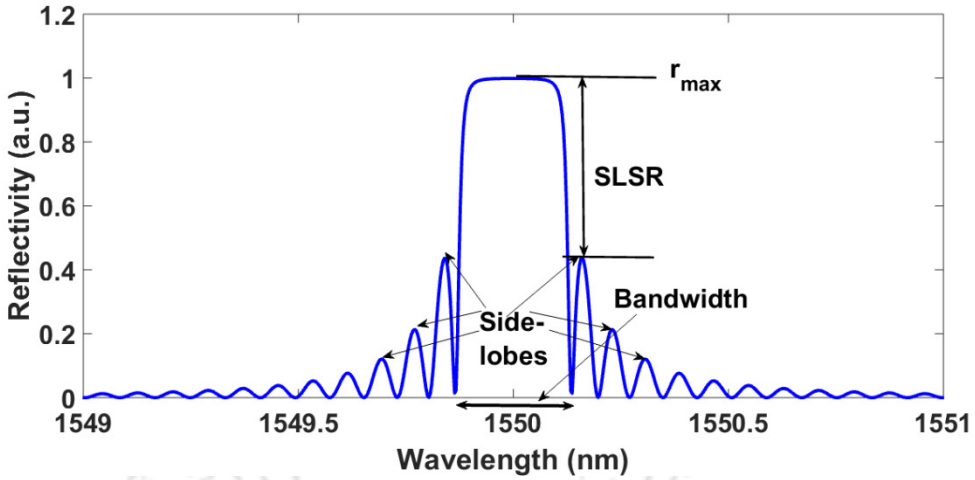

(a)

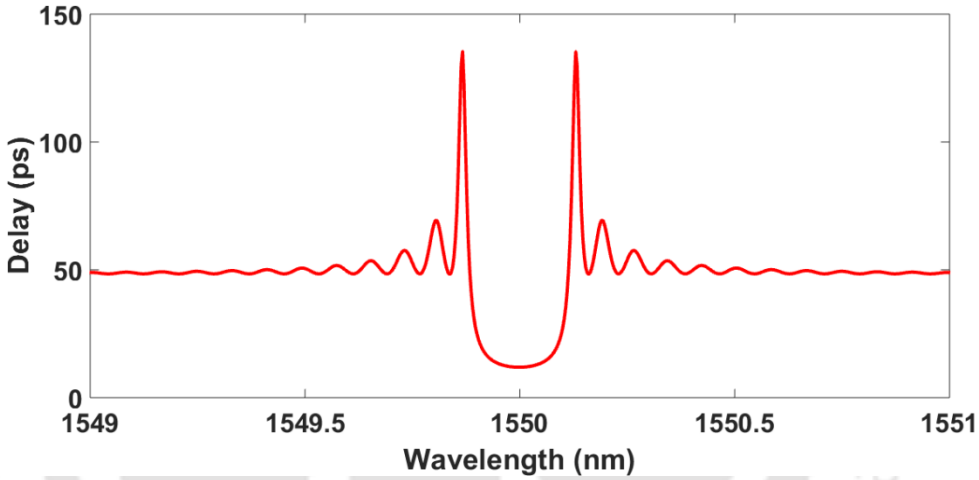

(b)

Figure 2.3: Simulated (a) reflectivity and (b) group delay for a uniform and weak grating with designed wavelength of1550 nm and L = 10 mm.

2. **Bandwidth:** There are several ways to define the bandwidth for a uniform grating. The easiest definition is the bandwidth between the first zeros on either side of the main reflection peak as depicted in Figure 2.3 (a). These first zeros occur when the numerator of Eq. (2.9) goes to zero. This happens for the argument of sinh to be equal to $i\pi$. Using Eq. (2.7) and appropriate conditions, the bandwidth can be determined, which is given as [123]

$$\Delta\lambda = \frac{\nu\overline{\delta n}\lambda}{n_{eff}}\sqrt{1+\left(\frac{\lambda_B}{\nu\overline{\delta n}L}\right)^2} \tag{2.25}$$

3. **Side-lobes:** For a uniform Bragg grating of a finite length, the main peak in the reflection/transmission spectrum is accompanied by a series of side-lobes as depicted in Figure 2.3 (a). Position of the peak reflectivity for these side-lobes can be readily determined from Eq. (2.9) and given as [20]

$$L\sqrt{\kappa^2 - \overline{\sigma}^2} = i\left(p + \frac{1}{2}\right)\pi \tag{2.26}$$

where, p = 1, 2 ,3…… The reason for appearance of these side-lobes is the fact that a uniform grating begins abruptly and ends abruptly at $z = \pm L/2$. These edges of the uniform grating structure act like abrupt interfaces and form Fabry-Perot cavity for the wavelengths that are outside the photonic bandgap of the FBG. The peak reflectivity of various side-lobs, calculated using Eqs. (2.9) and (2.26), is expressed as

$$r_{side-lobe,peak} = \frac{(\kappa L)^2}{(p+1/2)^2 \pi^2 + (\kappa L)^2} \tag{2.27}$$

4. **Time-delay:** The time-delay for the light reflected from the grating is given by

$$\tau_\rho = \frac{d\theta_\rho}{d\omega} = -\frac{\lambda^2}{2\pi c}\frac{d\theta_\rho}{d\lambda} \tag{2.28}$$

where, $\theta_\rho \equiv$ phase (ρ) and c is the speed of light in vacuum. Figure 2.3 (b) shows the typical delay characteristics of the grating whose reflection spectrum is depicted in Figure 2.3 (a).

2.4 Summary

This chapter presents important concepts, principles and techniques to analyze the spectral characteristics of a fiber Bragg grating. Coupled-mode theory and transfer matrix method, the most powerful technique to understand the optical response

characteristics of uniform as well as nonuniform FBGs, are discussed. Some of the key parameters defining the optical characteristics of FBG that play crucial role in optical communication and WDM quasi-distributed sensing applications are highlighted at the end of the chapter.

Chapter 3 : Fiber Bragg Grating Employing Novel Apodization Profile: Performance Optimization for Quasi-Distributed Sensing Applications

The focus of this chapter is to achieve greater efficiency of fiber Bragg grating (FBG) based all-optical quasi-distributed sensing network by suitably tailoring and controlling the key optical characteristics of the FBG. Apodization profile plays a critical role in order to achieve optimum optical characteristics for the FBG. Some of the recently proposed apodization profiles for the FBG and their impact on the sensor characteristics for single as well as multi-point quasi-distributed sensing applications are discussed in section 3.1. A novel apodization profile for achieving optimum optical characteristics for the FBG is proposed in section 3.2. In the context of the proposed apodization profile, grating length and the index-change (the key structural parameters) are optimized in order to achieve the optimum optical characteristics for the FBG. Resulting optical characteristics of the proposed FBG having novel apodization profile and optimized structural parameters are discussed in section 3.3. A comparative analysis of the optical characteristics is also presented in the same section for the proposed FBG and the other selected elite apodization profiles. Section 3.4 describes the application efficiency of the proposed grating in a quasi-distributed sensing network. Finally, summary of the chapter is presented in section 3.5.

3.1 Introduction

Fiber Bragg grating (FBG) offers excellent inherent advantages over the conventional optical fiber sensors (OFS), e. g., low insertion loss, high wavelength selectivity, polarization insensitivity, wavelength encoding nature, ability to be multiplexed and the inherent sensitivity towards strain/temperature perturbations.

Further, being in-fiber device, FBG inherits the remote-sensing capability of optical fiber sensors. Owing to these advantages, FBG is one of the dominant and widely used passive device in communication as well as in the real-field sensing applications. Many such applications, for example, optical add-drop multiplexers (OADMs), optical-cross-connect (OXC), DWDM systems and quasi-distributed sensing system require FBG network/multiplexing. As an example, quasi-distributed sensing systems are the integral part of structural health monitoring that demands simultaneous and multi-point monitoring of various physical parameters of interest. A single string of optical fiber can carry a large array of FBG sensors. These multiplexed FBG sensors may be interrogated by a single light source and detector employing one or a suitable combination of multiplexing techniques such as wavelength-division multiplexing (WDM), time-division multiplexing (TDM), spectral-profile-division multiplexing (SDM) and frequency-division multiplexing (FDM). Among these, WDM based multipoint/quasi-distributed sensing interrogation is the simplest and straightforward technique that exhibits high speed interrogation, better signal-to-noise ratio (SNR) and high measurement accuracy. The WDM interrogation requires FBG sensors in the network, each operating in its own distinct wavelength range, to be designed in such a way that their operational range do not overlap. Further, the number of FBG sensors that can be multiplexed in WDM based quasi-distributed sensing network is mainly dictated by the bandwidth of the light source [86]. High reflectivity, narrow full-width-at-half-maximum (FWHM) and greater degree of side-lobe suppression (SLS) in the spectral characteristics of FBG are desirable and critically important in order to increase the number of FBGs and to devise an efficient and optimized WDM/quasi-distributed sensing network for the given source-bandwidth. Reflectivity, bandwidth and the side-lobes can be controlled by suitably tailoring the FBG employing

appropriate apodization scheme. It's important to mention that, in comparison to the high reflectivity and narrow FWHM, the side-lobe suppression finds the top place on the hierarchical ladder while designing a quasi-distributed sensing network. Recently, few new apodization profiles in [124, 125, 126] have been proposed to optimize optical characteristics of FBG in order to achieve greater efficiency, measurement accuracy and maximum dynamic range for the sensing network. These apodization profiles are very strong. A strong apodization reduces the side-lobes of FBG very efficiently, but at the same time, it truncates the grating length. Truncated grating length results in a reduced reflectivity. From the perspective of achieving a threshold reflectivity, longer grating length is recommended [126]. However, in order to achieve an optimum performance and a high wavelength measurement accuracy in decoding information from the FBG spectrum in a quasi-distributed sensing network, it's not only the high reflectivity that matters, but it's a high signal-to-noise ratio (SNR) that plays a critically important role [86, 124]. To achieve higher SNR, side-lobe suppression ratio (SLSR) needs to be very high. Further, one of the proposed apodization profile in [125] is asymmetrical, which is derived from the Lanczos window. In the case of strong index change, such asymmetrical gratings are characterized with significantly asymmetrical reflection spectra that exhibit several intense side-lobes at the short wavelengths [127]. FBG with asymmetrical reflection spectrum having several intense side-lobes at the shorter wavelength edge is undesirable for quasi-distributed sensing network. Also, SLSR is observed to be less than 30 dB in [125]. Side-lobe suppression should be more than 30 dB for effectively minimizing cross talk between the adjacent channels [128]. All these facts highlight that finding an appropriate symmetrical apodization profile for tailoring FBG that predominantly focuses on to achieve higher degree of side-lobe suppression without

much compromise at the reflectivity and FWHM, thus facilitating high SNR and minimum channel-cross-talk, is quite important while designing an efficient quasi-distributed sensing network.

In this chapter, a novel symmetrical apodization profile is proposed for tailoring FBG. The motivation behind the proposed novel apodization profile is to optimize FBG characteristics in such a way that once deployed in the quasi-distributed sensing network, these novel FBGs would lead to a higher efficiency, measurement accuracy and the dynamic range. Coupled-mode theory (CMT) and Transfer-matrix method (TMM) are used for the theoretical modeling of the proposed FBG. All the simulations are performed in MATLAB. In order to achieve the best optical characteristics of the proposed FBG for quasi-distributed sensing applications, optimum values of the FBG's structural parameters such as grating length (L) and the index-change (δn) are determined. At these optimum grating parameters, reflectivity, FWHM, MSL and the SLSR are observed to be 0.607, 0.14 nm, -35.99 dB and -33.818 dB respectively. A comparative performance analysis of the proposed profile is carried out w.r.t. the other elite apodization profiles [91, 129]. The proposed FBG with optimized characteristics is then employed in a five-stage quasi-distributed temperature and strain sensing network to analyze its application efficiency. Dynamic range for the temperature measurement as high as 131.6℃ and for the strain measurement as high as 1450με are obtained. In order to increase the sensing accuracy towards the applied perturbation (temperature/strain), isolation between the adjacent FBG sensors in a network and the total isolation for individual FBG sensor need to be very high. An isolation of 10.07 dB and the total isolation of 33.818 dB, highest among the other apodization profiles recently reported in the literature, are

observed for the proposed grating. Thus, FBG with the proposed apodization profile is of greater importance for efficient quasi-distributed sensing applications.

3.2 Apodization Profiles

As discussed in Chapter 2, the AC coupling coefficient for the fundamental core mode, κ, varies in accordance with the apodization profile $f(z)$ through the relation $\kappa = \pi v f(z)\overline{\delta n}/\lambda$. Hence, the apodization profile plays critically important role in controlling and suitably optimizing the overall optical performance characteristics of the FBG. A novel symmetrical apodization profile for tailoring FBG with an objective to achieve higher efficiency, measurement accuracy and the dynamic range, once the FBG is deployed in a quasi-distributed sensing network, is proposed and defined as

$$f(z) = J_0\left(\cos\left(\frac{3z}{L}\right)\right)^8\left(\cos\left(\frac{z}{L}-1\right)\right)^4, \quad z\in[0,L] \qquad (3.1)$$

where J_0 is the ordinary Bessel function of first kind of order 0, L is the grating length and z is the distance along the fiber axis. In order to carry out comparative performance analysis of the proposed profile, elite apodization profiles from the literature are selected and simultaneously simulated. These selected elite profiles are:

- Gaussian Profile [91]

$$f(z) = \exp\left(-\frac{4(\ln 2)z^2}{(L/2)^2}\right), z\in[0,L] \qquad (3.2)$$

- Positive Tanh profile [129]

$$f(z) = \begin{cases} \tanh\left[\dfrac{2az}{L}\right], & z\in[0,L/2] \\ \tanh\left[\dfrac{2a(L-z)}{L}\right], & z\in[L/2,L] \end{cases} \qquad (3.3)$$

where a is a real parameter that determines the slope of the Tanh apodization profile at $z = 0$ and, therefore, the degree of apodization. For the positive Tanh apodization profile, a is taken as 4 [129].

These apodization profiles are illustrated in Figure 3.1 for the understanding and comparison. As can be observed from this figure, proposed as well as the selected elite apodization profiles are symmetrical at the center of the grating length and are normalized such that $f(L/2) = 1$. For each of the apodization profile, an apodization parameter, a_{eff}, can be calculated using [129]:

$$a_{eff} = \frac{L_{eff}}{L} = \frac{\int_0^L zf(z)dz}{\int_0^L zdz} \tag{3.4}$$

where L_{eff} is the effective length of the grating with apodization profile. The calculated values of a_{eff} for the proposed apodization profile, the Gaussian profile and the positive Tanh (with $a = 4$) profile come out to be 0.574, 0.522 and 0.826, respectively. A smaller apodization parameter not only results in an enhanced side-

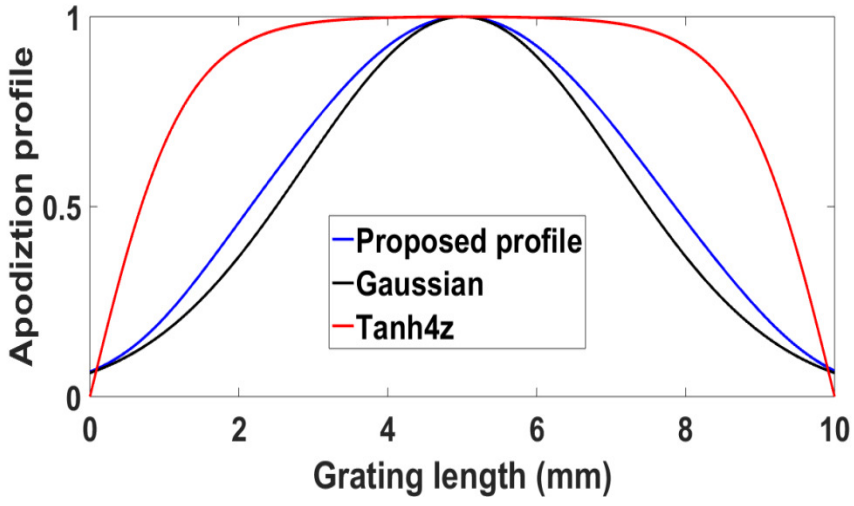

Figure 3.1: Apodization profile vs Grating length.

lobe suppression but leads to a tighter apodization profile and hence, a short effective grating length [129]. Apodization parameter is often used to define the degree of truncation. Reasons behind selecting the Gaussian and the positive Tanh profiles as the elite profiles are the facts that (a) these profiles are predominantly used in grating fabrication, (b) the apodization parameter is observed to be higher than a threshold value of 0.500, hence the effective grating length is not severely compromised, and (c) apodization parameters for these profiles provide upper bound as high as 0.826 (for unapodized grating, a_{eff} = 1.000) and the lower bound as low as 0.522 (within the range of 1.000 – 0.500) that makes the comparative analysis for the proposed apodization profile in quasi-distributed network more effective.

3.3 Results and Discussion

A detailed and comparative performance analysis of FBG that employs proposed apodization profile is carried out in this section. To do so, peak reflectivity, FWHM and side-lobe characteristics of the grating are chosen as the parameters of interest to be investigated. Effect of the grating controlling parameters, e.g., grating length (L), and index change (δn) on the optical characteristics of FBG is rigorously studied. For this, δn is varied in the range of 0.1×10^{-4} (weak grating) – 5.0×10^{-4} (strong grating), whereas L is varied in the range of 2 mm – 20 mm. Design (Bragg) wavelength is fixed at 1550 nm. Optical characteristics of FBG employing the selected elite apodization profiles (depicted in Equations (3.2) and (3.3)) are also simulated to carry out effective comparative analysis. CMT along with TMM is used for the theoretical modelling of the grating structures. All the simulations are performed in MATLAB. Optimum values of the grating structural parameters (L, and δn) are determined in order to achieve the best possible optical characteristics for the proposed FBG that

would lead to an efficient quasi-distributed FBG based sensing network. Optical characteristics of FBG employing the proposed apodization profile and the other selected elite apodization profiles are then simulated at the optimum values of L and δn for the comparative analysis. Finally, the application efficiency of the proposed FBG with optimized characteristics is investigated while deploying it in a five-stage quasi-distributed temperature and strain sensing network.

Reflectivity of FBG plays an important role in quasi-distributed sensing applications as well as in WDM optical communication systems. A high reflectivity not only facilitates better measurement accuracy but also a better signal-to-noise ratio (SNR). In order to investigate the effect of index-change (δn) and to seek a comparatively optimum performance, maximum (peak) reflectivity of FBG employing the proposed as well as selected apodization profiles is plotted as function of δn in Figure 3.2 for a fixed grating length of 10 mm (reason for fixing L at 10 mm is explained in the discussion for Figure 3.3). As can be observed from this figure, peak reflectivity increases rapidly with increasing δn and then saturates for all the opted apodization profiles. Peak reflectivity reaches to the saturation at δn = ~2×10^{-4}

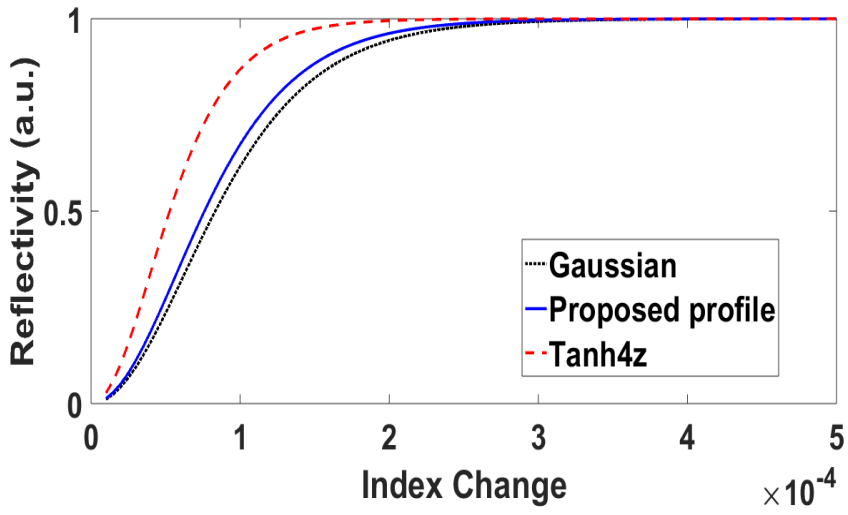

Figure 3.2: Reflectivity vs index change for the fixed L = 10 mm.

for the grating apodized with Tanh profile, and at δn = ~3×10^{-4} for the grating apodized with Gaussian as well as the proposed novel apodization profile. At very low value of δn, grating is very weak (no grating when δn = 0). Increasing δn strengthens the coupling coefficient (κ), and hence, increases the strength of the grating. Increasing strength of grating results in the increasing intensity of the backward propagating light (Eq. (2.23)) until it saturates near 100%. Further, at a fix value of δn, highest peak reflectivity is observed for the Tanh apodized grating among all the three profiles before saturation. However, proposed FBG with novel apodization profile exhibits better reflectivity than the Gaussian apodized grating. This shows that increasing the degree of grating truncation (Tanh → Proposed → Gaussian) results in a successively reduced reflectivity. Results also highlight that in order to achieve same reflectivity, larger δn is required for the tighter apodization profile.

On the other hand, effect of grating length (L) is also investigated in order to seek a comparatively optimum performance. Maximum (peak) reflectivity of FBG employing the proposed as well as selected apodization profiles is plotted as a function of L in Figure 3.3 for a fixed index change of 4×10^{-4}. Reason for choosing higher value of δn is to achieve higher reflectivity as per the observations from Figure 3.2. As can be observed from Figure 3.3, peak reflectivity increases rapidly with increasing L and then saturates for all the opted apodization profiles. This is in accordance with Eq. (2.23). For a fixed κ, reflectivity increases with the grating length until it saturates near 100%. Peak reflectivity reaches to the saturation (~100%) at ~7 mm for the grating apodized with Tanh profile, and at ~10 mm for the grating apodized with Gaussian as well as the proposed novel apodization profile. Once

again, highest peak reflectivity is observed for the Tanh apodized grating among all the three profiles. However, proposed FBG with novel apodization profile exhibits better reflectivity than the Gaussian apodized grating. This shows that the degree of grating truncation not only affects the reflectivity but also the grating length at which reflectivity reaches to saturation.

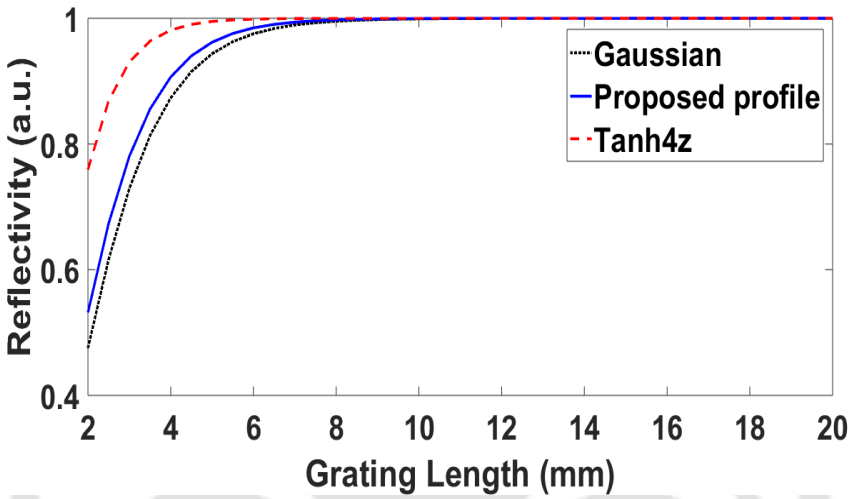

Figure 3.3: Reflectivity vs Grating length for the fixed $\delta n = 4\times10^{-4}$.

FWHM is another crucial parameter, which is important in achieving higher efficiency, measurement accuracy, dynamic range for the measurement and increasing the number of FBGs in a quasi-distributed WDM sensing network. In order to investigate the effect of index-change (δn) and to seek a comparatively optimum performance, FWHM of the FBG spectrum is plotted in Figure 3.4 against δn at a fixed grating length of 10 mm for all the three apodization profiles. As can be observed from this figure, FWHM increases with increasing δn. Tanh profile offers lowest (best) bandwidth only in the range from 0.1×10^{-4} to 0.85×10^{-4}. Gaussian and the proposed novel profile offer almost the same FWHM in the range from 0.85×10^{-4}

to 3.80×10^{-4}. However, proposed apodization profile offers minimum (best) FWHM among all the three profiles for $3.80\times10^{-4} < \delta n < 5.00\times10^{-4}$. In this range, the reflectivity of FBG employing the proposed apodization profile is nearly 100%. It's important to highlight that lowest value of δn should be chosen within the optimum range in order to minimize the broadening of the FBG spectrum. Effect of grating length (L) is also investigated in order to seek a comparatively optimum performance.

FWHM of FBG spectrum employing the proposed as well as selected apodization profiles is plotted as a function of L in Figure 3.5 for a fixed index change of 4×10^{-4}. As can be observed from Figure 3.5, while increasing the grating length, FWHM first decreases nonlinearly and rapidly and then reaches to saturation for all the opted apodization profiles. This shows that at a fixed δn, narrower FWHM can be achieved by increasing the grating length. Further, FWHM of FBG spectrum effectively saturates at around 15 mm for all the three apodization profiles. For this configuration of the grating, $\delta n \times L$ comes out to be 6000 nm, which is very large w.r.t. the design wavelength of the grating (1550 nm) [123]. For such strong grating, light seizes to penetrate the full length of the grating and hence, bandwidth is independent of the

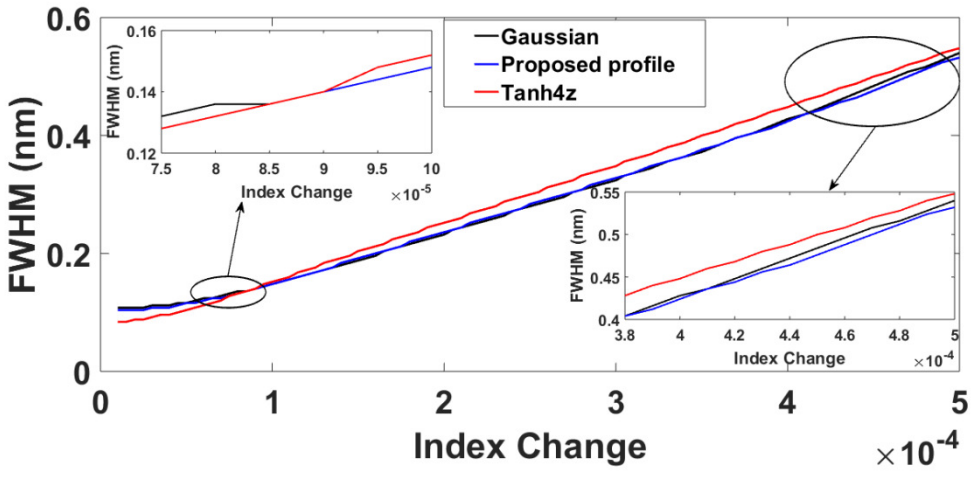

Figure 3.4: FWHM vs index change for the fixed L = 10 mm.

grating length. Before the saturation point, FBG with Tanh profile offers highest bandwidth among all. Gaussian profile offers lowest (best) FWHM for 2.64 mm < L < 8.50 mm, whereas, the proposed apodization profile offers lowest (best) FWHM for 2.07 mm < L < 2.64 mm and then for 9.44 mm < L < 15.00 mm. The range for L (9.44 mm – 15.00 mm) in which the proposed FBG offers best (lowest) FWHM when δn is fixed at 4×10^{-4}, is benefitted with a high reflectivity peak (Figure 3.3). Similarly, the range for δn (3.80×10^{-4} – 5.00×10^{-4}) in which the proposed FBG offers best (lowest) FWHM when L is fixed at 10 mm, is also benefitted with a high reflectivity peak (Figure 3.2). These ranges and combinations are mostly used while inscribing FBGs for almost all practical applications.

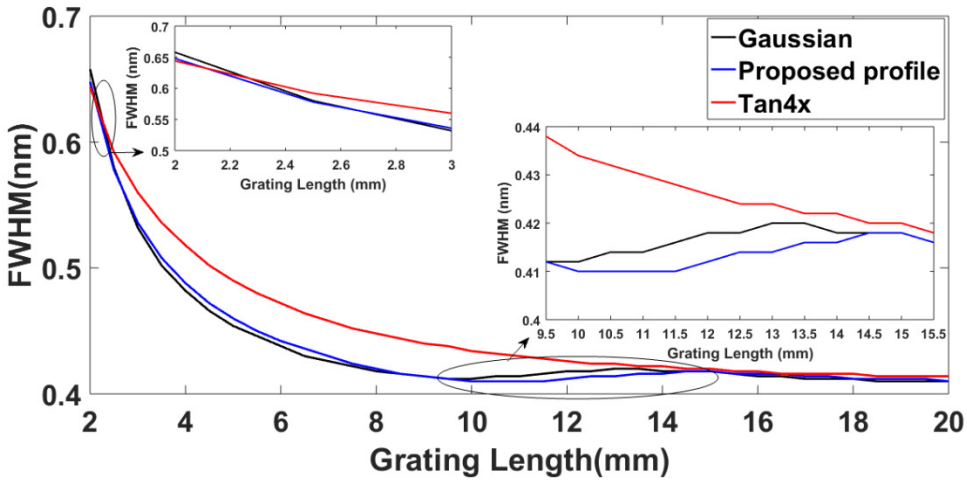

Figure 3.5: FWHM vs Grating length for the fixed $\delta n = 4\times10^{-4}$.

As mentioned earlier, greater degree of side-lobe suppression (SLS) is prominently desirable and hence, decisive in optimizing the grating parameters while devising an efficient, highly accurate quasi-distributed WDM sensing network with high SNR, minimum channel-cross-talk and large dynamic range of measurement. SLS also plays a very critical role in increasing the number of FBGs in the WDM network. Apodization plays a very crucial role in effectively controlling not only the reflectivity and FWHM, but also in controlling side-lobe characteristics of FBG.

Hence, side-lobe analysis is carried out in this part of the discussion. Maximum side-lobe (MSL) and side-lobe suppression ratio (SLSR) are used as the side-lobe parameters for this analysis. Objective of the analysis is to optimize the grating in such a way that leads to the side-lobe suppression of more than 30 dB within the ±1 nm bandwidth centered at the Bragg wavelength [128]. Also, for the better isolation between adjacent channels and reduction of cross-talk in DWDM quasi-distributed sensing systems, MSL must be as low as possible and SLSR must be as high as possible. MSL for FBG employing the proposed as well as selected apodization profiles is plotted as a function of δn in Figure 3.6 for a fixed grating length of 10 mm. As can be observed from Figure 3.6, FBG with Tanh apodization profile is characterized with maximum (not promising) side-lobe strength among all the opted apodization profiles over the entire range of δn. Gaussian apodization profile offers lowest (best) side-lobe strength among all the opted apodization profiles in the range from 0.1×10^{-4} to 0.866×10^{-4} and from 0.904×10^{-4} to 2.495×10^{-4}. However, proposed apodization profile offers lowest (best) side-lobe strength among all the three profiles for $0.866\times10^{-4} < \delta n < 0.904\times10^{-4}$ and $2.4955\times10^{-4} < \delta n < 5.00\times10^{-4}$. At 2.495×10^{-4},

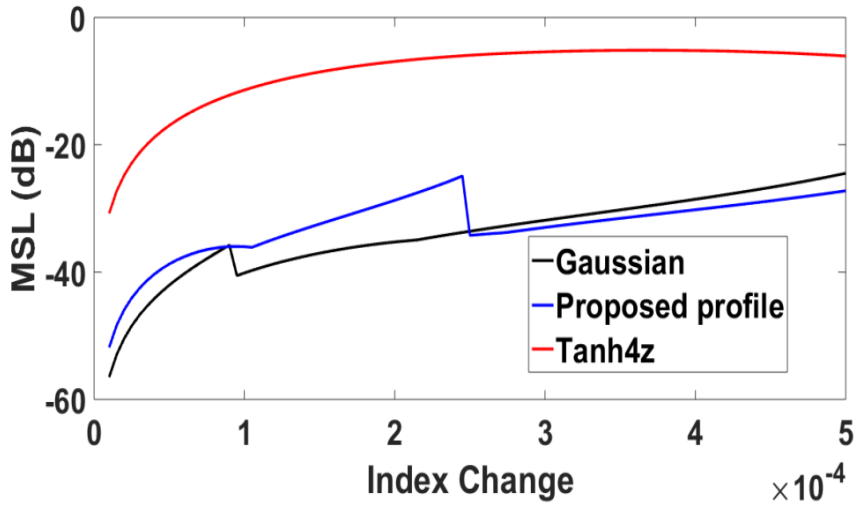

Figure 3.6: MSL vs index change for the fixed L = 10 mm.

MSL for proposed apodization profile reduces by roughly 30 dB in comparison to the Tanh profile.

Figure 3.7 depicts the variation of MSL as a function of L for FBG employing the proposed as well as selected apodization profiles for a fixed index change of 4×10^{-4}. Again, FBG with Tanh apodization profile exhibits maximum (not promising) side-lobe strength among all the opted apodization profiles. Gaussian apodization profile offers lowest (best) side-lobe strength for 4.00 mm < L < 6.44 mm and then for 13.68 mm < L < 16.88 mm. Proposed apodization profile offers lowest (best) side-lobe strength among all the three profiles for 6.44 mm < L < 13.68 mm and then for 16.88 mm < L < 20.00 mm.

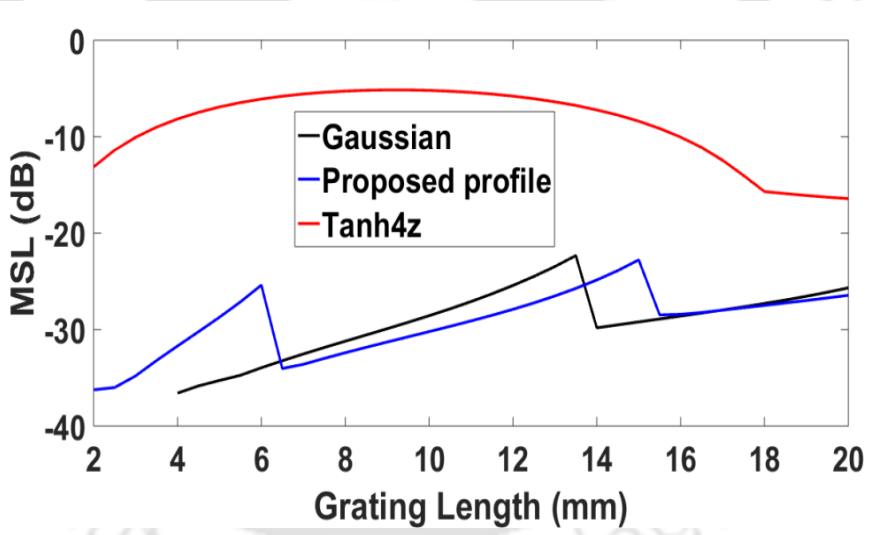

Figure 3.7: MSL vs grating length for the fixed $\delta n = 4\times10^{-4}$.

Side-lobe analysis is further extended to SLSR in order to seek a comparatively optimum performance. Variation of SLSR as a function of δn is plotted in Figure 3.8 at L equals to 10 mm, whereas, variation of SLSR as a function of L is plotted in Figure 3.9 at δn equals to 4×10^{-4}. As can be observed, proposed apodization profile offers highest SLSR among all the three profiles for δn in the range of 0.843×10^{-4} – 0.9095×10^{-4} as well as 2.495×10^{-4} – 5.00×10^{-4}; and for L in the range of 6.44 mm – 13.68 mm as well as 16.88 mm – 20.00 mm. There is a wide range for δn and L, over

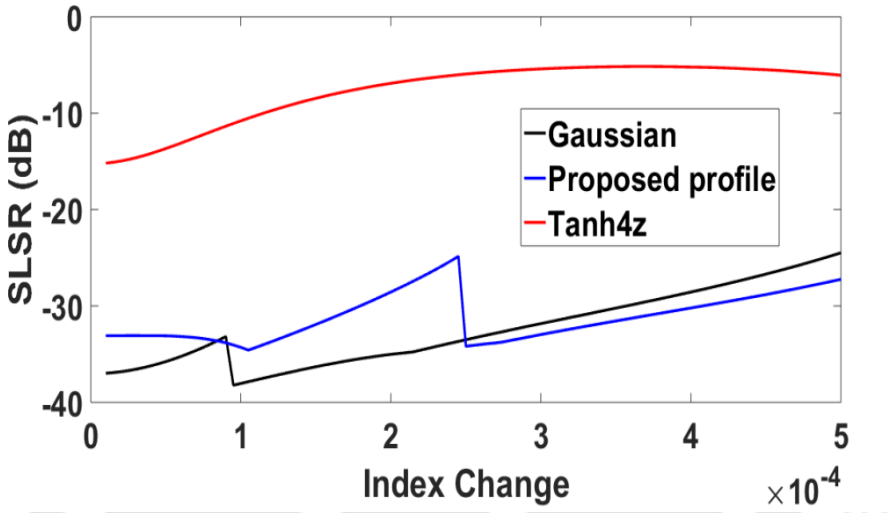

Figure 3.8: SLSR vs index change for the fixed L = 10 mm.

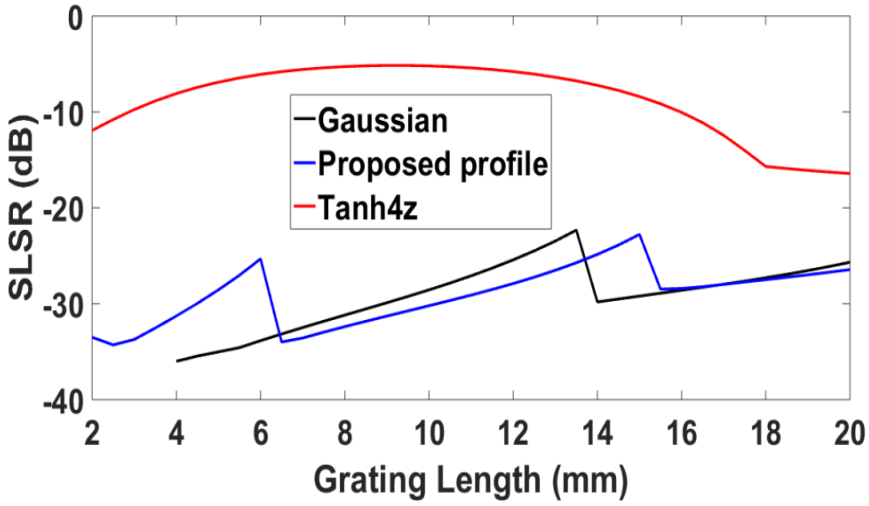

Figure 3.9: SLSR vs grating length for the fixed $\delta n = 4\times10^{-4}$.

which FBG with proposed apodization profile remarkably suppresses the side-lobes with SLSR greater than 30 dB.

The above-mentioned comparative analysis highlights the wide flexibility in designing and tailoring FBG with optical characteristics that can be tuned as per the specific requirement of the application. As stated earlier, while designing and tailoring FBG for realizing an efficient quasi-distributed FBG based sensing network, predominant focus should be on to achieve higher degree of side-lobe suppression, a decisive and highest priority factor, without much compromise at the reflectivity and FWHM. Of course, reflectivity and FWHM also affect performance of the quasi-distributed WDM sensing network. These facts indicate that structural parameters (L and δn) of the FBG should be suitably, smartly and very carefully chosen in order to achieve optimum performance of the WDM sensing network. Addressing all the constraints highlighted here as well as in the beginning of this chapter, criterion (used in this study) for extracting the structural parameters to tailor FBG for quasi-distributed sensing are: (a) reflectivity to be more than or equal to 0.5; (b) FWHM to be less than or equal to 0.20 nm [91]; and the magnitude of MSL and SLSR to be

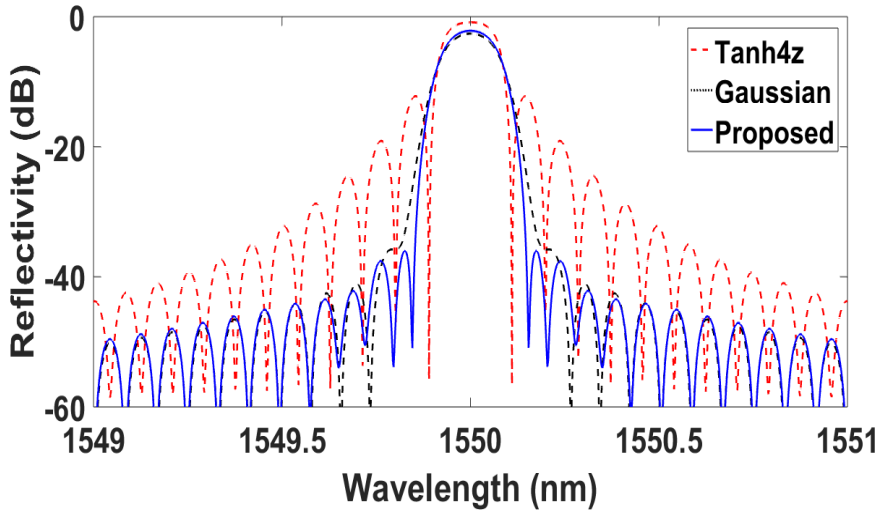

Figure 3.10: Reflectivity spectra of selected apodized FBGs for the optimum parameters of proposed profile L = 10 mm and $\delta n = 0.9\times10^{-4}$.

greater than 30 dB [128]. Values of the grating parameters for which observed characteristics for FBG not only satisfy the above mentioned criterion but are also optimum, are extracted as L = 10 mm and δn = 0.9×10^{-4}. Optical characteristics of FBG employing all the selected apodization profiles are then simulated at these values of the grating parameters. These simulated characteristics are depicted in Figure 3.10. Key performance characteristics for FBG employing proposed as well as the elite apodization profiles are summarized in Table 3.1 for comparative analysis. This analysis is further extended by including another standard apodization profile, the "Sinc profile" [129] as well as some of the recently reported apodization profiles in [125] and [124]. Optical characteristics of FBG employing these additional apodization profiles are also simulated at the above-mentioned values of L and δn. It's worth mentioning that the evaluated optical characteristics for the profile in [124] are excluded from the comparative analysis. Reason is the observed reflectivity of ~0.126 (~12.6%) only, which is too low to be considered in devising an effective quasi-distributed sensing network. As can be observed from Table 3.1, at L = 10 mm and δn = 0.9×10^{-4}, same FWHM is obtained for all the selected profiles, which is within the threshold limit of 0.2 nm for all the selected profiles. Highest reflectivity is obtained for the Tanh profile, which is expected as the degree of grating truncation is lowest for this profile among all the considered profiles. As mentioned earlier, the focus of research in this study is to achieve optimum side-lobe suppression without much compromise at reflectivity and the FWHM. As can be observed from the results

Table 3.1: Optical characteristics of the apodization profiles

Profile	Reflectivity	FWHM (nm)	MSL (dB)	SLSR (dB)
Tanh4z	0.821	0.14	-12.20	-11.345
Gaussian	0.549	0.14	-35.77	-33.165
Sinc	0.626	0.14	-27.16	-25.134
Ali et.al. [125]	0.727	0.14	-25.14	-23.764
Proposed	0.607	0.14	-35.99	-33.818

summarized in Table 3.1, only the Gaussian and the proposed apodization profile yield side-lobe suppression with a magnitude greater than 30 dB. However, the best side-lobe suppression characteristics are obtained for the proposed profile. In addition, a better reflectivity is obtained for the proposed profile in comparison to the Gaussian profile. These observations conclude that the proposed novel apodization profile with L = 10 mm and $\delta n = 0.9\times10^{-4}$ is the ideal choice for achieving greater degree of side-lobe suppression with an acceptable FWHM of 0.14 nm (< 0.2 nm) and an acceptable reflectivity of 0.607 (> 0.5). These features establish that the proposed FBG is most suitable for employing in quasi-distributed WDM sensing systems.

3.4 Quasi-distributed Sensing Application

FBGs with the proposed novel apodization profile, comprising the optimized grating parameters (L = 10 mm and $\delta n = 0.9\times10^{-4}$) are used in this part of the study. Before deploying in the sensing network, response of the proposed grating towards the applied temperature and strain perturbations is analyzed. Equations (1.4) and (1.6) are incorporated in the simulations. Optical fiber parameters, as specified in Chapter 1, are used to simulate temperature and strain response characteristics. Temperature and strain sensing characteristics of the proposed grating are depicted in Figure 3.11 and Figure 3.12 respectively. As expected, peak wavelength (λ_B) increases linearly with increasing temperature/strain perturbations. Temperature sensitivity of 13.32 pm/°C and strain sensitivity of 1.21 pm/με are obtained for the proposed FBG sensor, which are at par with the sensitivities reported for the other apodization profiles used in this study.

With the promising charactersitics as depicted in the previous sections, proposed FBG is employed in a five-stage quasi-distributed temperature and strain sensing

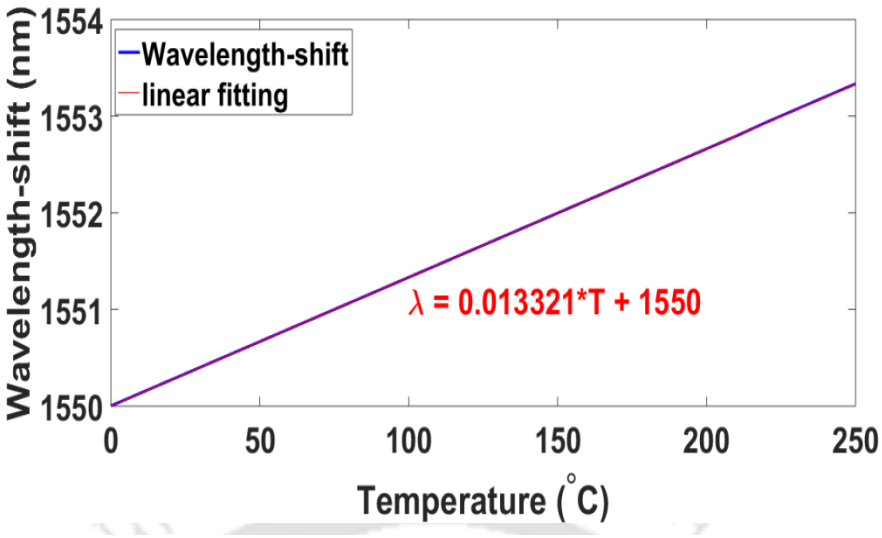

Figure 3.12: Peak wavelength shift of the proposed FBG with applied temperature perturbations.

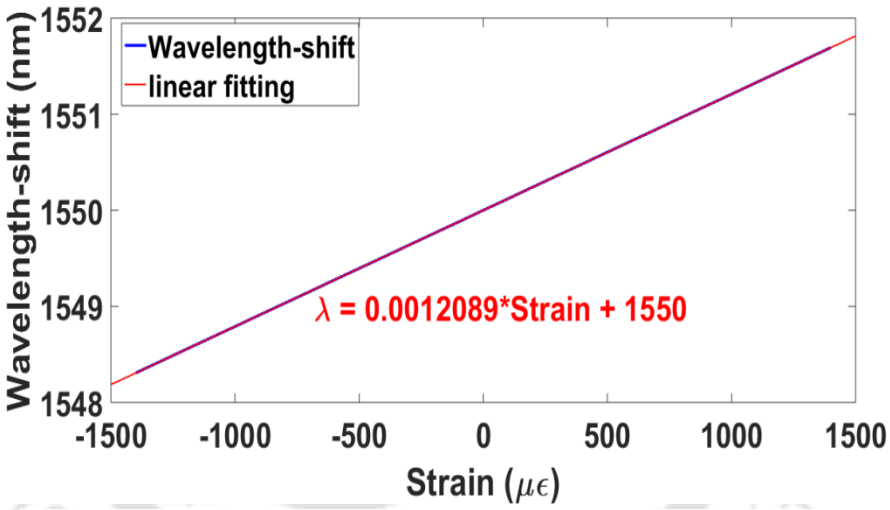

Figure 3.11: Peak wavelength shift of the proposed FBG with applied strain perturbations.

network to analyze its application efficiency. The five-stage quasi-distributed network is constructed employing FBGs with λ_{B1} = 1546.12 nm, λ_{B2} = 1548.12 nm, λ_{B3} = 1550.12 nm, λ_{B4} = 1552.12 nm and λ_{B5} = 1554.12 nm. The spacing between adjacent wavelengths of 2 nm (250 GHz) is chosen as per the ITU-T C-band grid recommendations. Figure 3.13 shows the reflectivity spectrum of these five stages quasi-distributed sensing network without any external perturbation applied to any one of the grating. Now temperature/strain perturbations are applied only to the third

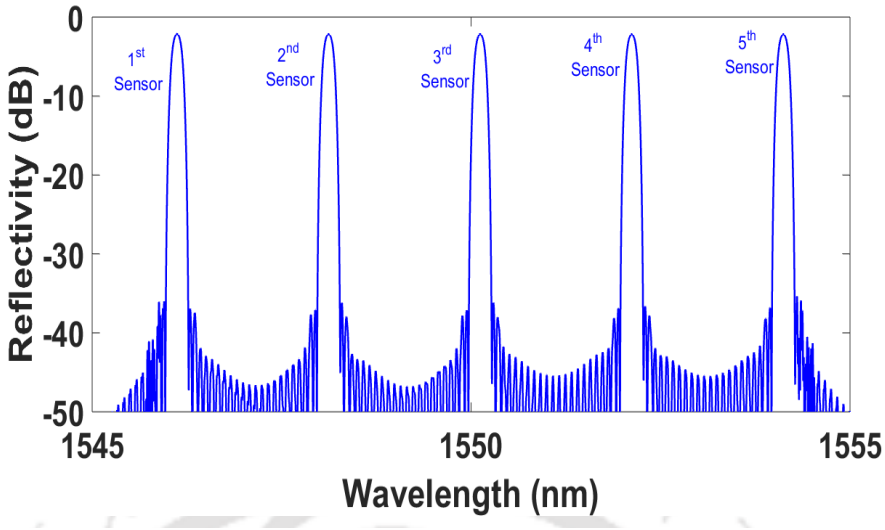

Figure 3.13: Reflectivity spectra of the proposed FBGs (L = 10 mm and $\delta n = 0.9\times10^{-4}$) in a five-stage quasi-distributed sensing network without any external perturbation.

sensor (λ_{B3} = 1550.12 nm) of this network, keeping other FBG sensors free from any external perturbations. Applied temperature/strain perturbations result in the red-shift for λ_{B3}. Maximum permitted red-shift and that ways, maximum applied and still measurable temperature/strain (dynamic range of the measurement) is dictated by the resolution of reflectivity spectra of the adjacent sensors (FBG3 and FBG4 in this case). Hence, the limit of maximum measurable perturbation is dictated by the limit of resolution or the main lobs of FBG3 and FBG4 in this case. Rayleigh's criterion for the two peaks to be "just resolved" is used in the present study. In the absence of side-lobes, Rayleigh's criterion leads to a maximum permissible red shift for a given FBG to be equal to the difference of wavelength-spacing between the two successive gratings and the FWHM. However, in the presence of side-lobes (even though very weak), it's quite important to include a "Guard band" in order to prevent any possibility of interference/modulation of the information and to achieve higher accuracy in decoding information from the FBG spectrum. Inclusion of "Guard band" truncates the maximum possible red-shift and hence the dynamic range. It is for this reason, FBG that facilitates the lowest "Guard band" will always be preferable. Figure

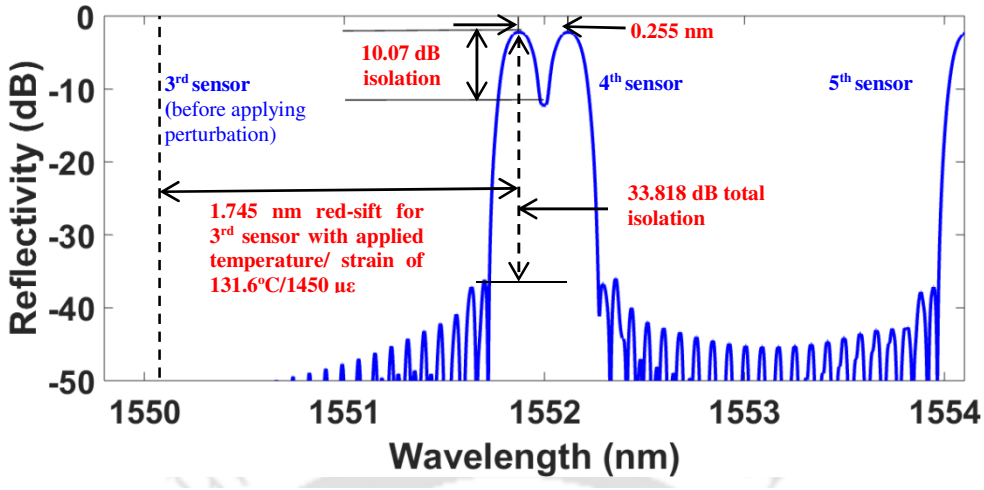

Figure 3.14: Response of the quasi-distributed sensing network employing FBG with the proposed apodization profile having L = 10 mm and $\delta n = 0.9\times10^{-4}$. Applied temperature/strain to only the third sensor is 131.6 °C/1450 με.

3.14 illustrates the resulting reflectivity spectrum of the quasi-distributed sensing network when the temperature/strain perturbations are applied to FBG3. A guard band as low as 0.115 nm is observed to be sufficient in order to maintain highest possible accuracy without any mixing of the information. With a guard band of 0.115 nm and the FWHM of 0.14 nm, maximum red shift for any FBG sensor is observed to be 1.745 nm. For this wavelength shift, maximum applied temperature and strain that can be accurately measured are obtained as 131.6°C and 1450με respectively, as depicted in Figure 3.14. Isolation (combined-peak to saddle-point) for 3rd and 4th FBG sensors under the "Rayleigh's criterion" is observed to be 10.07 dB; whereas the total isolation is observed to be 33.818 dB. For the apodized grating with optimum characteristics proposed in [126], guard band as large as 0.2592 nm is required to prevent the cross talk between the adjacent sensors. The isolation between the two adjacent sensors and the total isolation are observed to be 4.83 dB and 91 dB, respectively. Similarly, for the apodized grating with optimum characteristics proposed in [125]; the isolation and the total isolation are observed to be 6.953 dB and 25.30 dB, respectively. Further, the response characteristics of the five-stage quasi-

distributed temperature/strain sensing system is also simulated for FBGs employing Tanh and Sinc profiles at the optimum structural parameters (L = 10 mm and δn = 0.9×10^{-4}). As an example, total isolation for the Tanh and the Sinc profiles at the optimum guard band are observed to be 11.345 dB and 25.134 dB, respectively. This shows that the highest isolation and the total isolation are achieved for the proposed apodization profile among all the other considered in this study. An efficient apodization process leads to a high channel isolation, which increases the performance efficiency of FBG based quasi-distributed sensing system. High isolation ensures that the reflectivity peaks of the two adjacent FBGs are well resolved and highly distinguishable even after the maximum translation of the spectrum of one FBG towards the other under the influence of the applied external perturbations. Importantly, high isolation greatly minimizes the inter-channel cross talk, and hence, interference/modulation of the coded information onto the FBG spectrum in the FBG based WDM network. Further, the dynamic range of measurement is observed to be in the range of ~121°C – 127°C and ~1350με – 1400με for the FBG employing the elite apodization profiles. Analyzing the performance characteristics and the application efficiency in a quasi-distributed sensing network, narrow FWHM, superior side-lobes suppression capability, highest channel isolation in a multiplexed network, highest total isolation and the largest dynamic range of measurement are the distinguished features of the proposed FBG. These features make the proposed FBG most suitable for devising an efficient and optimized DWDM/quasi-distributed sensing network for a given source-bandwidth.

3.5 Summary

In this chapter, a novel apodization profile is proposed for tailoring and controlling key optical characteristics of FBG for its efficient application in a quasi-distributed sensing network. Objective of designing FBG for quasi-distributed sensing is to achieve better efficiency, measurement accuracy, high SNR, minimum channel-cross-talk and a large dynamic range. Optical characteristics, e.g., reflectivity, FWHM and the side-lobe suppression which are critically important for WDM sensing applications are optimized. While doing so, predominant focus is to achieve greater degree of side-lobe suppression without much compromise with reflectivity and FWHM. A rigorous and comparative analysis is carried out for the FBG employing proposed as well as the elite and the recently reported apodization profiles. Among all the apodization profiles included in the theoretical analysis, best side-lobe suppression characteristics along with a FWHM of 0.14 nm (< 0.2 nm) and reflectivity of 0.607 (> 0.5) are observed for the proposed apodization profile with L = 10 mm and δn = 0.9×10^{-4}. These features establish that the proposed FBG is most suitable for quasi-distributed sensing applications. The proposed FBG with optimized characteristics is then employed in a five-stage quasi-distributed temperature and strain sensing network to analyze its application efficiency. An isolation of 10.07 dB and the total isolation of 33.818 dB, highest among the other apodization profiles studied in this research, are observed for the proposed grating. Further, a large dynamic range for the temperature/strain measurement up to 131.6°C/1450με is achieved. These facts establish that the FBG with proposed apodization profile is of greater importance as it is most suitable for efficient quasi-distributed sensing applications.

Chapter 4 : Study of Slow-Light in π-Phase-Shifted FBG and its Application in WDM-Quasi-Distributed Sensing Network

Slow-light FBG sensors are known for high sensitivity and better resolution as compared to the conventional FBG sensors. In this chapter, slow-light in π-phase-shifted fiber Bragg grating (π-FBG) and its applications for single and multipoint/quasi-distributed sensing are theoretically analyzed. Section 4.1 presents general introduction and a review of slow-light FBG sensors for the detection of deferent physical parameters of interest. The concept of slow-light in π-FBG and its sensing characteristics are presented in section 4.2. Optical characteristics of slow-light π-FBG are optimized with respect to the grating parameters, such as grating length (L), index change (δn), loss coefficient (α) and the apodization profile. Numerical results for the optimized slow-light π-FBG and its sensing characteristics are discussed in section 4.3. Section 4.4 describes the application efficiency of the proposed slow-light π-FBG in a quasi-distributed sensing network. Finally, the summary of the chapter is presented in section 4.5.

4.1 Introduction

During past two decades, one of the areas that has generated lots of research interest is to achieve an active control on the velocity of the optical signal in material systems, which finds enormous applications in optical fiber communication systems, optical processing, quantum computing as well as in all-optical sensing. There are two possibilities – light being "slow" under the circumstances when group velocity is much smaller than the phase velocity of light and, light being "fast" under the

circumstances when group velocity exceeds the phase velocity of light in a dispersive medium. In particular, optical fiber based slow light technology is of great research interest as it has widespread applications, especially in optical fiber sensing. The increase in the delay time that leads to the slow light technology, improves the sensitivity and the resolution manifold. One way to achieve it is by exploiting the intrinsic optical properties of the fiber material, which is termed as *material slow-light* (discussed in Chapter 1). Other way to achieve it is by exploiting periodic structured optical material within the fiber where the propagation of the optical pulse is significantly controlled by the spatial modulation of the optical properties of the fiber material. This is termed as *structural slow-light*. Example of structures that are used to manipulate the group velocity of the propagating optical pulse are circled coupled resonator optical waveguides (CCROW), photonic crystal fiber and fiber-Bragg gratings (FBG). Material slow light cannot be exploited for sensing some of the key parameters required to be monitored in structural health monitoring, e.g., strain, rotation, torsion, tilt, micro displacement etc. [130]. Further, in comparison to the *material slow-light*, realization of *structural slow-light* is not only quite simple but leads to a genuine field enhancement [63] and can be used for sensing various parameters of interest. Among various structures, slow light in FBG has gained extensive research interest owing to its advantages of being a simple structure of small size, easy integration, relying on a passive resonant effect and an exceptional capability of controlling the slow light mechanism. It's important to mention that FBG acts as a narrowband reflection filter centered at the Bragg wavelength (λ_B). Acting as a notch filter, it must strongly reflect frequencies within the bandwidth of FBG's reflection peak (bandgap in transmission) and transmit all frequencies outside the peak. Strong reflection (high reflectivity) can be achieved, as an example, by

increasing the index modulation (δn) as large as possible (greater than ~ 0.001) and maintaining the loss coefficient (α) as low as possible. As explained in Chapter 2, this leads to the formation of pronounced narrow side-lobe resonances on both the sides of reflection peak (Figure 2.3) in the case of uniform FBG. In the vicinity of one of these resonances, light travels back and forth multiple times along the grating before making an exit from either side of the grating. This way, it experiences a longer group delay (equivalently, large effective group index n_g and large apparent group velocity reduction) than light away from the resonance. A simple analogy can be drawn from the Fabry-Perot interferometer (FPI), which comprises two reflectors. FBG can be considered as a superposition of FPIs with distinguished pair of reflectors distributed across its length (consequence of a periodic structure). Thus, strong uniform FBG supports *structural slow-light* and these resonances are referred to as the slow light resonances. These narrow resonances (and hence, large group indices) are exploited in developing sensor with extraordinary sensitivity. In the *structural slow-light* based sensing mechanism, phase shift induced by the applied perturbation to the structure is inversely proportional to the group velocity. As the group velocity is reduced substantially, this phase shift increases manifold resulting in a greatly enhanced sensitivity. These side-lobe resonances exist in conventional uniform/apodized FBGs (FBGs with weak index modulation) too. However, such gratings are so weak that the offered group index n_g is barely larger than n_{eff}. As an example, n_g of 3.3 (as against n_{eff} of ~1.44 in conventional single-mode optical fiber) was observed at around 1550 nm for FBG with L = 2.67 cm and $\delta n = 1.0\times10^{-4}$ [83]. Hence, slow-light mechanism is not observed in conventional FBGs. The standard way to classify FBG as a "slow-light FBG" is to have at least one resonance that exhibits n_g many times (>>~10) larger than n_{eff} [131]. Further, n_g increases rapidly with δn; and for a fixed δn, n_g

increases with L. Also, internal loss (α) not only reduces the transmission of FBG but also limits the maximum achievable n_g. Thus, α must be as low as possible. Hence, slow-light can be induced in FBG with an optimum value of δn, L and α. In general, δn for slow-light FBG used to be 10 to 30 times stronger than the δn for conventional FBG.

Apart from strong and uniform FBG, light can be further slowed down in a strong FBG with an appropriate apodization. In a strong and apodized FBG, side-lobes at the longer wavelength region around the bandgap are greatly reduced. Whereas, sharp side-lobe resonances (multiple slow-light peaks) are observed at the shorter wavelength region around the bandgap, leading to a much larger group delay/index (equivalently, much lower group velocities). As an example, n_g as high as ~212 was observed around 1550 nm for apodized FBG with L = 1.65 mm, α = 3.7 m^{-1} and δn = 4.5×10^{-3}. Interestingly, an un-apodized FBG with the same value of L, α and δn is characterized with a much lower n_g of 70.2 only [83]. The distinct advantages of strong apodized FBG over the strong uniform FBG are: (a) strong uniform FBG is characterized with higher apparent internal loss and, (b) resonances in strong apodized FBG have a much higher interference quality factor Q than in a uniform FBG.

It's important to mention that the strain and temperature sensitivities of conventional FBGs are limited. As an example, typical strain and temperature sensitivity of the conventional FBG written in germanosilicate optical fiber are of the order of 1.2pm/με and 13.7pm/^{o}C respectively. In order to characterize conventional FBG sensors, the wavelength shift resulting from the applied perturbation is measured either by an optical spectrum analyzer or an imbalanced Mach-Zehnder interferometer (MZI). Using the latter scheme, a better strain response manifested by the minimum

strain sensitivity of 0.6nε/√Hz was achieved [132]. There have been attempts to increase the sensitivity of FBG by employing various other configurations. Over the past couple of years, exploitation of the slow-light mechanism for increasing the sensitivity of the FBG sensor has attracted considerable amount of research interest. In one of such slow-light based attempts, edge of the reflection peak of an FBG is interrogated with narrow-linewidth laser [133]. In another attempt, FBG is interrogated at the steepest slope of one of the multiple slow-light resonances (peaks) on the shorter wavelength region of the bandgap [14]. Observed sensitivity in such schemes can be remarkably high because the slope of the transmission resonances at shorter wavelength region of the bandgap is very steep, giving rise to a large n_g. However, merely achieving maximum n_g does not guarantee the maximum sensitivity. This is because the maximum achievable sensitivity of slow-light based sensors towards the applied perturbations (e.g., temperature and strain) is proportional to the product $n_g T_0 L$, where T_0 is the peak transmission of the resonance [14]. In order to achieve maximum sensitivity, it's the product $n_g T_0 L$ that needs to be optimized. Resonance closest to the edge of the bandgap is characterized with highest n_g but its power transmission is used to be too weak. Hence, maximum sensitivity may not be observed while interrogating the first slow-light resonance. As an example, maximum sensitivity is observed at the second slow-light peak for an apodized FBG (L = 1.2 cm, α = 1.0 m^{-1}, δn = 1.0×10^{-3} and FWHM = 0.98 cm), which was characterized with maximum n_g equal to 127 [83]. Importantly, the requirement of large δn for realizing ultra-sensitive slow-light sensor generally results in an increased loss. Thus, δn and the loss should be controlled in such a way that leads to the maximum value of the product $n_g T_0 L$. Further, the sensitivity enhancement is achieved by exploiting the slow-light mechanism at the cost of reduced bandwidth. This is because of the fact

that slow-light exists only over a limited range of frequencies. As the group delay increases, this range of frequencies becomes further narrower.

Employing strong apodized slow-light FBG, the dynamic strain sensitivity is observed to be 0.314 $(\mu\varepsilon)^{-1}$ in [83]. Researchers in [134] exploited slow-light phenomenon employing strong apodized FBG that was fabricated using ultrafast pulses at 403 nm. This strong apodized FBG was characterized with considerably lower propagation loss (α was ~ 0.1 m^{-1} in comparison to usual 1.1–1.5 m^{-1} for the UV written FBGs). Transmission peak closest to the band edge was characterized with n_g of 58.2. Observed maximum strain and temperature sensitivities were 2.15 $(\mu\varepsilon)^{-1}$ and 22.1 $^oC^{-1}$ respectively. In [135], researchers exploited 25 mm long strongly apodized FBG. In order to achieve large δn and low α, FBG was fabricated using femtosecond laser (806 nm) in a deuterium-loaded optical fiber. The observed maximum strain sensitivity was ~4.0 $(\mu\varepsilon)^{-1}$ with a remarkable strain resolution of 30 fε/√Hz at 30 kHz. As another example, a micro displacement sensor that exploits the strain sensitivity of slow-light (uniform) FBG was experimentally demonstrated in [136]. Results show that in comparison to the normal FBG, 13 times higher sensitivity and resolution are observed for the slow light FBG. The dynamic displacement range of the proposed system is limited to 0.06 mm. Arora *et al.* experimentally demonstrated a slow-light FBG based temperature sensor that employed 6.5 mm grating fabricated using femtosecond laser. The temperature resolution of 0.3 m°C /√Hz was observed, which is nearly 30 times lower than the resolution achieved by conventional FBG [137]. However, the theoretically calculated temperature sensitivity for this sensor is predicted to be very low at ~5.2 $°C^{-1}$. Even with the substantial improvement of the resolution in this case, the internal loss was of the order of ~1.14 m^{-1}. In order of offset the internal loss of the slow-light FBG, Vigneron *et al.*

employed 6.5 mm slow-light apodized FBG written in Er-doped optical fiber using femtosecond laser [138]. This FBG was pumped at 1475 nm. At the highest pump power of 32.6 mW, used in this study, the narrowest resonance was observed with a FWHM of 8.5 fs, transmission of 95% and a record n_g of 13,900. The theoretically calculated strain sensitivity for this sensor is predicted to be very high at 147.5 $(\mu\varepsilon)^{-1}$.

Light can also be slowed down by employing phase-shifted FBG. When a discrete π phase-shift discontinuity is inserted into the middle of the FBG, the resulting structure is termed as π-phase-shifted FBG or π-FBG. The unique characteristic feature of π-FBG is the appearance of a single ultra-narrow transmission peak/pass band (strong resonance) within the band gap (stop band) of the FBG with nearly 100% reflectivity and much steeper slope than that of the side-lobe resonances of a strong uniform/apodized FBG. Light at these resonance frequencies undergoes strong localization centered on the phase shift, which allows to achieve very small sensing length. Importantly, the resonance frequencies exhibit slow-light effect arising from the significantly higher group delay. Further, the FWHM of the narrow pass band depends on the index modulation δn. Increasing δn (strong grating) decreases the FWHM of the pass band. In the case of π-FBG, apodization not only reduces the side lobe strengths outside the stop band but also affects the FWHM of the narrow pass band. Stronger apodization leads to a larger FWHM [20]. However, lowest FWHM of this pass band is desirable for multipoint/quasi-distributed sensing applications. If π-FBG is exploited for the sensing applications, much steeper slope of its single pass band will result in an extraordinary enhancement of the sensitivity. Interestingly, no side-lobes exist around this passband and hence, demodulation of the information about the applied perturbations is easier. However, the dynamic range of π-FBG is limited owing to the finite bandwidth of the stop band of the FBG.

Researchers in [139] exploited the steep edge of the transmission peak that exists inside the bandgap of π-FBG. Observed minimum strain sensitivity was 5pε/√Hz for frequencies greater than 100 kHz. Researchers in [140] proposed interferometric interrogation scheme for π-FBG and predicted a minimum strain sensitivity of ~4pε/√Hz. It's important to mention that the quasi-distributed sensing application of the π-FBG is not yet explored to the best of the author's knowledge.

This chapter presents detailed theoretical study of the optical (transmissivity and delay) and sensing characteristics of slow-light π-FBG. The main objective of the research carried out in this chapter is to develop slow-light π-FBG based all-optical quasi-distributed sensing network; and to analyze the response characteristics as well as the efficiency of this novel sensing network by suitably optimizing the key optical characteristics of the π-FBG. In the first step to achieve the objective, optical characteristics of slow-light π-FBG are optimized with respect to the grating parameters (δn, L, α and the apodization profile). In addition to the merits over the other apodization profiles analyzed in Chapter 3, proposed apodization profile depicted by Eq. (3.1) also qualifies the requirement (highlighted in the preceding discussion of this chapter) of achieving narrower FWHM of the characteristic pass band of π-FBG. Hence, apodization profile proposed in Chapter 3 is employed for π-FBG. The optimum grating parameters for which the slow-light π-FBG shows maximum transmissivity and delay are obtained as L = 50 mm, δn = 1.5×10^{-4}, and α = 0.10 m^{-1}. At these grating parameters, peak transmissivity of 0.424 and maximum delay of 31.95 ns are observed. Afterwards, strain and temperature characteristics of the optimized slow-light π-FBG are investigated. Strain sensitivity as high as 8.380 $(\mu\varepsilon)^{-1}$ and temperature sensitivity as high as 91.064°C^{-1} are achieved for the proposed

slow-light π-FBG. In comparison to the reported highest strain and temperature sensitivities (4.0 $(\mu\varepsilon)^{-1}$ [135] and 22.1°C^{-1} [134] respectively), strain sensitivity enhancement of more than two-fold and temperature sensitivity enhancement of more than four-fold are achieved by the proposed slow-light π-FBG. Further, the FWHM of the characteristic's transmission peak (pass band) of the proposed slow-light π-FBG is observed to be 0.0798 pm as against the overall FWHM of 0.2245 nm for its stop band. Finally, the slow-light π-FBG with optimized optical and sensing characteristics is employed in a five-stage quasi-distributed strain and temperature sensing network to analyze its application efficiency. Dynamic range for the strain measurement as high as 1469με and for the temperature measurement as high as 133°C are obtained.

4.2 Numerical Model of the Slow-Light π-FBG

4.2.1 Concept of Slow-light

An ideal monochromatic light wave propagates in a medium with the phase velocity $v_p = \omega_0/k = c/n$; where c is the speed of light in vacuum, ω_0 is the angular frequency of monochromatic light, k is the wavenumber, and n is the refractive index of the medium. However, it's impossible to have a perfect monochromatic light source. A practical light source gives rise to a band of frequencies (termed as the source bandwidth $\Delta\omega$) around the central frequency ω_0. A good quality source is characterized with an ultra-narrow spectral bandwidth (a very high spectral purity). As a consequence of this, light emanated by a source is composed of large number of component sinusoidal waves having slightly different frequencies. While travelling in a non-dispersive medium (perfect vacuum) in which phase velocities of individual components are equal, interference of these component waves gives rise to the formation of wave packet (light pulse) that travels in the medium without any

distortion. However, in a dispersive medium ($n = n(\omega)$) each monochromatic components travels at its own phase velocity, which is slightly different from the other. Interference of the individual components gives rise to the pulse that gets distorted (pulse broadening) while advancing in the medium. For the pulse whose bandwidth is significantly smaller than the normal dispersion regime and for sufficiently short propagation distances (as in the case of FBG for an example), pulse distortion is not too severe. In such conditions, pulse propagation is described by the group velocity, which is given by

$$v_g = \left.\frac{d\omega}{dk}\right|_{\omega_0} = \frac{c}{n_g} \tag{4.1}$$

where n_g denotes the group-index of the medium, and is given by

$$n_g = n + \omega \left.\frac{dn}{d\omega}\right|_{\omega_0} \tag{4.2}$$

The term $dn/d\omega$ at ω_0 describes the dispersive contribution to the group index. In a non-dispersive medium ($dn/d\omega = 0$), group velocity is equal to the phase velocity. However, in a medium, which is characterized with large normal dispersion ($dn/d\omega \neq 0$), n_g is significantly large. This leads to a much smaller group velocity and, hence the slow-light.

As discussed in the introduction section, light can also be slowed down by exploiting periodic structured optical material within the optical fiber. One of the simplest ways to achieve slow-light is by employing FBG, which is characterized by its stop band (centered at the Bragg wavelength) in the transmission. Owing to the inherent advantages, especially in multi-point/quasi-distributed sensing, it is desirable

to create a discrete localized phase-shift in an otherwise uniform periodic structure. In the simplest form, it is achieved by introducing a discrete phase-step of $\lambda/4$ (equivalently, a phase-step of $\pi/2$) at the center of uniform FBG as shown in Figure 4.1. Introduction of this discrete phase-step results in a single ultra-narrow transmission peak (strong resonance), having Lorentzian line shape, within the band gap (stop band) of the FBG. Such FBG structure can be easily visualized as a Fabry-Perot cavity formed by two identical FBGs having cavity length of $\lambda_B/4$ and the length of each grating section equal to $L/2$, where L is the total length of the grating. Light trapped within the cavity accumulates π-phase shift per round trip. This is the reason, such structures are termed as π-phase-shifted FBG or simply, π-FBG. Light at the resonance frequencies undergoes strong localization, which results in the slow-light. A convenient parameter that describes the slow-light mechanism is slowing down factor (SDF), which is defined as the ratio of average group velocity to group velocity of light in the medium [141].

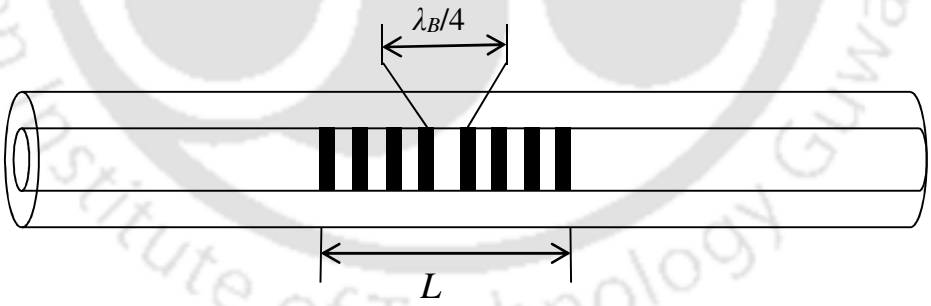

Figure 4.1: Schematic of π-FBG.

The modelling of slow-light π-FBG can be easily performed by employing coupled-mode theory and transfer matrix method as discussed in Chapter 2. Figure 4.2 shows the reflectivity spectra and slowing down factor of an apodized π-phase-shift FBG and a zero phase-shift (apodized & uniform) FBG (AFBG). These gratings are considered in a Germania doped silica optical fiber with the grating parameters L = 50

mm, δn = 1.5×10^{-4}, λ_B = 1550 nm and n_{eff} = 1.464. Apodization profile proposed in Chapter 3 (Eq. (3.1)) is employed for slow-light π-FBG as well as AFBG. For slow-light π-FBG, loss coefficient α is taken as 0.10 m^{-1}. As can be observed, introducing a phase-step of $\lambda/4$ at the center of the FBG not only opens a single ultra-narrow transmission resonance at the center of the reflection spectra but also increases its bandwidth. Further, a very large slow-down effect is observed in the case of π-FBG. This is depicted from the fact that a maximum slow down factor (lowest minimum group velocity) of 317.84 is observed for the (apodized) π-FBG in comparison to a slow down factor of only 1.609 for the conventional (apodized) FBG.

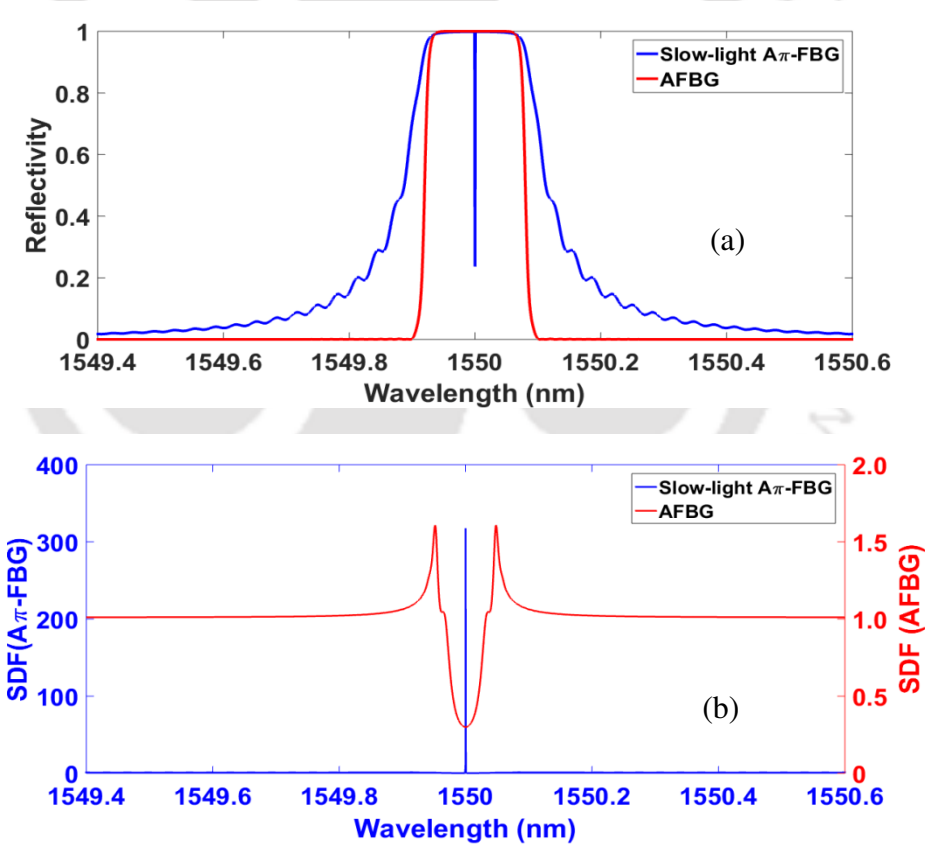

Figure 4.2: (a) Reflectivity spectra of slow-light apodized π-FBG (Aπ-FBG) and conventional apodized FBG (AFBG) (b) slowing down factor for slow-light apodized π-FBG (Aπ-FBG) and conventional apodized FBG (AFBG).

4.2.2 Sensitivity Characteristics of Slow-light π-FBG

Sensitivity of slow-light π-FBG is defined as [134]

$$S_x(\lambda) = \frac{dT(\lambda)}{dx} = \frac{dT(\lambda)}{d\lambda}\frac{d\lambda}{dx} \tag{4.3}$$

where x is the applied external perturbation, $T(\lambda)$ is the wavelength dependent transmissivity of the characteristics Lorentzian line shaped ultra-narrow transmission resonance of π-FBG. Slope of the slow-light grating's Lorentzian transmission resonance, $dT(\lambda)/d\lambda$, is observed to be maximum at $\lambda = \lambda_B \pm \Delta\lambda\sqrt{3}/6$ with a maximum value of $3\sqrt{3}T_0/4\Delta\lambda$. Here, T_0 is the peak transmission at the resonance (Bragg) wavelength and $\Delta\lambda$ is FWHM of the Lorentzian [134]. $\Delta\lambda$ can be related to the group delay τ_g by $\Delta\lambda = \lambda_B^2/\pi c\tau_g$. Thus, Eq. (4.3) can be rewritten as

$$S_x(\lambda) = \frac{4.08c\tau_g T_0}{\lambda_B^2}\frac{d\lambda}{dx} \tag{4.4}$$

FBG is inherently sensitive to the applied strain and temperature perturbations. FBG sensors are also deployed for the measurement of a range of other physical parameters that are smartly and successfully mapped on to the strain or the temperature domain. The basic operational principal of FBG sensor is to monitor the wavelength shift with the changes in the applied strain/temperature perturbations. The Bragg wavelength shift is defined in Eq. (1.7) and can be reformulated as

$$\delta\lambda = \left(K_\varepsilon \delta\varepsilon + K_T \delta T\right)\lambda_B \tag{4.5}$$

where K_ε and K_T are the strain and thermal sensitivity coefficients, respectively. For FBG in silica fiber with λ_B = 1550 nm, $K_\varepsilon \approx 0.78\times10^{-6}\varepsilon^{-1}$ and $K_T \approx 8.6\times10^{-6}{}^{\circ}C^{-1}$. Thus, at constant temperature ($\delta T = 0$) the slow-light strain sensitivity is obtained as:

$$S_\varepsilon(\lambda) = 3.182\times10^{-6}\frac{c\tau_g T_0}{\lambda_B} = 3.182\times10^{-6}\frac{n_g L T_0}{\lambda_B} \tag{4.6}$$

where Eq. (4.4) and Eq. (4.5) are used along with the definition of group-index, $n_g = c\tau_g/L$.

Similarly, at constant strain ($\delta\varepsilon = 0$), the slow-light temperature sensitivity is obtained as

$$S_T(\lambda) = 3.508\times10^{-5}\frac{c\tau_g T_0}{\lambda_B} = 3.508\times10^{-5}\frac{n_g L T_0}{\lambda_B} \tag{4.7}$$

where again Eq. (4.4) and Eq. (4.5) are used along with the relation for group-index.

It can be seen from Eq. (4.6) and Eq. (4.7), that the slow-light sensitivity is proportional to the product $\tau_g T_0$ or equivalently the product $n_g L T_0$, where n_g is the group-index at the resonance wavelength. Thus, the product $n_g L T_0$ (or, $\tau_g T_0$) needs to be maximized in order to achieve maximum slow-light sensitivity. This product is defined as the relevant "figure of merit (FoM)" of slow-light FBG sensors.

4.3 Results and Discussion

A detailed performance analysis of π-FBG that employs apodization profile proposed in Chapter 3 (Eq. (3.1)) is carried out in this section. To do so, optical characteristics, e.g., peak transmissivity and the group delay along with the sensitivity of π-FBG are chosen as the parameters of interest to be investigated. It's important to mention that peak transmissivity, delay, and sensitivity are evaluated at the Bragg wavelength, λ_B, for π-FBG. Effect of grating length (L), index change (δn) and the loss coefficient (α) on the optical and the sensing characteristics of slow-light π-FBG is rigorously studied. For this, L is varied in the range of 10 mm – 70 mm, whereas δn is varied in the range of 0.5×10^{-4} (weak grating) – 5.0×10^{-4} (strong grating). Design (Bragg) wavelength is fixed at 1550.12 nm. CMT along with TMM is used for the

theoretical modelling of the grating structures. All the simulations are performed in MATLAB. Optimum values of the grating parameters (L, δn and α) are determined in order to achieve the best possible response characteristics for the slow-light π-FBG that would lead to an efficient quasi-distributed π-FBG based sensing network. Optical and sensing characteristics of apodized π-FBG are then simulated at the optimum values of L, δn and α. Finally, the application efficiency of the proposed apodized π-FBG with optimized characteristics is investigated while deploying it in a five-stage quasi-distributed temperature and strain sensing network.

In order to investigate the effect of grating length (L), peak transmissivity and the group delay corresponding to the characteristic ultra-narrow transmission peak within the stop band of π-FBG are plotted as a function of L in Figure 4.3 at δn equal to 1.5×10^{-4} and α equal to zero. On the other hand, effect of index-change (δn) is also investigated in order to seek the optimum performance for π-FBG. Peak transmissivity and the group-delay of π-FBG are plotted as a function of δn in Figure 4.4 for a fixed grating length equal to 50 mm and loss coefficient equal to zero. As can be observed from Figure 4.3, as L increases, peak transmissivity initially decreases gradually till L ~ 50 nm, and then onwards, decreases rapidly before trending to zero at L just above 70 mm. Similar behavior is observed in Figure 4.4.

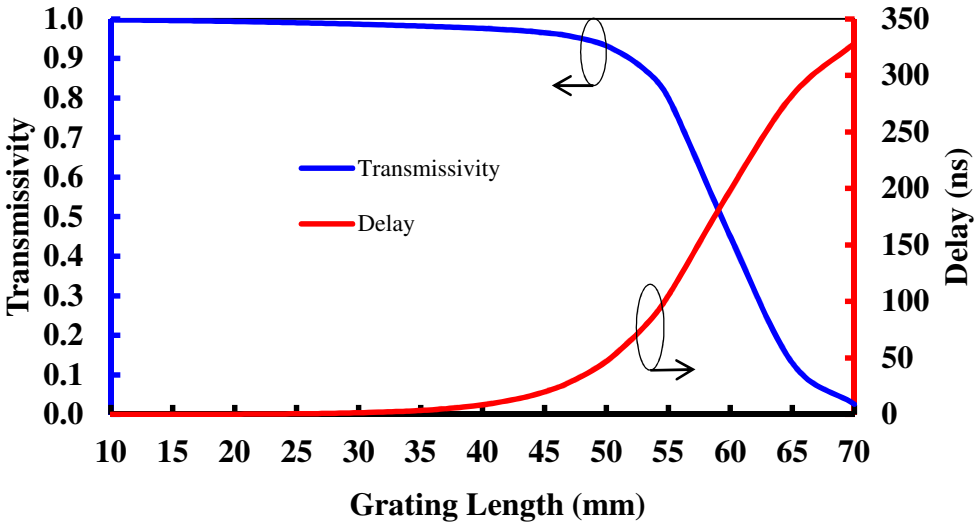

Figure 4.3: Transmissivity and group delay vs. grating length for fixed $\delta n = 1.5\times10^{-4}$ and $\alpha = 0$.

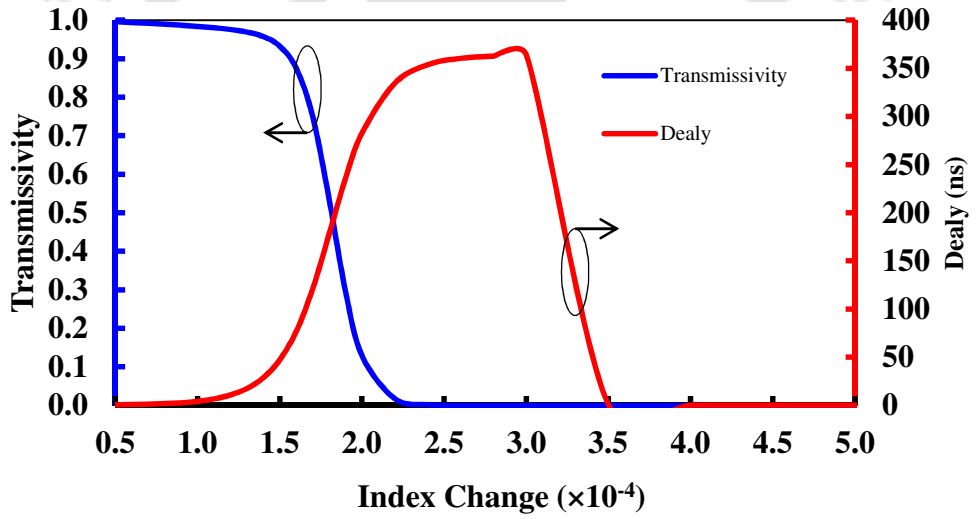

Figure 4.4: Transmissivity and group delay vs index change for fixed $L = 50$ mm and $\alpha = 0$.

While increasing δn, peak transmissivity initially decreases gradually till $\delta n \sim 1.5\times10^{-4}$, and then onwards, decreases rapidly before trending to zero at $\delta n \sim 2.25\times10^{-4}$. The group delay time of slow-light π-FBG shows a different pattern from the transmissivity. As can be observed from Figure 4.3, delay increases gradually till $L \sim$ 45 nm, and then onwards increases continuously and rapidly till $L = 70$ nm. Slightly different behavior is observed while increasing δn at fixed L, which is depicted in Figure 4.4. While increasing δn, the group delay time initially increases very slowly

till δn ~ 1.0×10^{-4}. Then onwards it increases rapidly till δn ~ 2.25×10^{-4}. Further increment in δn results in a very slow increment in the delay till δn ~ 3.0×10^{-4}, there after it decreases rapidly before trending to zero at δn ~ 3.5×10^{-4}. The observed behavior of the optical characteristics (transmissivity and delay) of π-FBG can be explained as following. Increasing the grating length at fixed δn (i.e., at fixed reflectivity of the corresponding FP mirrors) increases the equivalent Fabry-Perot (FP) cavity length of the π-FBG. On the other hand, increasing δn at fixed L enhances the Fabry-Perot (FP) effect within the π-FBG by increasing the reflectivity of the corresponding FP mirrors. Both the effects independently culminate in increasing the strength of the grating. For example, grating is very weak when the value of δn is very low (no grating when δn = 0). Increasing strength of grating results in the increasing intensity of the backward propagating light until it saturates near 100%. In other words, increasing the equivalent Fabry-Perot cavity length owing to the increase of L (at fixed δn) or enhancement of the Fabry-Perot effect in π-FBG owing to the increase of δn (at fixed L), both, result in an increase in the optical path length as well as the reflectivity of π-FBG. This is equivalent to the reduction in the transmissivity of π-FBG. As the reflectivity reaches to the saturation, transmissivity reaches to zero, which is observed at $\delta n = 1.5\times10^{-4}$ for L ~ 70 mm (in Figure 4.3) and at L = 50 mm for δn ~ 2.25×10^{-4} (in Figure 4.4) when α = 0. Further, as the light is trapped within the cavity, increased optical path length owing to the increased cavity length (while increasing the grating length at fixed δn) increases the group delay time as observed in Figure 4.3. On the other hand, increased reflectivity of the corresponding FP mirrors of π-FBG owing to the increased δn (at fixed L) results in the increased number of reflections from the mirrors and the multiple travel of light signal back and

forth within the cavity (π-FBG). This results in an increasing optical path length and hence, increasing group delay time. However, maximum value to which the reflectivity of the FP mirrors can reach is 1. As δn increases beyond 2.25×10^{-4}, reflectivity of the FP mirrors starts approaching towards its maximum value as depicted from the transmissivity behavior of the π-FBG in Figure 4.4. This leads to a very slow increment of the optical path length beyond this value of δn as observed during the variation of δn within the range of ~2.25×10^{-4}–3.0×10^{-4}. Beyond δn ~3.0×10^{-4}, π-FBG becomes too strong and light seizes to penetrate the full length of the grating. This results in a sharp and significant reduction of the light power within the equivalent FP cavity of π-FBG. Naturally, this is reflected in the sharp and significant reduction of the delay in Figure 4.4.

Though ignored in the case of uniform FBG, loss is another very important parameter that not only affects the transmission but also affects the maximum possible delay (slow-light effect) that can be achieved by π-FBG. The loss (manifested by the coefficient α) within the FBG depends upon many factors such as grating fabrication technique and the index change (δn). For example, loss coefficient for an apodized FBG written in the conventional SMF-28 fiber using femtosecond laser can be very low (within a range of 0.02 – 0.9 m^{-1}) [142], whereas it can be as high as 5.8 m^{-1} for an FBG written in a H_2 loaded SMF-28 fiber [83]. In order to investigate the effect of α, peak transmissivity and the group delay characteristic of π-FBG are plotted as a function of L in Figure 4.5. Here, δn is fixed at 1.5×10^{-4}, whereas α is varied from 0.10 m^{-1} to 5.80 m^{-1} as depicted in the figure. Simulated results clearly depict that loss not only reduces the transmissivity but also induces a significant reduction in the achievable group delay. In addition, increasing α results in (a) the transmissivity

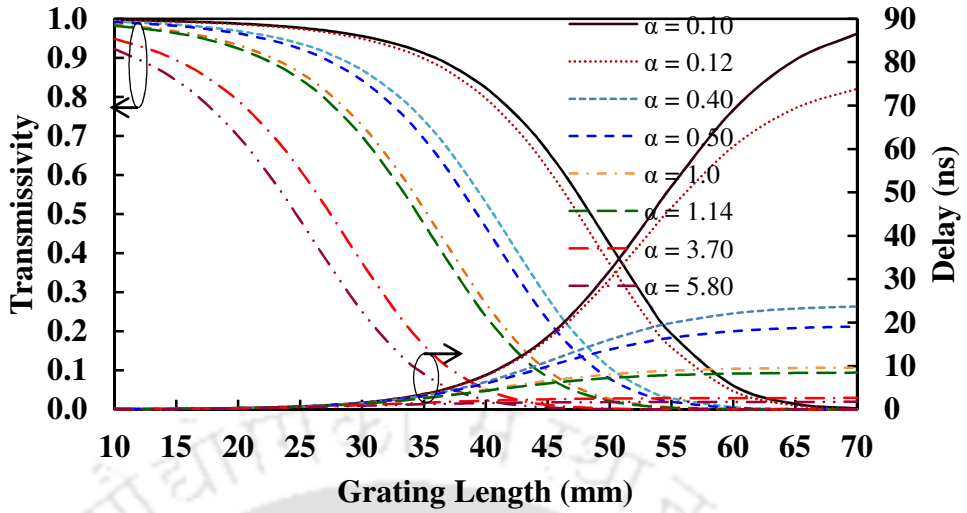

Figure 4.5: Transmissivity and delay vs grating length with different loss coefficients and fixed δn = 1.5 ×10^{-4}.

trending to zero at shorter grating lengths and (b) significant reduction in the incremental rate and then the saturation of the delay. However, increasing loss coefficient results in an increasing loss of the optical signal that shuttles back and forth within the grating. This weakens the optical power gradually and hence, the transmissivity as well as the group delay. Further, in the absence of loss, group-index (n_g) increase with the grating length. Because of the influence of finite loss, group-index seizes to increase indefinitely with the length. Rather, it reaches to maximum at an optimum grating length and then onwards decreases with the grating length [83]. Beyond a certain value of L, the product $L \times n_g$ becomes invariant and hence, the group delay constant. Grating length at which saturation of the delay is observed varies with the loss coefficient as depicted in Figure 4.5.

In the next part of the study, effect of grating length (L), index change (Δn) and loss coefficient (α) on the sensitivity of slow-light π-FBG are investigated. As explained in Section 4.2.2, sensitivity of slow-light π-FBG is directly proportional to the FoM (given by the product $\tau_g T_0$). In order to achieve maximum slow-light sensitivity, FoM needs to be optimized. In order to do so, simulated values of FoM are

plotted as a function of L in Figure 4.6 for the constant values of δn (= 1.5×10^{-4}) and α (= 0). On the other hand, Figure 4.8 illustrates simulated values of FoM as a function of δn for the constant values of L (= 50 mm) and α (= 0). As can be observed from Figure 4.6, while increasing L, FoM increases gradually, reaches its maximum at the grating length of 60 mm and then decreases. Similar behavior is observed in Figure 4.7. While increasing δn, FoM increases gradually, reaches its maximum at δn equal to 1.8×10^{-4} and then decreases. Behavior of FoM against increasing L and δn can be easily understood from the behavior of T_0 and τ_g in Figure 4.3 and Figure 4.4. Product of T_0 and τ_g is maximum at the grating length of 60 mm (while δn is fixed at 1.5×10^{-4}) (Figure 4.3); whereas, it is maximum at the index-change of 1.5×10^{-4} (while L is fixed at 50 mm) (Figure 4.4).

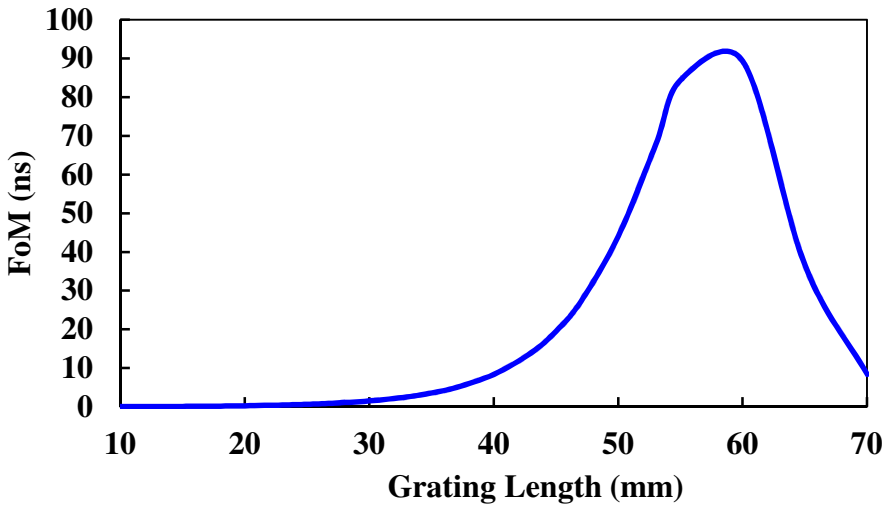

Figure 4.6: FoM vs grating length for $\delta n = 1.5\times10^{-4}$ and $\alpha = 0$.

In order to investigate the effect of α, first, FoM of π-FBG is plotted as a function of δn in Figure 4.8. Here, L is fixed at 50 mm, whereas α is varied from 0.10 m^{-1} to 5.80 m^{-1}. Comparing the results plotted in Figure 4.8 with the results plotted in Figure 4.7 (α = 0), loss not only substantially reduces the maximum achievable FoM but

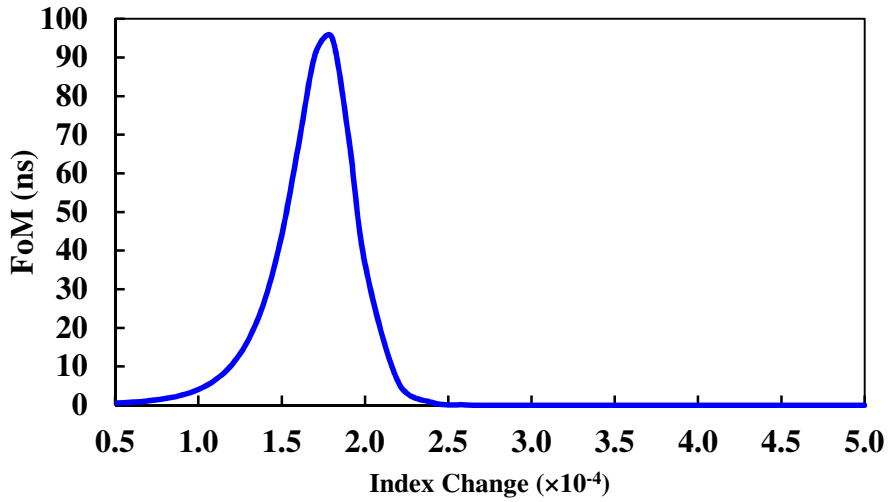

Figure 4.7: FoM vs index change for L = 50 mm and α = 0.

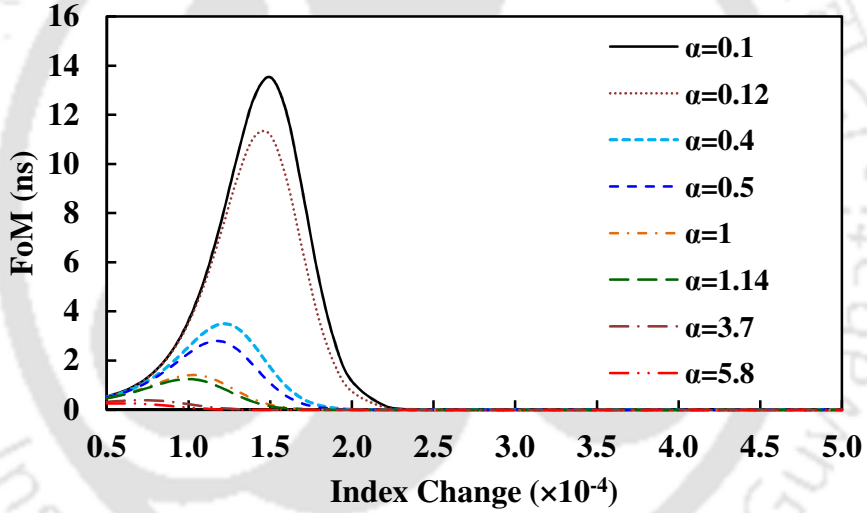

Figure 4.8: FoM vs index change with different loss coefficients and L = 50 mm.

shifts the value of δn at which maximum FoM is obtained to the lower values. For maximum sensitivity, FoM must be highest. Most challenging aspect to attain this objective is to maintain the loss coefficient as low as possible while optimizing FBG as can be observed from Figure 4.8. The lowest loss coefficient, practically achieved and reported in the literature, is 0.10 m^{-1} [134]. Fixing the loss at this minimum value, δn at which FoM is maximum is observed to be 1.5×10^{-4} (Figure 4.8). This value of δn is used while optimizing the grating length in order to achieve maximum FoM. To

do so, FoM of π-FBG is plotted as a function of L in Figure 4.9. Here, δn is fixed at 1.5×10^{-4} whereas α is varied from 0.10 m^{-1} to 5.80 m^{-1}. Comparing the results plotted in Figure 4.9 with the results plotted in Figure 4.6 ($\alpha = 0$), once again loss not only reduces the maximum achievable FoM but shifts the optimum grating length towards the smaller value at which FoM is maximum. This is obvious in the light of results obtained in Figure 4.5. On the basis of observations made here, optimum grating parameters are fixed at grating length equal to 50 mm, index change equal to 1.5×10^{-4} and α equal to 0.10 m^{-1}. As can be observed from Figure 4.9, maximum FoM of 13.5361 ns is obtained at these optimum grating parameters.

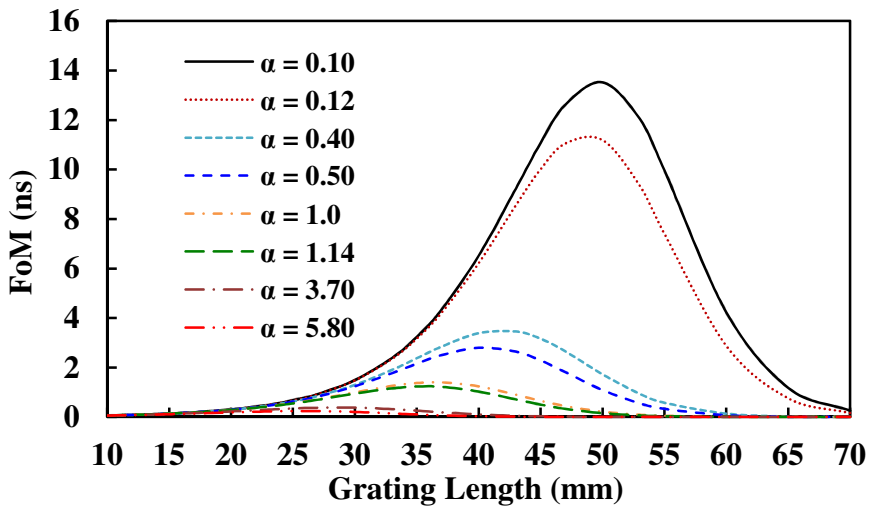

Figure 4.9: FoM vs grating length with different loss coefficients and fixed $\delta n = 1.5\times10^{-4}$.

Optical and sensing characteristics of π-FBG are then simulated at the optimum values of L (= 50 mm), δn (= 1.5×10^{-4}), and α (= 0.10 m^{-1}). Simulated characteristics are shown in Figure 4.10. Proposed slow-light π-FBG is characterized with the peak transmissivity of 0.424, maximum delay of 31.95 ns, the strain sensitivity of 8.380 $\mu\varepsilon^{-1}$, and the temperature sensitivity of 91.064°C^{-1}. In comparison to the reported highest strain and temperature sensitivities (4.0 $(\mu\varepsilon)^{-1}$ [135] and 22.1°C^{-1} [134] respectively), strain sensitivity enhancement of more than two-fold and temperature sensitivity

enhancement of more than four-fold are achieved by the proposed slow-light π-FBG. Further, the FWHM of the characteristic's transmission peak (pass band) of the proposed slow-light π-FBG is observed to be 0.0798 pm as against the overall FWHM of 0.2245 nm for its stop band.

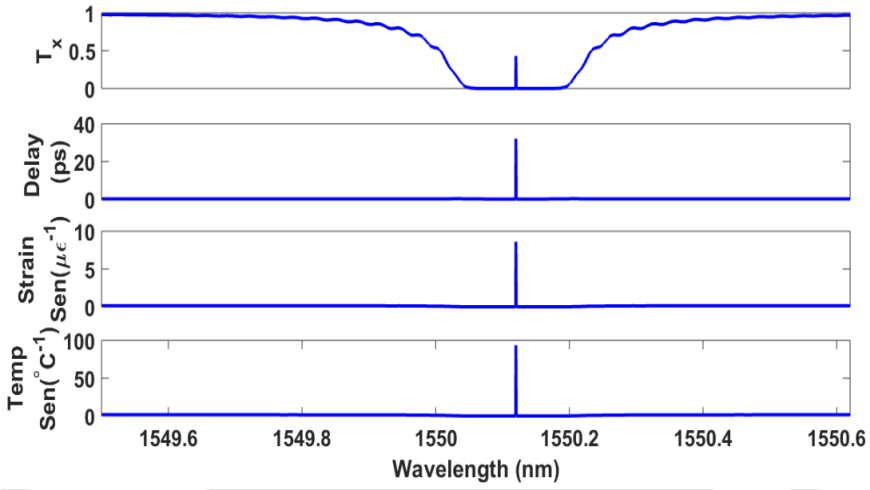

Figure 4.10: Optical and sensing spectra of optimized slow-light π-FBG.

4.4 Quasi-distributed Sensing Application

Slow-light π-FBG with novel apodization profile of Eq. (3.1) and the optimized grating parameters (L = 50 mm, and δn = 1.5×10^{-4} and α = 0.10 m^{-1}) is used in this part of the study. With the promising charactersitics depicted in the previous sections, this slow-light π-FBG is employed in a five-stage quasi-distributed temperature and strain sensing network to analyze its application efficiency. The five-stage quasi-distributed network is constructed employing five π-FBGs with distinct peak resonance wavelengths as λ_{B1} = 1546.12 nm, λ_{B2} = 1548.11 nm, λ_{B3} = 1550.12 nm, λ_{B4} = 1552.12 nm and λ_{B5} = 1554.13 nm. Once again, the spacing of ~2 nm (250 GHz) between the adjacent resonance wavelengths is chosen as per the ITU-T C-band grid recommendations. Figure 4.11 (a) shows the transmission spectrum of this five-

stage quasi-distributed sensing network without any external perturbation applied to any one of the grating. Figure 4.11(b) depicts the strain sensitivity spectrum calculated using Eq. (4.6).

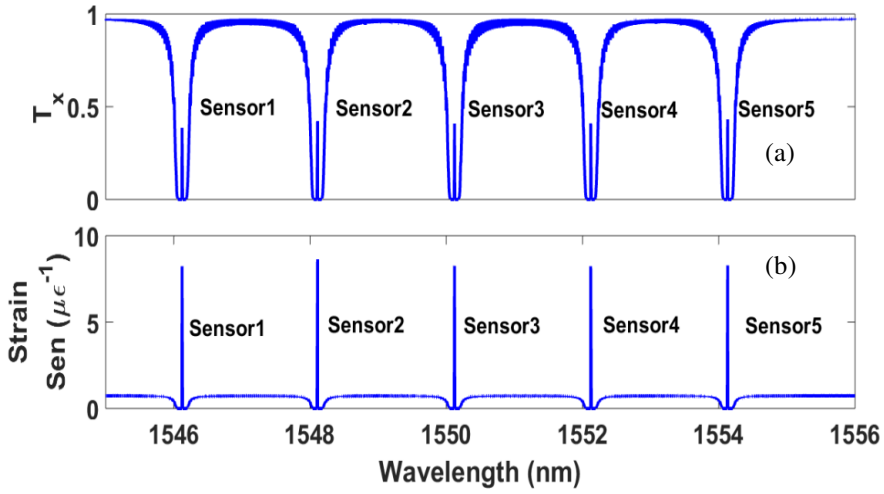

Figure 4.11: (a) Transmission and (b) strain- sensitivity spectra of the proposed slow-light π-FBG in a five-stage quasi-distributed sensing network.

Now strain/temperature perturbations are applied only to the third sensor (λ_{B3} = 1550.12 nm) of this network, keeping other π-FBG sensors free from any external perturbations. Applied strain/temperature perturbations result in the red-shift for λ_{B3}. Maximum permitted red-shift and that ways, maximum applied and still measurable strain/temperature (dynamic range of the measurement) is dictated by the resolution of transmission spectra of the adjacent sensors (π-FBG3 and π-FBG4 in this case). As per the Rayleigh's criterion, maximum permissible red shift for a given π-FBG will be dictated by the difference of wavelength-spacing between the two adjacent gratings and their individual FWHM. With the wavelength-spacing of 2 nm and the FWHM of 0.2245 nm for each π-FBG, maximum allowable red shift is observed to be 1.7755 nm. For this wavelength shift, maximum applied strain and temperature that can be accurately measured are obtained as 1469με and 133°C respectively. This is illustrated in Figure 4.12 for applied strain perturbations. The transmissivity spectrum

is very complicated, while the strain sensitivity spectrum shows two sharp and distinct sensitivity peaks. However, the two sensitivity peaks are not equal, as shown in Figure 4.12 (b). It's important to highlight that the factor $d\lambda/d\varepsilon$ in sensitivity expression of show-light grating sensor (Eq. (4.3)) depends, in general, only on the fiber material and thus, is a constant. Hence, the transmission resonance characteristics (depicted by $dT/d\lambda$), which is proportional to the product $\tau_g T_0$, plays a critical role in defining the sensitivity of the sensor. Applied strain modulates L and δn of the π-FBG, which results in the modulation of transmission and the slow-light characteristics of the 3rd π-FBG sensor, yielding an enhanced value of $\tau_g T_0$ and hence, higher sensitivity peak.

Moreover, the slow-light sensitivity peak is free from the side-lobes, which negates the requirement of the guard band while analyzing the response of the adjacent sensors in the network. This is an additional advantage of slow-light π-FBG based sensing network over the conventional apodized FBG based sensing networks. Furthermore, employing a measurement system having sufficiently wide spectral range will enable the broadening of the FBGs grid (inter-channel spacing) and hence a

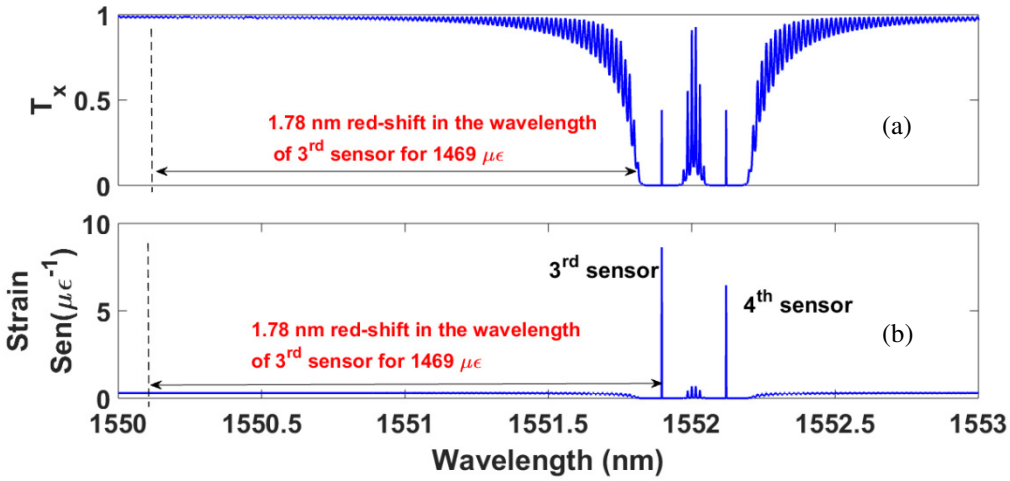

Figure 4.12: Quasi-distributed sensing of optimized slow-light π-FBG with applied strain of 1469 με to the third sensor only.

larger dynamic range for the system.

4.5 Summary

Phase-shifted gratings provide a greater active control on the velocity of the optical signal. This results in achieving a far better sensitivity and resolution while designing sensing applications. In this chapter, optical (transmissivity and delay) and sensing characteristics of slow-light π-FBG are theoretically investigated. The motivation behind the research investigation is to develop an efficient all-optical quasi-distributed sensing network based on slow-light π-FBG and to analyze its response characteristics. To do so, optical characteristics of slow-light π-FBG are optimized with respect to the grating parameters (δn, L, α and the apodization profile). Apodization profile proposed in Chapter 3 is employed to design π-FBG. Sensitivity of slow-light grating depends on the peak transmissivity and the group delay. The optimum grating parameters for which the slow-light π-FBG shows maximum transmissivity and delay are obtained as L= 50 mm, $\Delta n = 1.5\times10^{-4}$, and α = 0.10 m^{-1}. At these parameters, proposed slow-light π-FBG is characterized with peak transmissivity of 0.424 and maximum delay of 31.95 ns. Further, strain sensitivity as high as 8.380 $\mu\varepsilon^{-1}$ and temperature sensitivity as high as 91.064°C^{-1} are achieved for the optimized π-FBG. In comparison to the highest sensitivities reported in the literature, strain sensitivity enhancement of more than two-fold and temperature sensitivity enhancement of more than four-fold are achieved by the proposed optimized π-FBG. Further, the FWHM of the characteristic transmission peak is observed to be 0.0798 pm as against the overall FWHM of 0.2245 nm for its stop band. Finally, the slow-light π-FBG with optimized optical and sensing characteristics is employed in a five-stage quasi-distributed strain and temperature sensing network

to analyze its application efficiency. Dynamic range for the strain measurement as high as 1469με and for the temperature measurement as high as 133℃ are obtained.

Chapter 5 : Design and Analysis of Highly Sensitive Ultrasonic Acoustic Sensor based on π-FBG and Mach-Zehnder Interferometer

A π-phase-shifted fiber Bragg grating (π-FBG) shows high sensitivity to the ultrasonic (US) wave as compared to the conventional FBG due to the strong slow-light phenomenon at the resonance peak. However, its sensitivity is limited by the applied interrogation schemes. In this chapter, a combination of π-FBG and unbalanced fiber Mach-Zehnder interferometer (F-MZI) is theoretically analyzed and optimized for the highly sensitive acoustic sensing applications. Proposed sensing system strongly supports both time and wavelength division multiplexing techniques. Section 5.1 presents the general introduction and a review of the ultrasonic optical fiber sensors. Theoretical modelling of the highly sensitive acoustic sensing system is described in section 5.2. Section 5.3 present the result and discussion and finally summary of the chapter is presented in section 5.4.

5.1 Introduction

Ultrasonic structural health monitoring (SHM) is an effective tool for inside damage of structure by analyzing the time of flight, attenuation, mode conversation, etc. It detects ultrasonic signals that propagate over a long distance within a structure. Over the past few decades, piezoelectric transducer (PZT) is heavily deployed as the most common device for ultrasonic generation as well as ultrasonic detection [143]. However, major limitation of this device is performance degradation in harsh environments, sensitivity to electromagnetic interferences, and incapability of remote sensing and multiplexing. Therefore, during the last few years, fiber-optic ultrasonic sensors have attracted massive attention in various real-field applications including,

but not limited to, structural health monitoring (SHM) of civil infrastructures, aerospace structures, medical diagnostic to name a few. Various fiber-optic ultrasonic sensors for localized applications as well as for quasi-distributed/distributed sensing applications have been reported in the literature [7, 112]. Among these, fiber Bragg grating (FBG) based ultrasonic sensors are mostly used to detect ultrasonic wave in SHM [143]. Reason for the preference of FBG sensor is its inherent features, such as, small size, durability, excellent multiplexing and embedding capabilities.

The working principle of most of the FBG acoustic sensors is based on wavelength modulation in which the dynamic ultrasonic strain wave shifts the Bragg wavelength. However, it is established by theoretical and experimental studies that FBG is hardly sensitive to the ultrasonic (US) wave when the acoustic wavelength is smaller than the grating length [45]. The optimal grating length for the ultrasonic (US) wave detection must be shorter than 1/7 of the acoustic wavelength [144]. Therefore, for the high frequency acoustic ultrasonic wave detection, a short length FBG is needed. However, the short length gratings (weak gratings) suffer from low detection sensitivity due to their reduced peak reflectivity and very moderate reflectivity slope. Recently, Liang *et al*. proposed the novel side-lobe modulation for high frequencies of ultrasonic waves [145]. However, this method requires detection of very weak optical signal since the optical power of the side-lobe used to be much lower than the power at Bragg wavelength. This also limits the achievable sensitivity. A sensor having high sensitivity along with a broad bandwidth would be of extreme importance for ultrasonic detection.

As discussed in Chapter 4, spectrum of π-FBG shows a characteristic single ultra-narrow transmission peak (strong resonance) in the middle of the stop band, whose slope is much steeper than that of the spectrum of conventional FBG. Light at these

resonance frequencies undergoes strong localization centered on the phase shift, which allows to achieve very small sensing length. Additionally, the resonance frequencies exhibit slow-light effect arising from the significantly higher group delay. As already highlighted in the previous chapter, if π-FBG is exploited for the sensing applications, much steeper slope of its single pass band will result in an extraordinary enhancement of the sensitivity. Therefore, in recent years, several sensors based on π-FBG have been proposed for ultrasonic detection [146, 147, 148, 149, 150]. Rosenthal et.al., achieved 10 MHz bandwidth of ultrasonic detection by tuning a CW laser to the maximum slope of the π-FBG resonance and monitoring the reflected intensity by a single photodetector [146]. To minimize the laser intensity noise and to further improve the sensitivity, π-FBG ultrasonic sensor based on Pound-Drever-Hall (PDH) technique was used in [147]. However, this technique requires a tight wavelength tracking for locking the tunable laser source (TLS) frequency to the resonance center or to the midpoint of the linear region in the π-FBG spectra, which makes it very expensive and complicated. A balanced photodetector-based interrogation technique, which is immune to the laser intensity noise was reported in [148]. However, sensitivity is limited by the laser frequency noise and photodetector noise in this technique. Hu *et al*. [149] presented a sensing scheme that employed π-FBG and an imbalanced fiber-optic Michelson interferometer as a reference channel. This scheme offered the potential of multiplexing acoustic sensor systems. A noise reduction ratio of more than 20 dB was achieved. An ultrasonic sensor employing two cascaded π-FBGs and broadband source (BBS) that provided multiplexing capability was demonstrated in [150]. Proposed system offered high sensitivity and broad bandwidth for detecting weak high-frequency ultrasonic waves; however, noise of the system limited the performance.

Interferometric interrogation scheme that employs unbalanced fiber Mach-Zehnder interferometer (F-MZI) offers high resolution, high sensitivity and broad bandwidth for dynamic measurement of strain modulations [140]. In this scheme, reflected signal from the grating structure which is modulated by the applied perturbation (and hence shifted from λ_B by $\Delta\lambda$) is sent through the path-imbalanced F-MZI. F-MZI converts this shift in the wavelength into a change in the intensity, which is proportional to $\Delta\lambda$ and path mismatch d. Therefore, the sensitivity of this scheme can be increased by increasing d. However, the maximum path-length mismatch cannot exceed the coherence length of the signal in the fiber. This coherence length is inversely proportional to the bandwidth of the reflected signal from the FBG [151]. An F-MZI shows the limited sensitivity with the conventional FBGs due to their broader bandwidth (>80 pm).

In this chapter, an ultrasonic acoustic sensor based on π-FBG and F-MZI interrogation scheme is theoretically analyzed and optimized for ultrasonic acoustic sensing application. In order to do so, optical characteristics of π-FBG are optimized for ultrasonic acoustic sensing application w.r.t. grating parameters, grating length (L) and index change (δn). In most of the practical applications, the grating length of 5 mm is used [148, 150]. On the other hand, optimization of index change is done while considering the optical path difference (OPD) of F-MZI, which is a product of the refractive index of fiber and path-length mismatch. The optimum index change is taken as 1.2×10^{-3} in the present study. For the optimum grating parameters (L = 5 mm and $\Delta n = 1.2\times10^{-3}$), π-FBG is characterized by the peak transmissivity of 0.985 and FWHM of 0.012 pm. The OPD of F-MZI is calculated as 76.1 m for the given FWHM. A high strain sensitivity of $1.2321\times10^{8}/\varepsilon$ and a high strain resolution of 4.1 fε/√Hz are achieved for the proposed sensing system. The achieved strain resolution

of the proposed sensing system is much better than 7.3 fε/√Hz of [152] and provides a wavelength shift resolution of 4.9×10^{-9} pm. Best wavelength shift resolution reported for the acoustic-emission sensor based on π-FBG and Michelson interferometer is 3.7×10^{-3} pm [149]. Proposed sensing system shows a much better wavelength resolution than reported in [149]. Further, the intensity noise of BLS in the proposed sensing system can be easily eliminated by using a dual-channel F-MZI configuration [153].

5.2 Theoretical Modelling

5.2.1 Acoustic-Ultrasonic Wave Modelling

Acoustic emission is a transient ultrasonic wave with frequencies typically varying from 100 kHz to 1 MHz. Damage-related structural changes, such as, surface degradation, defect initiation, crack growth, etc. lead to the generation of acoustic emission [149]. A longitudinal ultrasonic (US) acoustic wave can be considered as a longitudinal strain wave propagating along the fiber axis z, whose sinusoidal time dependence can be given as [30]

$$\varepsilon(z,t) = \varepsilon_m \cos\left(\frac{2\pi}{\lambda_S} z - \omega_S t\right) \tag{5.1}$$

where ε_m is the US acoustic strain field amplitude normalized to the US acoustic wavenumber $2\pi/\lambda_S$. λ_S and ω_S are wavelength and angular frequency of US acoustic wave, respectively.

When longitudinal US acoustic wave, as described by Eq. (5.1), propagates through the FBG, it changes (a) the effective refractive index due to the elasto-optic effect, termed as optical contribution and (b) period of the grating due to the mechanical effect, termed as geometrical contribution. Due to the later contribution, a

given point (0, 0, z) within the grating is translated to a new position (0, 0, z') along the grating. This new position is given by [30]

$$z' = f(z,t) = z + \int_0^z \varepsilon(\xi)\, d\xi = z + \varepsilon_m \frac{\lambda_s}{2\pi}\left[\sin\left(\frac{2\pi}{\lambda_s} z - \omega_s t\right) + \sin(\omega_s t)\right] \tag{5.2}$$

On the other hand, the change in the optical indicatrix ($1/n^2$) due to the elasto-optics effect while applying strain is given as [7]

$$\delta\left(\frac{1}{n^2}\right)_i = \sum_{j=1}^{6} p_{ij} S_j \tag{5.3}$$

Here, p_{ij} is the strain-optic tensor and S_j is the strain vector. For the optical fiber, which is homogeneous and isotropic, p_{ij} is given by

$$p_{ij} = \begin{bmatrix} p_{11} & p_{12} & p_{12} & 0 & 0 & 0 \\ p_{12} & p_{11} & p_{12} & 0 & 0 & 0 \\ p_{12} & p_{12} & p_{11} & 0 & 0 & 0 \\ 0 & 0 & 0 & p_{44} & 0 & 0 \\ 0 & 0 & 0 & 0 & p_{44} & 0 \\ 0 & 0 & 0 & 0 & 0 & p_{44} \end{bmatrix} \tag{5.4}$$

Whereas, for an applied longitudinal strain ε, strain vector S_j is given by

$$S_j = \begin{bmatrix} \varepsilon(z,t) \\ -\nu\varepsilon(z,t) \\ -\nu\varepsilon(z,t) \\ 0 \\ 0 \\ 0 \end{bmatrix} \tag{5.5}$$

Here, ν is the Poisson's ratio. Further, change in the indicatrix can be related to a change in the refractive index δn by [7]

$$\delta\left(\frac{1}{n^2}\right) = -2\frac{\delta n}{n^3} \tag{5.6}$$

In the absence of shear strain, change in the refractive index can be obtained by solving above mentioned equations. This change in the refractive index is given as:

$$\delta n'\left(z',t\right) = -\left(\frac{n_{eff}^3}{2}\right)\left[p_{12} - \upsilon\left(p_{11}+p_{12}\right)\right]\varepsilon_m \cos\left(\frac{2\pi}{\lambda_s}z' - \omega_s t\right) \tag{5.7}$$

Thus, the effective refractive index modulation due to the action of US wave is rewritten as:

$$\begin{aligned} n'_{eff}\left(z',t\right) = n_{eff} + \overline{\delta n}\left(1 - \nu\cos\left[\frac{2\pi}{\Lambda}f^{-1}\left(z',t\right)\right]\right) \\ -\left(\frac{n_{eff}^3}{2}\right)\left[p_{12} - \upsilon\left(p_{11}+p_{12}\right)\right]\varepsilon_m \cos\left(\frac{2\pi}{\lambda_s}z' - \omega_s t\right) \end{aligned} \tag{5.8}$$

Once, the effective refractive index modulation is defined, the transmissivity/reflectivity characteristics of π-FBG under ultrasonic wave can be obtained by solving the CMT and TMM.

5.2.2 Sensor System Modelling

The schematic diagram of the proposed sensing system is shown in Figure 5.1. The transmitted spectrum of π-FBG is shown in the inset at the left-bottom of Figure 5.1. Proposed scheme exploits the characteristic single ultra-narrow transmission peak (strong resonance) in the middle of the stop band of π-FBG for sensing purpose. To apply the sensing mechanism, this ultra-narrow transmission peak needs to be filtered. Optical filtering of the ultra-narrow transmission peak in the transmitted spectrum of π-FBG is performed by suitably using an optimized apodized FBG (AFBG). Reflection spectrum of this AFBG filter is shown in the inset at the left-top of Figure

5.1. A chirped FBG can also be used as a filter owing to its top-hat reflection spectrum. However, the (relatively small) chirp rate and an appropriate grating length should be chosen to ensure high reflection coefficient and desired spectral width. Output of a broadband light source (BLS) is fed to the π-FBG sensor. Transmitted light signal from π-FBG sensor is then fed to an AFBG filter through a circulator. If the design parameters such as bandwidth, central wavelength and δn are suitably chosen, then the reflected light from the filter will retain only the central ultra-narrow transmission peak as depicted across the port "3" of the circulator in Figure 5.1. The filtered peak retains the entire characteristics of π-FBG and act as source input to the interferometer for high resolution measurement.

When the ultrasonic wave is applied to the system, output filtered power at the port "3" of the circulator is given as:

$$P_{filter-out} = \int P_0(\lambda) T_{\pi-sensor}(\lambda) R_{AFBG}(\lambda) d\lambda \tag{5.9}$$

where P_0 is the broadband light source (BLS) output optical power, $T_{\pi\text{-}sensor}$ denotes

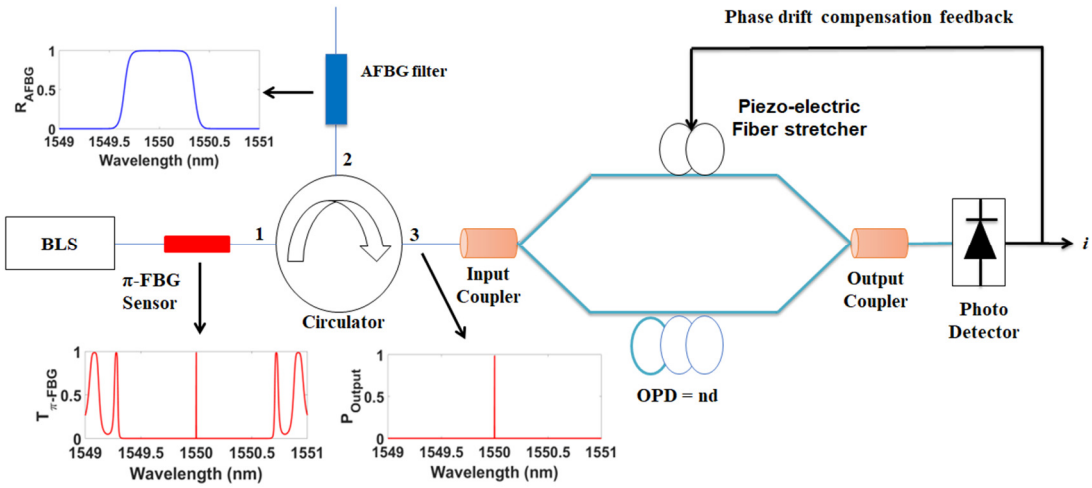

Figure 5.1: Schematic of π-FBG ultrasonic acoustic sensor using interferometric interrogation technique.

the transmissivity of the π-FBG sensor, and R_{AFBG} is the reflectivity of AFBG filter. The F-MZI output power is the coherent sum of fields traveling in lower and upper arms. For the ideal 50% coupling at both F-MZI couplers, the output power is given by

$$P = 0.5P_{filter-out}\left(1+\cos\left(\psi(\lambda)+\phi\right)\right) \tag{5.10}$$

where $\psi(\lambda) = 2\pi nd/\lambda$ is the phase difference due to the path-length mismatch /imbalance of F-MZI; d is the path-length mismatch between the two fiber arms of F-MZI; n is the effective mode index in the fiber; and ϕ is a bias phase offset of the F-MZI. The F-MZI sensitivity is maximum for the phase bias of π/2. For the ultrasonic strain perturbation, it's the second term of Eq. (5.10) that is detected at the output of the sensor. Thus, Eq. (5.10) under the small $\psi(\lambda)$ approximation and ignoring the negative sign, becomes

$$P = 0.5P_{filter-out}\psi(\lambda) \tag{5.11}$$

Phase of the F-MZI changes due to the modulation of Bragg wavelength of π-FBG by ultrasonic strain wave. This change in the phase of F-MZI can be described as:

$$\left|\Delta\psi(\lambda)\right| = \frac{2\pi nd}{\lambda^2}\Delta\lambda_B \tag{5.12}$$

where $\Delta\lambda_B$ is the change in Bragg wavelength due to ultrasonic acoustic waves. The product nd is known as the optical path difference (OPD). For the maximum sensitivity, the optimum OPD satisfies the condition: $OPD\times\delta k = 2.355$ [151]. Here δk is the spectral bandwidth of optical signal fed to the F-MZI.

Finally, the grating response to the longitudinal ultrasonic (US) perturbation needs to be quantified in terms of the sensitivity of the system. It has been shown that the

amplitude of Bragg wavelength modulation ($\delta\lambda_{US}$) due to the US-induced strain wave depends on the ratio of US wavelength to the grating length (λ_S/L) and the strain wave amplitude (ε_m). Thus, Bragg wavelength shift sensitivity (S_λ) can be defined as [30]

$$S_\lambda\left(\lambda_S/L,\varepsilon_m\right)=\frac{\delta\lambda_{US}\left(\lambda_S/L,\varepsilon_m\right)}{\lambda_{B0}\varepsilon_m} \tag{5.13}$$

On the other hand, normalized power sensitivity of the sensor system towards the ultrasonic acoustic strain field (S_ε) can be derived as

$$S_\varepsilon=\frac{1}{P_{filter-out}}\frac{dP}{d\varepsilon}=\frac{1}{P_{filter-out}}\frac{dP}{d\psi}\frac{d\psi}{d\lambda}\frac{d\lambda}{d\varepsilon}=\frac{0.78\pi nd}{\lambda^2}\lambda_B \tag{5.14}$$

5.3 Numerical Results and Discussion

As the OPD plays a critically important role in the proposed sensing scheme, π-FBG is optimized to achieve optimum OPD for the F-MZI. As already highlighted in the previous section of this chapter, proposed scheme converts the wavelength shift ($\Delta\lambda$) resulting from the applied perturbation into a relative intensity change, which is proportional to $\Delta\lambda$ and path mismatch d within F-MZI. OPD of the F-MZI is a product of the refractive index of fiber and d. Therefore, the sensitivity of this scheme can be increased by increasing the OPD. However, the maximum path-length mismatch cannot exceed the coherence length of the signal in the fiber, which limits the maximum achievable OPD. This coherence length is inversely proportional to the bandwidth of the reflected signal from the FBG. Thus, wider the bandwidth of the reflected signal from the grating, the lower will be the coherence length and hence, the effective and achievable OPD. As the reflected signal is the central characteristic ultra-narrow transmission peak, π-FBG used in the present work is considered to be lossless in the light of the physics discussed in the previous chapter.

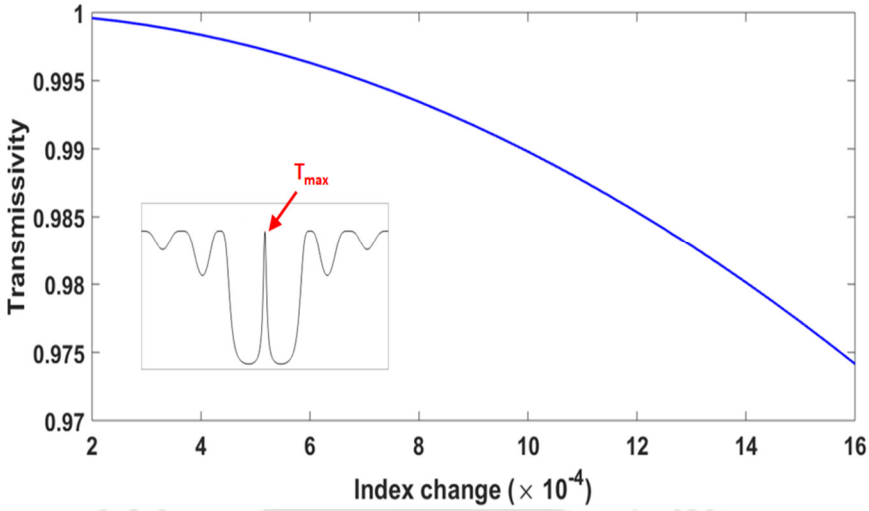

Figure 5.2: Transmissivity vs. index change for fixed L = 5 mm (inset figure shows the peak transmissivity of π-FBG at Bragg wavelength).

The typical length of grating is taken as 5 mm, which is commonly used in most of the studies reported in the literature. Figure 5.2 shows the change in the resonance peak transmissivity of π-FBG as a function of index change. As the index change increases, transmissivity decreases. As explained in the previous chapter, increasing δn at fixed L enhances the Fabry-Perot effect within π-FBG. These results in the increased strength of the grating, thereby, increased reflectivity and equivalently decreased transmissivity. For better detection or signal to noise ratio, the resonance peak transmissivity must be as high as possible [149].

Bandwidth of the signal reflected from the AFBG reflector of the F-MZI, that is FWHM of the transmission resonance peak, which plays a critical role in achieving higher sensitivity is plotted as a function of index change in Figure 5.3. As can be observed from the figure, FWHM decreases linearly on a logarithmic scale as δn increases.

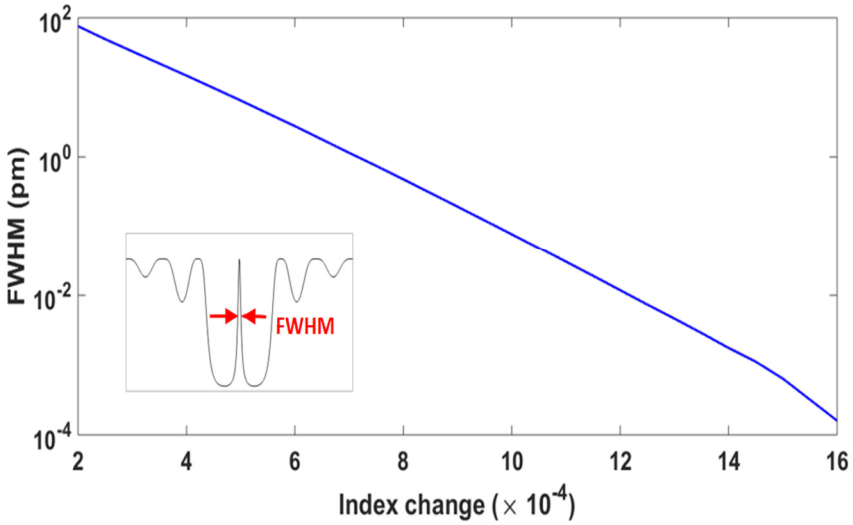

Figure 5.3: FWHM of resonance peak of π-FBG vs. index change for fixed L = 5 mm (inset figure shows the FWHM of π-FBG at Bragg wavelength).

To investigate the effect δn, OPD is plotted as a function of index change in Figure 5.4. As can be observed from the figure, OPD increases linearly on the logarithmic scale as δn increases. To the best of author knowledge, a maximum OPD of 96 m was used in a fiber laser-based F-MZI sensor system [152]. Considering this as the maximum limit of OPD, corresponding index change of 1.2×10^{-3} is obtained from Figure 5.4. Considering the selected values of grating parameters L = 5 mm and

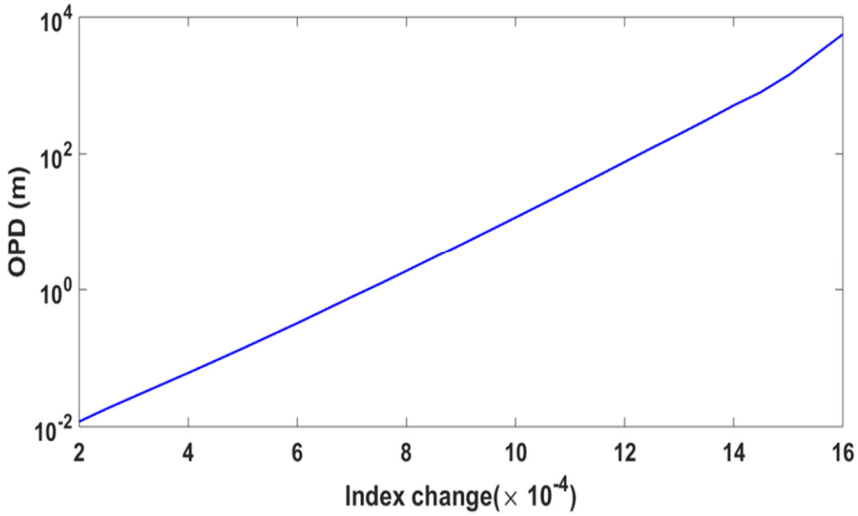

Figure 5.4: OPD of F-MZI vs index change.

δn = 1.2×10^{-3} as the optimum grating parameters, peak transmissivity and FWHM for π-FBG are calculated as 0.985 and 0.012 pm, respectively. For this value of FWHM, OPD of F-MZI employing the optimized π-FBG is calculated as 76.1 m.

Bragg wavelength shift sensitivity, $S\lambda$, is plotted as a function of λ_S/L for the optimized π-FBG in Figure 5.5. In order to simulate the Bragg wavelength shift sensitivity characteristics, the amplitude of US-induced strain wave is taken as 100 με. As can be observed from Figure 5.5, wavelength shift sensitivity for the optimized π-FBG approaches maximum and then attains a constant sensitivity for λ_S/L>2. The grating length (L) at which maximum sensitivity $S\lambda$ is observed in the present study is five times lower than the grating length at which maximum $S\lambda$ is achieved in [30] and 3.5 times lower than the length reported in [144].

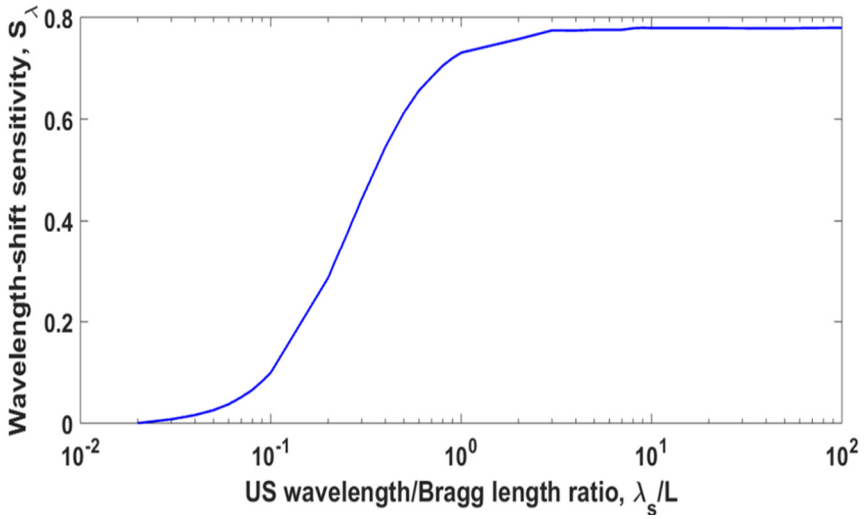

Figure 5.5: Bragg wavelength shift sensitivity of π-FBG, S_λ vs. the US wavelength for the strain amplitude of 100 με.

Next, the simulated strain sensitivity of F-MZI, S_ε , is plotted in Figure 5.6. The strain sensitivity is evaluated for the optimized OPD of 76.1 m. As can be observed, the maximum strain sensitivity of 1.21321×10^8/ε is obtained for λ_S/L>2. The maximum phase sensitivity ($\delta\psi/\delta\varepsilon$) that corresponds to the maximum strain sensitivity

is calculated as 240 rad/με. Considering the high-resolution dynamic phase shift of 1 μrad/√Hz for F-MZI [151] and observed phase sensitivity, a high dynamic strain resolution of 4.1 fε/√Hz is observed for the present sensor system. The strain resolution of the proposed sensing system is nearly half as compared to the strain resolution of 7.3 fε/√Hz for the fiber laser sensor reported in [152]. Further, for the achieved strain resolution of 4.1 fε, a wavelength shift resolution of 4.92×10^{-9} pm is easily obtained. A wavelength shift resolution of 3.7×10^{-3} pm is reported in [149] for the acoustic-emission sensor based on π-FBG and Michelson interferometer. The proposed sensor shows a much better wavelength resolution than that presented in [149].

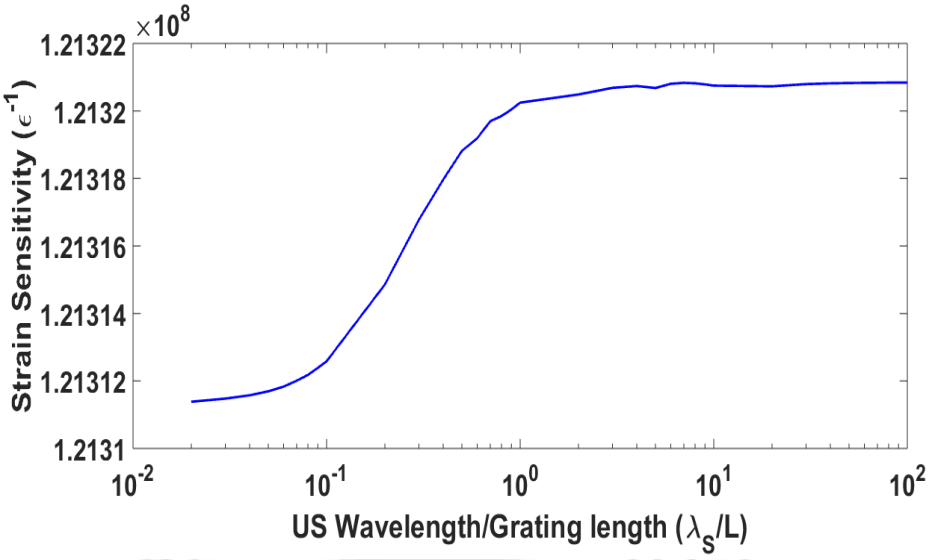

Figure 5.6: Strain sensitivity of π-FBG, S_ε vs. the US wavelength for the strain amplitude of 100 με.

Finally, to depict the other aspects of the proposed sensing system, Bragg wavelength shift and the wavelength-shift sensitivity, $S\lambda$, for the optimized π-FBG is plotted as a function of US acoustic strain amplitudes in Figure 5.7. The ratio λ_S/L is taken as 3. Bragg wavelength shifts linearly with the strain amplitude with a slope of 1.2 pm/με. However, a constant value of 0.774 is obtained for $S\lambda$. The result shows

that for the ratio $\lambda_S/L>2$, the proposed π-FBG experiences uniform distribution of strain along the grating length.

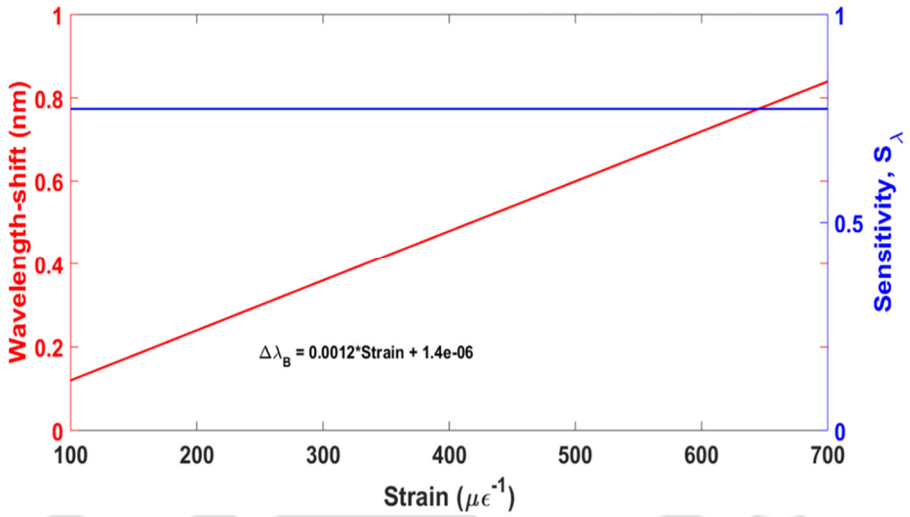

Figure 5.7: The Bragg wavelength-shift and sensitivity of optimized π-FBG vs. strain.

As previously discussed, to filter out the resonance peak of π-FBG, a suitable apodized FBG filter is required. Apodization profile proposed in Eq. (3.1) is used for designing the AFBG filter to be employed in the present sensor system. For this AFBG, the grating parameters are taken as L = 10 mm, and $\delta n = 7\times10^{-4}$. Simulated spectrum of the designed AFBG filter is depicted in the top-left corner of Figure 5.1. The flat-topped bandwidth of the AFBG filter is observed to be 0.51 nm, which is capable filtering the resonance peak for ±200 με US strain amplitudes.

5.4 Summary

In this chapter, a combination of π-FBG and unbalanced fiber Mach-Zehnder interferometer (F-MZI) is theoretically analyzed and optimized for the highly sensitive ultrasonic acoustic sensing applications. Numerical investigations show that π-FBG ultrasonic sensor exhibits better sensitivity at high frequency as compared to the conventional FBGs ultrasonic sensors. This is because of the fact that light at the resonance frequencies of the strong ultra-narrow transmission peak within the stop

band of π-FBG undergoes strong localization resulting in a significantly higher group delay and hence, the sensitivity. Optical characteristics of π-FBG are optimized for ultrasonic acoustic sensing application w.r.t. L and δn. Further the sensor characteristics are optimized w.r.t. the optical path difference (OPD) of F-MZI. Proposed sensing system shows the theoretical highest strain sensitivity of $1.21321\times10^{8}/\varepsilon$ and a theoretical dynamic strain resolution of 4.1 fε/√Hz. The achieved strain resolution provides a theoretical wavelength shift resolution of 4.9×10^{-9} pm, which is much better than the reported values in the literature. The achieved strain resolution provides a wavelength shift resolution of 4.9×10^{-9} pm, which is far better than reported in the literature. The strain sensitivity, resolution, and wavelength-shift sensitivity of the proposed sensing system can further be enhanced by increasing the path mismatch of F-MZI to the coherent length, $\lambda^2/n_{eff}\delta\lambda$, where $\delta\lambda$ is spectral bandwidth of transmission resonance peak of π-FBG. Moreover, the proposed sensing system strongly supports both time and wavelength division multiplexing techniques. Therefore, the proposed sensing system shows extreme importance in single as well as quasi-distributed US acoustic wave sensing networks.

Chapter 6 : Conclusions and Scope for Future Work

In this chapter, conclusions of the various studies and investigations that were carried out in the thesis are presented. Furthermore, possible works that can be carried out in the future as a contribution of the present work are highlighted.

6.1 Conclusion

Fiber Bragg grating (FBG) based WDM sensing networks have become integral part of various engineering applications, including but not limited to civil, mechanical, aeronautical and environmental engineering. Multi-point sensing with accurate and reliable feedback is very crucial in all such applications, which is established in Chapter 1, which also presents in-depth review of the current state-of-the-art research progress and issues to be addressed. As highlighted, number of sensors in the WDM sensing system is limited by the bandwidth of the light source, dynamic range and the optical characteristics of each FBG sensor, which heavily affects the design and implementation of quasi-distributed all-optical sensing network. Ultra-narrow FWHM and greater degree of SLSR are the two most critically important factors among the other that are key to realize an efficient and optimized WDM/quasi-distributed sensing network. In this thesis, novel FBG structures are proposed for its efficient application in quasi-distributed sensing network and to enhance the sensing capabilities. Primary focus of the research is to achieve higher sensing efficiency, sensitivity, measurement accuracy and the dynamic range of the measurement in individual/distributed sensing application. Rigorous theoretical study and analysis for (a) the optimization of optical and sensing characteristics of FBG sensor and (b) its response-characteristics in quasi-distributed sensing network are carried out. Foundation of the theoretical aspect and techniques require for

numerically analyze the response characteristics of grating structure is presented in Chapter 2.

A novel symmetrical apodization profile for tailoring FBG that predominantly focuses on to achieve higher degree of SLSR without much compromise at the reflectivity and FWHM, thus facilitating high SNR and minimum channel-cross-talk is proposed to design FBG for efficient quasi-distributed sensing application in Chapter 3. A rigorous optimization and comparative analysis is carried out in order to investigate the merits of the proposed apodization profile over to the elite apodization profiles. Best side-lobe suppression characteristics along with a FWHM of 0.14 nm (< 0.2 nm) and reflectivity of 0.607 (> 0.5) are observed for the proposed grating at optimized parameters (10 mm grating length and 0.9×10^{-4} index-change). While deploying the proposed grating in a five-stage quasi-distributed sensing network, dynamic range as high as 131.6°C for temperature and as high as 1450με for strain measurement are obtained. Further, an isolation of 10.07 dB and the total isolation of 33.818 dB, highest among the other apodization profiles recently reported in the literature, are observed for the proposed FBG. These results depict that the proposed apodized grating exhibits optimum optical characteristics of grating, and when deployed in a quasi-distributed sensing network it results in an optimum guard band requirement – leading to the highest possible isolation between the adjacent sensors ~~as~~ in comparison to the other apodization profiles proposed in the literature.

Phase-shifted gratings provide a greater active control on the light confinement and the resulting group delay. This result in achieving a far better sensitivity and resolution while designing sensing applications based on such grating structures. In order to further enhance the sensing efficiency, slow-light π-FBG based quasi-distributed sensing network is proposed in Chapter 4. A novel π-FBG is designed by

optimizing its optical (peak transmissivity and the group delay) and sensing characteristics with respect to the grating parameters (length, index-change, loss and apodization). Strain sensitivity as high as 8.380 $(\mu\varepsilon)^{-1}$ and temperature sensitivity as high as 91.064°C^{-1} are achieved for the optimized π-FBG. Observed sensitivities are manifold higher than the maximum sensitivities reported in the literature. Optimized slow-light π-FBG is employed in a five-stage quasi-distributed sensing network. Dynamic range for the strain measurement as high as 1469με and for the temperature measurement as high as 133°C are obtained.

Finally, highly sensitive ultrasonic acoustic sensing system is developed in Chapter 5 by employing π-FBG and unbalanced fiber Mach-Zehnder interferometer. Characteristics of π-FBG are optimized for ultrasonic signal detection. At optimum grating parameters, peak transmissivity of 0.985 and FWHM of 0.012 pm are achieved for π-FBG. Further, strain sensitivity as high as $1.21321\times10^{8}/\varepsilon$ and resolution as high as 4.1 fε/√Hz are achieved from the proposed sensor. Observed strain sensitivity and resolution are much better than the best reported in the literature.

6.2 Future Research Work

Multi-point sensing in the form of quasi-distributed sensing network is realized and theoretically investigated with an objective to achieve higher sensing efficiency, sensitivity, measurement accuracy and the dynamic range of the measurement. Grating structure in the form of uniquely apodized FBG and π-FBG are designed for the theoretical investigation not only to achieve optimum individual optical characteristics but to achieve greater application efficiency in a quasi-distributed sensing network. Far better response characteristics are achieved in comparison to the reported response in the literature. However, there are further scopes of improvement

as for as real-field application is concerned. Based on the theoretical investigations carried out in the present thesis, the following recommendations are proposed as the future work in continuation:

- Apodized FBG sensors are characterized with better resolution and performance as compared to the uniform gratings. However, these sensors are utilized as a point sensor. The analytical study of apodized gratings for quasi-distributed sensing networks proposed in this thesis needs to be experimentally validated.
- Slow-light in π-FBG for quasi-distributed static measurements is described in Chapter 4. Detection techniques of slow-light grating sensors are different from the conventional FBG sensors. The interrogation system for slow-light π-FBG based quasi-distributed sensing networks enabling static measurements needs to be designed and experimentally characterized.
- The experimental verification of acoustic sensing system based on π-FBG and unbalanced F-MZI presented in this thesis is to be conducted.

References

[1] B. Pal, Fundamentals of fiber optics in telecommunication and sensor systems, New Age Inc., 2003.

[2] K. Y. Wong, "Instrumentation and health monitoring of cable-supported bridges," *Struct. Control Health Monit.,* vol. 11, no. 2, pp. 91-124, 2004.

[3] F. J. Tressler, S. Alkoy and R. E. Newnham, "Piezoelectric sensors and sensor materials," *J. Electroceram.,* vol. 2, no. 4, pp. 257-272, 1998.

[4] H. Nassif, M. Gindy and J. Davis, "Comparison of laser Doppler vibrometer with contact sensors," *Non Destructive Testing and Evaluation International (NDT&E Int.),* vol. 38, no. 3, pp. 213-218, 2005.

[5] J. Lee and M. Shinozuka, "A vision-based system for remote sensing of bridge displacement," *Non Destructive Testing and Evaluation International (NDT&E Int.),* vol. 39, no. 5, pp. 425-431, 2006.

[6] C. K. Kao and G. A. Hockham, "Dielectric fiber surface waveguides for optical frequencies," *Proc. IEEE,* vol. 113, no. 7, p. 1151–1158, 1966.

[7] G. Wild and S. Hinckley, "Acousto-ultrasonic optical fiber sensors: Overview and state-of-the-art," *IEEE Sens. J.,* vol. 8, no. 7, pp. 1184 - 1193, 2008.

[8] J. M. Nichols, S. T. Trickey, M. Seaver and L. Moniz, "Use of fber-optic strain sensors and holder exponents for detecting and localizing damage in an experimental plate structure," *J. Intelligent Material Systems*

and Structures, vol. 18, p. 51–67, 2007.

[9] H. Murayama, K. Kageyama, K. Uzawa, K. Ohara and H. Igawa, "Strain monitoring of a single-lap joint with embedded fber Strain monitoring of a single-lap joint with embedded fber," *Struct. Health Monit.,* vol. 11, no. 3, p. 325–344, 2011.

[10] C. Pang, M. Yu, A. K. Gupta and K. M. Bryden, "Investigation of smart multifunctional optical sensor platform and its application in optical sensor networks," *Smart Mater. Struct. ,* vol. 12, no. 1, p. 23–39, 2013.

[11] G. Mudhana, K. S. Park, S. Y. Ryu and B. H. Lee, "Fiber-Optic Probe Based on a Bifunctional LensedPhotonic Crystal Fiber for Refractive IndexMeasurements of Liquids," *IEEE Sens. J.,* vol. 11, no. 5, pp. 1178-1183, 2011.

[12] P. Morris, A. Hurrell, A. Shaw, E. Zhang and P. Beard, "A Fabry-Perot fiber-optic ultrasonic hydrophone for the simultaneous measurement of temperature and acoustic pressure," *J. Acoust. Soc. Am.,* vol. 125, no. 6, p. 3611–3622, 2009.

[13] B. Culshaw and A. Kersey, "Fiber-Optic Sensing: A Historical Perspective," *J. Lightw. Technol.,* vol. 26, no. 9, pp. 1064-1078, 2008.

[14] M. Digonnet, H. Wen, M. Terrel and S. Fan, "Slow Light in Fiber Sensors," in *Proc. SPIE*, 2012.

[15] J. López-Higuera, L. R. Cobo, A. Q. Incera and A. Cobo, "Fiber optic sensors in structural health monitoring," *J. Lightw. Technol.,* vol. 29, no. 4,

p. 587–608, 2011.

[16] R. Perez-Herrera and M. Lopez-Amo, "Fiber optic sensor networks," *Opt. Fiber Technol.,* vol. 19, p. 689–699, 2013.

[17] R. Aneesh and S. K. Khijwania, "Zinc oxide nanoparticle based optical fiber humidity sensor having linear response throughout a large dynamic range," *Appl. Opt.,* vol. 50, no. 27, pp. 5310-5314, 2011.

[18] P. Munendhar, R. Aneesh and S. K. Khijwania, "Development of an all-optical temperature insensitive nonpendulum-type tilt sensor employing fiber Bragg gratings," *Appl. Opt.,* vol. 53, no. 16, pp. 3574-3580, 2014.

[19] S. A. Slattery, D. N. Nikogosyan and G. Brambilla, "Fiber Bragg grating inscription by high intensity femtosecond UV laser light: Comparison with other existing methods of fabrication," *J. Opt. Soc. Am. B* , vol. 22, no. 2, p. 354–361, 2005.

[20] R. Kashyap, Fiber Bragg gratings, 2nd ed., Academic Press, 2010.

[21] A. Othonos, K. Kalli, D. Pureur and A. Mugnier, "Fibre Bragg gratings," in *Wavelength Filters in Fibre Optics*, Springer, 2006, p. 189–269.

[22] H. Y. Au, S. K. Khijwania, H. Y. Fu, W. H. Chung and H. Y. Tam, "Temperature-Insensitive Fiber Bragg Grating Based Tilt Sensor With Large Dynamic Range," *J. Lightw. Technol.,* vol. 29, no. 11, pp. 1714-1720, 2011.

[23] C. C. Ma and K. C. Chuang, "Investigation of the transient behavior of

a cantilever using a point-wise fiber Bragg grating displacement sensor system," *Smart Mater. Struct.,* vol. 17, pp. 1-11, 2008.

[24] M. I. Comanici, L. R. Chen, P. Kung and L. Wang, "Measurement of dynamic strain using a fiber Bragg grating-based laser sensor system," in *2011 ICO International Conference on Information Photonics*, 2011.

[25] Y. Zhan, S. Xue, Q. Yang, S. Xiang, H. He and R. Zhu, "A novel fiber Bragg grating high temperature sensor," *Opt-Int. J. Light Electron Opt.,* vol. 119, no. 11, pp. 535-539, 2008.

[26] T. L. Yeo, T. Sun, K. T. V. Grattan, D. Parry, R. Lade and B. D. Powell, "Characterisation of a polymer-coated fibre Bragg grating sensor for relative humidity sensing," *Sens. Actuaters B,* vol. 110, no. 1, pp. 148-156, 2005.

[27] J. Wang, L. Zhao, T. Liu, Z. Li, T. Sun and K. T. V. Grattan, "Novel Negative Pressure Wave-Based Pipeline Leak Detection System Using Fiber Bragg Grating-Based Pressure Sensors," *J. Lightw. Technol.,* vol. 35, no. 16, pp. 3366-3373, 2017.

[28] C. Ambrosino, P. Capoluongo, S. Campopiano, A. Cutolo, M. Giordano, D. Davino, C. Visone and A. Cusano, "Fiber bragg grating and magnetic shape memory alloy: Novel high-sensitivity magnetic Sensor," *IEEE Sens. J.,* vol. 7, no. 2, pp. 228 - 229, 2007.

[29] C. E. Campanella, F. D. Leonardis, L. Mastronardi, P. Malara, G. Gagliardi and V. M. N. Passaro, "Investigation of refractive index sensing based on Fano resonance in fiber Bragg grating ring resonators.," *Opt.*

Express, vol. 23, no. 11, pp. 14301-14313, 2015.

[30] A. Minardo, A. Cusano, R. Bernini, L. Zeni and M. Giordano, "Response of fiber Bragg gratings to longitudinal ultrasonic waves," *IEEE Trans. Ultrason., Ferroelectr. Freq. Control,* vol. 52, no. 2, p. 304–312, 2005.

[31] S. K. T. Grattan, P. A. M. Basheer, S. E. Taylor, W. Zhao, T. Sun and K. T. V. Grattan, "Fibre Bragg Grating sensors for reinforcement corrosion monitoring in civil engineering structures," *J. Phys. Conf. Ser.,* vol. 76, no. 1, p. 012018, 2007.

[32] W. Zhou, X. Dong, C. Shen, C. Zhao, C. C. Chan and P. Shum, "Temperature□independent vibration sensor with a fiber Bragg grating," *Microw. Opt. Technol. Lett.,,* vol. 52, no. 10, pp. 2282-2285, 2010.

[33] P. B. Varghese, K. N. Madhusoodanan, P. Vinod and P. Radhakrishnan, "A novel Fiber Bragg Grating sensor for measuring weight," in *2011 Annual IEEE India Conference*, 2011.

[34] W. Ecke and K. Schroeder, "Fiber Bragg grating optochemical sensor basing on evanescent-field interaction with surface plasmon waves," in *Proc. SPIE 7293, Smart Sensor Phenomena, Technology, Networks, and Systems 2009*, 2009.

[35] Ł. Dziuda, M. Krej and F. Skibniewski, "Fiber Bragg Grating Strain Sensor Incorporated to Monitor Patient Vital Signs During MRI," *IEEE Sens. J.,* vol. 13, no. 12, p. 4986–4991, 2013.

[36] J. Witt, F. Narbonneau, M. Schukar, K. Krebber, J. D. Jonckeere, M. Jeanne, D. Kinet, B. Paquet, A. Depre, L. T. D'Angelo, T. Thiel and R. Logier, "Medical Textiles With Embedded Fiber Optic Sensors for Monitoring of Respiratory Movement," *IEEE Sens. J.,* vol. 12, no. 1, p. 246–254, 2012.

[37] J. Albert, L. Shao and C. Caucheteur, "Tilted fiber Bragg grating sensors," *Laser Photon. Rev.,* vol. 7, p. 83–108, 2013.

[38] Q. Zhang, N. Liu, T. Fink, H. Li, W. Peng and M. Han, "Fiber-Optic Pressure Sensor Based on π-Phase-Shifted Fiber Bragg Grating on Side-Hole Fiber," *IEEE Photon. Technol. Lett.,* vol. 24, no. 17, pp. 1519 - 1522, 2012.

[39] H. Y. Chang, Y. C. Chang, H. J. Sheng, M. Y. Fu, W. F. Liu and R. Kashyap, "An Ultra-Sensitive Liquid-Level Indicator Based on an Etched Chirped-Fiber Bragg Grating," *IEEE Photon. Technol. Lett.,* vol. 28, no. 3, pp. 268 - 271, 2016.

[40] T. Osuch, K. Markowski and K. Jedrzejewski, "Temperature Independent Tapered Fiber Bragg Grating-Based Inclinometer," *IEEE Photon. Technol. Lett.,* vol. 27, no. 21, pp. 2312 - 2315, 2015.

[41] K. Khalid, M. Zafrullah, S. Bilal and M. Mirza, "Simulation and analysis of Gaussian apodized fiber Bragg grating strain sensor," *J. Opt. Technol.,* vol. 79, p. 667–673, 2012.

[42] H. Tsuda, K. Kumakura and S. Ogihara, "Ultrasonic sensitivity of strain-insensitive fiber Bragg grating sensors and evaluation of ultrasound-

induced strain," *Sensors,* vol. 10, pp. 11248-11258, 2010.

[43] M. Hamstad, "A review: Acoustic emission, a tool for composite-materials studies," *Exp. Mech.,* vol. 26, p. 7–13, 1986.

[44] C. Scruby, "An introduction to acoustic emission," *J. Phys. E Sci. Instrum,* vol. 20, no. 8, p. 946–953, 1987.

[45] Q. Wu, Y. Okabe and F. Yu, "Ultrasonic Structural Health Monitoring Using Fiber Bragg Grating," *Sensors,* vol. 18, p. 3395, 2018.

[46] J. Lim, H. Jang, K. Lee, J. Kim and B. Lee, "Interferometric fiber optic sensors," *Sensors,* vol. 12, p. 2467–2486, 2012.

[47] R. F. Cahill and E. Udd, "Solid-State Phase-Nulling Optical Gyro," *Appl. Opt.,* vol. 19, no. 18, pp. 3054-3056 , 1979.

[48] E. Udd, "Fiber-Optic Sensor Systems for Aerospace Applications," in *Proc. Spie*, 1987.

[49] L. B. Yuan, Q. B. Li, Y. J. Liang, J. Yang and Z. H. Liu, "Fiber optic 2-D sensor for measuring the strain inside the concrete specimen," *Sens. Actuatuator A,* vol. 94, no. 1, p. 25–31, 2001.

[50] R. D. Sante and L. Scalise, "A novel fiber optic sensor for multiple and simultaneous measurement of vibration velocity," *Rev. Sci. Instrum.,* vol. 75, no. 6, p. 1952–1958, June 2004.

[51] Y. Kim, U. Paek and B. H. Lee, "Measurement of refractive-index variation with temperature by use of long-period fiber gratings," *Opt. Lett.,* vol. 27, no. 15, p. 1297–1299, August 2002.

[52] L. B. Yuan, L. M. Zhou and J. S. Wu, "Fiber optic temperature sensor with duplex Michelson interferometric technique," *Sens. Actuatuator A,* vol. 86, p. 2–7, 2000.

[53] H. Y. Fu, H. Y. Tam, L. Y. Shao, X. Dong, P. K. A. Wai, C. Lu and S. K. Khijwania, "Pressure sensor realized with polarization-maintaining photonic crystal fiber-based Sagnac interferometer," *Appl. Opt.,* vol. 47, no. 15, pp. 2835-2839, 2008.

[54] Y. Rao, "Recent progress in fiber optic extrinsic Fabry-Perot interferometric sensors," *Opt. Fiber Technol.,* vol. 12, p. 227–237, 2006.

[55] T. Yoshino, K. Kurosawa, K. Itoh and T. Ose, "Fiber-optic Fabry-Perot interferometer and its sensor applications," *IEEE Trans. Microw. Theory Techn.,* vol. 30, no. 10, p. 1612–1621, Oct. 1982.

[56] É. Pinet, "Fabry–Perot fiber-optics sensors for physical parameters measurements in challenging conditions," *J. Sensor,* vol. 2009, pp. 1-9, 2009.

[57] D. H. Kim, J. W. Park, H. K. Kang, C. S. Hong and C. G. Kim, "Measuring dynamic strain of structures using a gold deposited extrinsic Fabry-Perot interferometer," *Smart Mater. Struct.,* vol. 12, no. 1, p. 1–5, December 2002.

[58] G. Zhou, L. M. Sim and J. Loughlan, "Damage evaluation of smart composite beams using embedded extrinsic Fabry-Perot interferometric strain sensors: bending stiffness assessment," *Smart Mater. Struct.,* vol. 13, no. 6, p. 1291–1302, 2004.

[59] M. Quirion and G. Ballivy, "Concrete strain monitoring with Fabry-Perot fber-optic sensor," *J. Mater. Civ. Eng.,* vol. 12, no. 3, p. 724–732, 2000.

[60] T. Liu, M. Wu, Y. Rao, D. A. Jackson and G. F. Fernando, "A multiplexed optical fbre-based extrinsic Fabry-Perot sensor system for in-situ strain monitoring in composites," *Smart Mater. Struct. ,* vol. 7, no. 4, p. 550–556, 1998.

[61] G. M. Gehring, R. W. Boyd, A. L. Gaeta, D. J. Gauthier and A. E. Willner, "Fiber-Based Slow-Light Technologies," *J. Lightw. Technol.,* vol. 26, no. 23, pp. 3752-3762, 2008.

[62] J. Gan, J. Chen, S. Xu, Z. Yang and Z. Jiang, "Slow/fast light using a very short Er3+/Yb3+ co-doped fiber," *Opt. Letters,* vol. 38, no. 5, p. 670–672, 2013.

[63] R. W. Boyd, "Material slow light and structural slow light: similarities and differences for nonlinear optics [Invited]," *J. Opt. Soc. Am. B,* vol. 28, no. 12, pp. A38-A44, 2011.

[64] A. Zadok, A. Eyal and M. Tur, "Stimulated Brillouin scattering slow light in optical fibers [Invited]," *Appl. Opt.,* vol. 50, no. 25, p. E38–E49, 2011.

[65] D. Dahan and G. Eisenstein, "Tunable all optical delay via slow and fast light propagation in a Raman assisted fiber optical parametric amplifier: a route to all optical buffering," *Opt. Express,* vol. 13, no. 16, p. 6234–6249, 2005.

[66] S. Melle, O. Calderon and M. Moreno, "Group velocity coupling and synchronization-like phenomenon of two light beams based on coherent population oscillations," *J. Phys. B: At. Mol. Opt. Phys.,* vol. 43, p. 1–10, 2010.

[67] N. Wheeler, P. Light, F. Couny and F. Benabid, "Slow and Superluminal Light Pulses Via EIT in a 20-m Acetylene-Filled Photonic Microcell," *J. Lightw. Tech.,* vol. 28, no. 6, p. 870–875, 2010.

[68] K. Y. Song, M. Herráez and L. Thévenaz, "Observation of pulse delaying and advancement in optical fibers using stimulated Brillouin scattering," *Opt. Exp.,* vol. 13, p. 82–88, 2005.

[69] Y. Okawachi, M. S. Bigelow, J. E. Sharping, Z. Zhu, A. Schweinsberg, D. J. Gauthier, R. W. Boyd and A. L. Gaeta, "Tunable all-optical delays via Brillouin slow light in an optical fiber," *Phys. Rev. Lett.,* vol. 94, no. 15, p. 153902, 2005.

[70] J. Sharping, Y. Okawachi and A. Gaeta, "Wide bandwidth slow light using a Raman fiber amplifier," *Opt. Exp.,* vol. 13, p. 6092–6098, 2005.

[71] E. Kuramochi, N. Matsuda, K. Nozaki, A. Park, H. Takesue and M. Notomi, "Wideband slow short-pulse propagation in one-thousand slantingly coupled L3 photonic crystal nanocavities," *Opt. Express,* vol. 26, no. 8, p. 9552–9564, 2018.

[72] J. Yu, S. Yuan, J. Gao and L. Sun, "Optical pulse propagation in a Fabry-Perot etalon: analytical discussion," *J. Opt. Soc. Am. A,* vol. 18, no. 9, p. 2153–2160, 2001.

[73] J. E. Heebner, V. Wong, A. Schweinsberg, R. W. Boyd and D. J. Jackson, "Optical Transmission Characteristics of Fiber Ring Resonators," *IEEE J. Quant. Electron.,* vol. 40, no. 6, p. 726–730, 2004.

[74] D. Janner, G. Galzerano, G. D. Vall, P. Laporta and S. Longhi, "Slow light in periodic superstructure Bragg gratings," *Phys. Rev. E,* vol. 72, pp. 1-8, 2005.

[75] H. Wen, G. Skolianos, S. Fan and M. Digonnet, "Slow Light in Fiber Bragg Gratings," *Proc. of SPIE,* vol. 7949, pp. 1-11, 2011.

[76] W. An, H. Jiang, Y. Fang, E. Wang, C. Chen and K. Xie, "Slow light generation using SBS in a liquid-core photonic crystal fiber," *J. Mod. Opt.,* vol. 64, no. 6, p. 632–638, 2016.

[77] L. Wang, B. Zhou, C. Shu and S. He, "Stimulated Brillouin scattering slow-light-based fiber-optic temperature sensor," *Opt. Lett.,* vol. 36, no. 3, pp. 427-430, 2011.

[78] Y. Zhang, H. Tian, X. Zhang, N. Wang, J. Zhang, H. Wu and P. Yuan, "Experimental evidence of enhanced rotation sensing in a slow-light structure," *Opt. Lett.,* vol. 35, no. 5, pp. 691-693, 2010.

[79] Y. Zhang, Y. Zhao and Q. Wang, "Improved design of slow light interferometer and its application in FBG displacement sensor," *Sens. Actuator A,* vol. 214, p. 168–174, 2014.

[80] Q. Wang, X. Feng, Y. Zhao, J. Li and H. Hu, "Research on fiber loop coupled resonator slow light and displacement sensing technology," *Sens.*

Actuator A, vol. 223, pp. 472-479, 2015.

[81] H. Gu, Y. Cui and J. Luan, "Angular Velocity Sensing Based on Double-Ring Slow-Light Structure," *IEEE Photon Technol. Lett.,* vol. 27, no. 24, pp. 2539-2542, 2015.

[82] W. S. Pang, Y. G. Shee, F. A. Rahman, F. R. M. Adikan and M. A. Mahdi, "Enhanced sensitivity temperature sensing based on second order Brillouin slow light," *Opt-Int. J. Light Electron Opt.,* vol. 228, p. 166146, 2021.

[83] H. Wen, M. Terrel, S. Fan and M. Digonnet, "Sensing With Slow Light in Fiber Bragg Gratings," *IEEE Sens. J.,* vol. 12, no. 1, pp. 156-163, 2012.

[84] W. Morey, J. Dunphy and G. Meltz, "Multiplexing fiber bragg grating sensors," in *Proc. SPIE 1586*, Boston, MA, United States, 1992.

[85] A. D. Kersey, M. A. Davis, H. J. Patrick, M. LeBlanc, K. P. Koo, C. G. Askins, M. A. Putnam and E. J. Friebele, "Fiber Grating Sensors," *J. Lightw. Technol.,* vol. 15, no. 8, pp. 1442-1463, 1997.

[86] T. H. T. Chan, L. Yu, H. Y. Tam, Y. Q. Ni, S. Y. Liu, W. H. Chung and L. K. Cheng, "Fiber Bragg grating sensors for structural health monitoring of Tsing Ma bridge: Background and experimental observation," *Eng. Struct.,* vol. 28, no. 5, p. 648–659, 2006.

[87] H. Y. Fu, H. L. Liu, W. H. Chung and H. Y. Tam, "A Novel Fiber Bragg Grating Sensor Configuration for Long-Distance Quasi-Distributed Measurement," *IEEE Sens. J.,* vol. 8, no. 9, pp. 1598-1602, 2008.

[88] Z. Luo, H. Guo and H. Wen, "Interrogation system for a sensor array with 1310-nm band ultra-weak fiber Bragg gratings," *Opt. Eng.,* vol. 52, no. 10, pp. 107101-1-107101-6, 2013.

[89] W. Stewart, B. V. Hoe, G. V. Steenberge and S. Schultz, "Spectral profile tracking of multiplexed fiber Bragg grating sensors," *Opt. Commn.,* vol. 357, p. 113–119, 2015.

[90] Y. Ou, C. Zhou, L. Qian, D. Fan, C. Cheng, H. Guo and Z. Xiong, "Large WDM FBG Sensor Network Based on Frequency-Shifted Interferometry," *IEEE Photon. Technol. Lett.,* vol. 29, no. 6, pp. 535-538, 2017.

[91] N. A. Mohammed, T. A. Ali and M. H. Aly, "Evaluation and performance enhancement for accurate FBG temperature sensor measurement with different apodization profiles in single and quasi-distributed DWDM systems," *Opt. Laser Eng.,* vol. 55, p. 22–34, 2014.

[92] D. J. F. Cooper, T. Coroy and P. W. E. Smith, "Time-division multiplexing of large serial fiber-optic Bragg grating sensor arrays," *Appl. Optics,* vol. 40, no. 16, pp. 2643-2654, 2001.

[93] H. Guo, L. Qian, C. Zhou, Z. Zheng, Y. Yuan, R. Xu and D. Jiang, "Crosstalk and Ghost Gratings in a Large-Scale Weak Fiber Bragg Grating Array," *J. Lightw. Technol.,* vol. 35, no. 10, pp. 2032-2036, 2017.

[94] Y. Wang, J. Gong, B. Dong, D. Y. Wang, T. J. Shillig and A. Wang, "A large serial time-division multiplexed fber Bragg grating sensor network," *J. Lightw. Technol.,* vol. 30, no. 17, pp. 2751 - 2756, 2012.

[95] V. Voisin, C. Caucheteur, D. Kinet, P. Megret and M. Wuilpart, "Self-Referenced Photon Counting OTDR Technique for Quasi-Distributed Fiber Bragg Gratings Sensors," *IEEE Sens. J.,* vol. 12, no. 1, pp. 118 - 123, 2012.

[96] G. Xin, L. Zhengying, W. Fan, W. Yiming, W. Changjia, Z. Siyue and Y. Haihu, "Distributed sensing technology of high-spatial resolution based on dense ultra-short FBG array with large multiplexing capacity," *Opt. Express,* vol. 25, no. 23, pp. 28112-28122, 2017.

[97] F. Ye, L. Qian, Y. Liu and B. Qi, "Using Frequency-Shifted Interferometry for Multiplexing a Fiber Bragg Grating Array," *IEEE Photon. Technol. Lett.,* vol. 20, no. 17, pp. 1488 - 1490, 2008.

[98] M. Majumder, T. K. Gangopadhyay, A. K. Chakraborty, K. Dasgupta and D. Bhattacharya, "Fibre Bragg gratings in structural health monitoring—Present status and applications," *Sens. Actuator A,* vol. 147, p. 150–164, 2008.

[99] Y. M. Gebremichael, W. Li, B. T. Meggitt, W. J. O. Boyle, K. T. V. Grattan, B. McKinley, L. F. Boswell, K. A. Aarnes, S. E. Aasen, B. Tynes, Y. Fonjallaz and T. Triantafillou, "A Field Deployable, Multiplexed Bragg Grating Sensor System Used in an Extensive Highway Bridge Monitoring Evaluation Tests," *IEEE Sens. J.,* vol. 5, no. 3, pp. 510-519, 2005.

[100] A. Kerrouche, J. Leighton, W. J. O. Boyle, Y. M. Gebremichael, T. Sun, K. T. V. Grattan and B. Täljsten, "Strain Measurement on a Rail Bridge Loaded to Failure Using a Fiber Bragg Grating-Based Distributed Sensor System," *IEEE Sens. J.,* vol. 8, no. 12, pp. 2059-2065, 2008.

[101] A. Kerrouche, W. Boyle, Y. Gebremichael, T. Sun, K. Grattan, B. Täljsten and A. Bennitz, "Field tests of fibre Bragg grating sensors incorporated into CFRP for railway bridge strengthening condition monitoring," *Sens. Actuators A,* vol. 148, p. 68–74, 2008.

[102] C. Rodrigues, C. Felix, A. Lage and J. Figueiras, "Development of a long-term monitoring system based on FBG sensors applied to concrete bridges," *Eng. Struct.,* vol. 32, p. 1993–2002, 2010.

[103] G. Kister, D. Winter, J. Leighton, R. A. Badcock, P. D. Tester, S. Krishnamurthy, W. J. O. Boyle, K. T. V. Grattan and G. F. Fernando, "Methodology and integrity monitoring of foundation concrete piles using Bragg grating optical fibre sensors," *Eng. Struct.,* vol. 29, no. 9, p. 2048–2055, 2007.

[104] K. Schroeder, W. Ecke, J. Apitz, E. Lembke and G. Lenschow, "A fibre Bragg grating sensor system monitors operational load in a wind turbine rotor blade," *Meas. Sci. Technol.,* vol. 17, p. 1167–1172, 2006.

[105] H. J. Bang, H. I. Kim and K. S. Lee, "Measurement of Strain and Bending Deflection of a Wind Turbine Tower Using Arrayed FBG Sensors," *Int. J. Precis. Eng. Manuf.,* vol. 13, no. 12, pp. 2121-2126, 2012.

[106] K.-S. Cho, Y.-H. Huh, I.-B. Kwon and D.-J. Yoon, "A tip deflection calculation method for a wind turbine blade using temperature compensated FBG sensors," *Smart Mater. Struct. ,* vol. 21, p. 025008, 2012.

[107] D. Kang and W. Chung, "Integrated monitoring scheme for a maglev

guideway using multiplexed FBG sensor arrays," *Non Destructive Testing and Evaluation International (NDT&E Int.),* vol. 42, p. 260–266, 2009.

[108] J. Gomez, I. Jorge, G. Durana, J. Arrue, J. Zubia, G. Aranguren, A. Montero and I. López, "Proof of Concept of Impact Detection in Composites Using Fiber Bragg Grating Arrays," *Sensors,* vol. 13, pp. 11998-12011, 2013.

[109] M. Vidakovic, C. McCague, I. Armakolas, T. Sun, J. S. Carlton and K. T. V. Grattan, "Fibre Bragg Grating-Based Cascaded Acoustic Sensors for Potential Marine Structural Condition Monitoring," *J. Lightw. Technol.,* vol. 34, no. 19, pp. 4473-4478, 2016.

[110] Y. Zhao, Y. Zhu, M. Yuan, J. Wang and S. Zhu, "A Laser-Based Fiber Bragg Grating Ultrasonic Sensing System for Structural Health Monitoring," *IEEE Photon. Technol. Lett.,* vol. 28, no. 22, pp. 2573-2576, 2015.

[111] W. Li, T. Liu and H. Xiang, "Leakage detection of water pipelines based on active thermometry and FBG based quasi-distributed fiber optic temperature sensing," *J. Intell. Mater. Syst. Struct.,* pp. 1-12, 2021.

[112] X. Bao and L. Chen, "Recent Progress in Distributed Fiber Optic Sensors," *Sensors,* vol. 12, pp. 8601-8639, 2012.

[113] X. Zeng, X. Bao, C. Y. Chhoa, T. W. Bremner, A. W. Brown, M. D. DeMerchant, G. Ferrier, A. L. Kalamkarov and A. V. Georgiades, "Strain measurement in a concrete beam by use of the Brillouin-scattering-based distributed fiber sensor with single-mode fibers embedded in glass fiber

reinforced polymer rods and bonded to steel reinforcing bars," *Appl. Opt.,* vol. 41, no. 24, p. 5105–5114, 2002.

[114] Z. L. Wang, J. Chang, S. S. Zhang, G. P. Lv, W. J. Wang, S. Jiang, X. Z. Liu, X. H. Liu, S. Luo, B. N. Sun and Y. N. Liu, "Spatial Resolution Improvement of Distributed Raman Temperature Measurement System," *IEEE Sens. J.,* vol. 13, no. 11, pp. 4271-4278, 2013.

[115] S. Yadav, A. Kumar, T. S. Saini and R. K. Sinha, "SBS based slow-light generation in rectangular lattice graded-index photonic crystal fiber: Design and analysis," *Opt-Int. J. Light Electron Opt.,* vol. 132, p. 164–170, 2017.

[116] L. Wang and C. Shu, "Demonstration of Distributed Strain Sensing With the Use of Stimulated Brillouin Scattering-Based Slow Light," *IEEE Photon. Technol. Lett.,* vol. 3, no. 6, pp. 1164-1170, 2011.

[117] L. Wang, B. Zhou, C. Shu and S. He, "Distributed Temperature Sensing Using Stimulated-Brillouin-Scattering-Based Slow Light," *IEEE Phton. Technol. Lett.,* vol. 5, no. 6, p. 6801808, 2013.

[118] P. Ferdinand, "The evolution of optical fiber sensors technologies during the 35 last years and their applications in structure health monitoring," in *EWSHM - 7th European Workshop on Structural Health Monitoring, IFFSTTAR, Inria, Université de Nantes, Jul 2014*, Nantes, France, 2014.

[119] W. Zhang, W. Chen, X. Lei and C. Wang, "Accuracy evaluation of demodulation results of fiber Bragg grating sensors," *Appl. opt.,* vol. 56,

no. 33, pp. 9212-9220, 2017.

[120] K. O. Hill and G. Meltz, "Fiber Bragg Grating Technology," *J. Lightw. Technol.,* vol. 15, no. 7, pp. 1263-1276, 1997.

[121] K. O. Hill, Y. Fujii, D. C. Johnson and B. S. Kawasaki, "Photosensitivity in optical fiber waveguides: Application to reflection filter," *Appl. Phys. Lett.,* vol. 32, p. 647–649, 1978.

[122] T. Osuch and Z. Jaroszewicz, "Numerical analysis of apodized fiber Bragg gratings formation using phase mask with variable diffraction efficiency," *Opt. Comm.,* vol. 284, p. 567–572, 2011.

[123] T. Erdogan, "Fiber Grating Spectra," *J. Lightw. Technol.,* vol. 15, no. 8, pp. 1277-1294, 1997.

[124] N. A. Mohammed, T. A. Ali and M. H. Aly, "Performance optimization of apodized FBG-based temperature sensors in single and quasi-distributed DWDM systems with new and different apodization profiles," *AIP Adv.,* vol. 3, p. 122125, 2013.

[125] T. Ali, M. Shehata and N. A. Mohammed, "Design and performance investigation of a highly accurate apodized fiber Bragg grating-based strain sensor in single and quasi-distributed systems," *Appl. Opt.,* vol. 54, pp. 5243-5251, 2015.

[126] N. A. Mohmammed and H. O. Elserafy, "Ultra-sensitive quasi-distributed temperature sensor based on an apodized fiber Bragg grating," *Appl. Opt.,* vol. 57, no. 2, pp. 273-282, 2018.

[127] S. A. Kolpakov, Y. O. Barmenkov and V. Aboites, "Asymmetrically Apodized Fiber Bragg Gratings for Applications in Dispersion Less Fabry-Prot Fiber Cavities," *Fiber Integr. Opt.,* vol. 29, pp. 466-479, 2010.

[128] J. Canning, D. C. Psaila, Z. Brodzeli, A. Higley and M. Janos, "Characterization of apodized fiber Bragg gratings for rejection filter applications," *Appl. Opt.,* vol. 36, no. 36, p. 9378–9382, 1997.

[129] K. Ennser, M. N. Zervas and R. I. Lamming, "Optimization of Apodized Lineraly Chirped Fiber Gratings for Optical Communications," *IEEE J. Quantum Electrs.,* vol. 34, pp. 770-778, 1998.

[130] Y. Zhao, C. Qin and Q. Wang, "Principles of Structural Slow Light and Its Appilications for Optical Fiber Sensors: A Review," *Instr. Science and Technol.,* vol. 42, p. 72–94, 2014.

[131] G. Skolianos, A. Arora, M. Bernier and M. Digonnet, "Slow light in fber Bragg gratings and its applications," *J. Phys. D,* vol. 49, p. 463001 , 2016.

[132] A. D. Kersey, T. A. Berkoff and W. W. Morey, "High resolution fibre grating based strain sensor with interferometric wavelength-shift detection," *Electron. Lett.,* vol. 28, no. 3, p. 136–138, 1992.

[133] B. Lissak, A. Arie and M. Tur, "Highly sensitive dynamic strain measurement by locking lasers to fiber Bragg gratings," *Opt. Lett.,* vol. 23, no. 24, p. 1930–1932, 1998.

[134] H. Wen, G. Skolianos, S. Fan, M. Bernier, R. Valle and J. F. D. M,

"Slow-Light Fiber-Bragg-Grating Strain Sensor with a 280-femtostrain/√Hz Resolution," *J. Lightw. Tech.,* vol. 31, no. 11, p. 1804–1808, 2013.

[135] G. Skolianos, A. Arora, M. Bernier and M. Digonnet, "Measuring attostrains in a slow-light fiber Bragg grating," in *Proc. of SPIE*, 2016.

[136] Q. Wang, M. Guo and Y. Zhao, "A Sensitivity Enhanced Microdisplacement Sensing Method Improved Using Slow Light in Fiber Bragg," *IEEE Trans. Inst. Meas.,* vol. 66, no. 1, p. 122–130, 2017.

[137] A. Arora, M. Esmaeelpour, M. Bernier and M. J. F. Digonnet, "High-resolution slow-light fiber Bragg grating temperature sensor with phase-sensitive detection," *Opt. Letters ,* vol. 23, p. 3337–3340, 2018.

[138] P. B. Vigneron, T. Boilard, E. Balliu, A. L. Broome, M. Bernier and M. J. F. Digonnet, "Loss-compensated slow-light fiber Bragg grating with 22-km/s group velocity," *Opt. Lett.,* vol. 45, no. 11, pp. 3179-3182, 2020.

[139] D. Gatti, G. Galzerano, D. Janner, S. Longhi and P. Laporta, "Fiber strain sensor based on a π-phase shifted Bragg grating and the Pound-Drever-Hall technique," *Opt. Exp.,* vol. 16, no. 3, p. 1945–1950 , 2008.

[140] D. Srivastava, U. Tiwari and B. Das, "Interferometric interrogation of π-phase shifted fiber Bragg grating sensors," *Optics Commun.,* vol. 410, p. 88–93, 2018.

[141] N. B. Ali, J. Zaghdoudi, M. Kanzari and R. Kuszelewicz, "The slowing of light in one-dimensional hybrid periodic and non-periodic photonic

crystals," *J. Opt. ,* vol. 12, pp. 1-9, 2010.

[142] G. Skolianos, M. Bernier, R. Valle and M. Digonnet, "Observation of~20 ns group delay in a low-loss apodized fiber Bragg grating," *Opt. Lett.,* vol. 31, no. 11, p. 3978–3981, 2014.

[143] Q. Wu, Y. Okabe and F. Yu, "Ultasonic Structural Health Monitorig Using Fiber Bragg Grating," *Sensors,* vol. 18, p. 3395, 2018.

[144] N. Takeda, Y. Okabe, J. Kuwahara and S. Kojima, "Lamb wave sensing using fiber Bragg grating sensors for delamination detection in composite laminates," in *Proc. SPIE*, 2005.

[145] S. Liang, S. C. Tjin, B. Lin, X. Sheng, S. Lou, Y. Zhang and X. Wang, "Novel Fiber Bragg Grating Sensing Method Based on the Sidelobe Modulation for Ultrasound Detection," *J. Lightw. Technol.,* vol. 37, no. 11, p. 2686–2693, 2019.

[146] A. Rosenthal, D. Razansky and V. Ntziachristos, "High-sensitivity compact ultrasonic detector based on a pi-phase-shifted fiber Bragg grating," *Opt. Lett.,* vol. 36, no. 10, p. 1833–1835, 2011.

[147] J. Guo and C. Yang, "Highly stabilized phase-shifted fiber Bragg grating sensing system for ultrasonic detection," *IEEE Photon. Technol. Lett.,* vol. 27, no. 8, p. 848–85, 2015.

[148] Q. Wu and Y. Okabe, "High-sensitivity ultrasonic phase-shifted fiber Bragg grating balanced sensing system," *Opt. Exp.,* vol. 20, no. 27, p. 28353–28362, 2012.

[149] L. Hu and M. Han, "Reduction of Laser Frequency Noise and Intensity Noise in Phase-Shifted Fiber Bragg Grating Acoustic-Emission Sensor System," *IEEE Sens. J.,* vol. 17, no. 15, p. 4820–4825, 2017.

[150] Q. Wu and Y. Okabe, "Ultrasonic sensor employing two cascaded phase-shifted fiber Bragg gratings suitable for multiplexing," *Opt. Lett.,* vol. 37, no. 16, p. 3336–3338, 2012.

[151] R. S. Weis, A. D. Kersey and T. A. Berkoff, "A Four-Element Fiber Grating Sensor Array with Phase Sensitive Detection," *IEEE Photon. Technol. Lett.,* vol. 6, no. 12, p. 1469–1472, 1994.

[152] K. P. Koo and A. D. Kersey, "Bragg Grating-Based Laser Sensors Systems with Interferometric Interrogation and Wavelength Division Multiplexing," *J. Lightw. Technol.,* vol. 13, no. 7, p. 1243–1249, 1995.

[153] V. Chandra, U. Tiwari and B. Das, "Elimination of Light Intensity Noise Using Dual-Channel Scheme for Fiber MZI-Based FBG Sensor Interrogation," *IEEE Sens. J.,* vol. 16, no. 8, p. 2431–2436, 2016.

List of publications

Journals

(**By mistake, name of one of my supervisor, Prof Sunil K Khijwania, is missed out in these publications*)

1. *Krishna Mohan Dwivedi, Tomasz Osuch, and Gaurav Trivedi, "High Sensitive and Large Dynamic Range Quasi-Distributed Sensing System Based on Slow-Light π-phase-shifted Fiber Bragg Grating," Opto-Electronics Review, vol. 27, no.3, pp. 233–240, Sept. 2019.

2. Krishna Mohan Dwivedi, Gaurav Trivedi, Sunil K Khijwania, and Tomasz Osuch, "Design and Numerical Analysis of a High Sensitive Ultrasonic Acoustic sensor based on π-phase-shifted Fiber Bragg Grating and Fiber Mach-Zehnder Interferometer Interrogation," Metrology and Measurement Systems, vol. 27, no. 2, pp. 289–300, June 2020.

3. Krishna Mohan Dwivedi, Gaurav Trivedi and Sunil K Khijwania, "Fiber Bragg Grating Employing Novel Apodization Profile: Performance Optimization for Quasi-Distributed Sensing Applications" Optical and Quantum Electronics, vol. 54, pp. 1-17, May 2022.

Conferences

1. Krishna Mohan Dwivedi, Gaurav Trivedi and Sunil K Khijwania, "Theoretical Study and Optimization of Apodized Fiber Bragg Grating Sensors for Single and Quasi-distributed Structural Health Monitoring Applications," Radioelectronika 2020.

2. Krishna Mohan Dwivedi, Sunil K Khijwania, Gaurav Trivedi, and Tomasz Osuch, "Theoretical Analysis of pi-Phase-Shifted Fiber Bragg Grating for Longitudinal Ultrasonic Acoustic Wave," IEEE WRAP 2019.

3. *Krishna Mohan Dwivedi, Gaurav Trivedi, Tomasz Osuch, Karel Juryca, and Jan Pidanič, "Theoretical Analysis of Slow-light in π-phase-shifted fiber Bragg grating and its sensing applications," In IEEE 2019 Conference on Microwave Techniques (COMITE), pp. 1–6, 2019.

4. Krishna Mohan Dwivedi, Gaurav Trivedi, and Sunil K Khijwania, "A Sensitive Enhanced Acousto-ultrasonic Sensor using π-Fiber Bragg Grating

and Interferometric interrogation," in Proc. of Photonics, Photonics 2018, pp.1–2, 2018.

5. Krishna Mohan Dwivedi, Gaurav Trivedi, and Sunil K Khijwania, "Study of Slow-Light in π-phase shifted Fiber Bragg Grating," in Proc. of Photonics, Photonics 2018, pp. 1–2, 2018.

6. Krishna Mohan Dwivedi, Gaurav Trivedi, and Sunil K Khijwania, "Theoretical Analysis of Fiber Bragg Grating Employing Novel Apodization Profile," in Proc. of Photonics, Photonics 2018, pp. 1–2, 2018.

7. Krishna Mohan Dwivedi, Gaurav Trivedi, and Sunil K Khijwania, "Novel Apodization Profile for Performance Optimization of Uniform and Linearly Chirped Fiber Bragg Gratings," ICAOP-2017, pp. 1–6, 2017.

8. Krishna Mohan Dwivedi, Gaurav Trivedi, and Sunik K Khijwania, "Design and Analysis of Fiber Bragg Grating Employing Novel Apodization Profile," IEEE WRAP-2017, pp. 1–3, 2017.